NUMERICAL METHODS AND COMPARISON FOR SIMULATING LONG STREAMER PROPAGATION

HUANG MENGMIN

(B.Sc., Beijing Normal University, China)

A THESIS SUBMITTED

FOR THE DEGREE OF DOCTOR OF PHILOSOPHY

DEPARTMENT OF MATHEMATICS

NATIONAL UNIVERSITY OF SINGAPORE

2014

To my family

DECLARATION

I hereby declare that the thesis is my original work and it has been written by me in its entirety.

I have duly acknowledged all the sources of information which have been used in the thesis.

This thesis has also not been submitted for any degree in any university previously.

Huang Mengmin

Oct 2014

Acknowledgements

Firstly, I would like to express my deepest gratitude to my supervisor, Prof. Bao Weizhu, and co-supervisor, Dr. Liu Jie. Prof. Bao is a very strict supervisor. He teaches me how to become a professional person. He also tells me how to do research well during my PhD period. Dr. Liu is an efficient and smart person. He can always proposed some good ideas to solve different problems and made my research go well. Specially, Dr. Liu have helped me quite a lot with programming. He usually spends much of his time to figure out the incorrectness in my codes. Without his guidance, this thesis can not be completed. Their rigorous academic attitude has a powerful influence on my future life.

My research work is collaborated with Prof. Zeng Rong and Dr. Zhuang Chijie from Tsinghua University, China. Prof. Zeng supported me very well when I visit Tsinghua University in July 2011. I cannot make progress without the discussion with Dr. Zhuang. Dr. Zhuang also helped me improve my codes and revise my first publication.

I also want to thank Prof. Zhang Hui from Beijing Normal University, China. It was him who gave me this opportunity to have further study in NUS.

I am grateful to Prof. Ren Weiqing, Prof. Shen Zuowei, Prof. Xu Xingwang, Dr. Yip Ming-ham, Prof. Yu Shih-Hsien, Prof. Zhang Louxin, Prof. Zhao Gongyun

and all the other teachers who have ever taught me in NUS. From their modules, I have a broader understanding of mathematics. Some knowledge in these modules gives me help to finish this thesis. I am also grateful to Department of Mathematics and National University of Singapore for generous financial support in the past five years.

Besides, my fellow friends, Dr. Cai Yongyong, Dr. Dong Xuanchun, Dr. Tang Qinglin, Mr. Wang Nan, Mr. Zhao Xiaofei, Mr. Jia Xiaowei, Ms. Wang Yan and Mr. Ruan Xinran have helped me a lot. Thanks for the companying and discussion.

Last but not least, my parents have given me their unconditional love. My girlfriend, Ms. Tang Ling has always been very supportive of everything about me. She taught me much about life and made me mature.

Huang Mengmin

Oct 2014

Abstract

In plasma physics, streamer propagation is an interesting discharge phenomenon which has many applications in engineering and industry. Due to the small time scale of streamer propagation, numerical simulation becomes a more effective way to study the streamer than experiment. The governing partial differential equations (PDEs) of streamer propagation include continuity equations for the particle densities coupled with a Poisson's equation for the electric potential.

In this thesis, two discontinuous Galerkin (DG) methods are proposed to solve the continuity equations since there are large derivatives or even jumps in the profile of particle densities. Meanwhile, the Poisson's equation is solved by 4 different methods which include finite difference method (FDM), mixed finite element method (MFEM), least-squares finite element method (LSFEM), and symmetric interior penalty Galerkin (SIPG) method. We have compared the compatibility when these 4 methods are coupled with DG methods for continuity equations. The comparison results recommend that FDM is the best method for Poisson's equations if uniform rectangular meshes are used and SIPG method is the best choice for triangular meshes. By applying the recommended methods, we have simulated many configurations of short and long streamer propagations and successfully captured the features of streamer.

In summary, this thesis work is a comprehensive study in applying DG methods to numerical simulations of streamer propagations. It supplements some early numerical studies done by our collaborators. The gap lengths in most of the simulations in our study are 5 times longer as the existing results, hence we have observed more interesting phenomenon during simulations, for example the bifurcation of streamer. We have considered not only the rectangular computational domain in this thesis, but also carried out simulation in complex geometry. Our study indicates that DG method are highly potential competitor in simulating streamer propagations. In addition, this work studies the numerical compatibility in the coupling between hyperbolic system and elliptic equation.

Key words: streamer propagations, hyperbolic system, coupling with elliptic equation, discontinuous Galerkin methods, mixed finite element method, least-squares finite element method.

Contents

List of Tables

List of Figures

Chapter 1

Introduction

1.1 Background

In physics, plasma is a state of matter in which a certain portion of the particles are ionized [56]. When non-ionized or lowly ionized matter is exposed to high electric field, non-equilibrium ionization processes, so-called discharges, occur. In recent years, plasma discharges have been studied in industrial and technical applications [17, 74, 91]. A particular example of plasma discharges is lightning, which is still a big problem and needs to be aboratively studied. Another interesting experimental example is the breakdown in air gap which is submitted to a very high, in magnitude, voltage at atmospheric pressure [47, 65].

Consider two metal electrodes, anode and cathode, which are separated by a gas-filled gap. Up to a certain threshold value of applied electric field, free electrons are produced by ionizations. When the free electron forms an electron avalanche, the so-called first corona inception occurs [34]. In a positive discharge where the gap is submitted to a positive voltage, the electron avalanche moving towards the anode creates a net positive charge which increases the electric field near the avalanche. If the modified electric field is high enough, new avalanches can be generated and developed. The discharge process then consists of a series of avalanches developing

into narrow branched plasma channels, which are called streamers. These channels develop from a common root. On the other hand, if a negative voltage is applied to the air gap, the first corona will disappear after some time; and then two coronas of opposite polarity, positive corona and negative corona, develop after the extinction of the first corona.

If the gap is long enough such that breakdown occurs after a large time scale, a new phenomenon called leader will be observed. In positive discharge, leader appears as a weakly luminous channel from the common root of positive streamer, and then elongates and propagates continuously, and also pushes the streamer. On the other hand, in negative discharge, since positive corona propagates towards the H.V. electrode and negative corona moves in the opposite way, a new leader channel occurs between them. This leader is called space leader and elongates bi-directionally. Therefore, a junction of space leader and original leader will produce a strong illumination of the whole channel.

The mechanism of streamer and leader has been studied in the past three decades [49, 51, 59, 68, 72, 79]. Firstly, the minimum inception field of the first corona is empirically given by the Peek's equation [75]

$$E = E_0 \delta M \left(1 + \frac{K}{\sqrt{\delta R}}\right),$$

where E_0 is the breakdown field in the range of $10^6 V/m$, δ is relative air density, R is equivalent curvature radius of electrode, K and M are two constants. This formula is just one of the various criteria [1, 45, 55, 66, 67] for the inception of streamer. This inception process can continue for several microseconds during the propagation of streamers as long as the electric field around the tip of streamers is sufficiently large. The streamer usually propagates with velocity in the range of $10^7 cm/s$; therefore, in the short gap (in the millimeter or centimeter range), breakdown occurs in several nanoseconds.

On the other hand, in the elongation of leader, since the electrons and positive ions travel in opposite direction in the leader channel, current is created. Then the

thermal energy in the leader channel will be increased by the current due to Joule effect. Thus, different from the mechanism of streamer, leader is governed by a thermal process. The diameter of leader channel is proportional to the length of the gap. It is between 0.5 and 1mm for a 1.5m gap and between 2 and 4mm for a 10m gap. The temperature in leader channel can reach several thousands of Kelvin. This elongation process can continue for several hundred microseconds.

For a better understanding of streamer and leader, one can refer to the schematic representation in Figure 1.1, which is cited from [33],

So far, the most common method for studying streamer discharges is still to do the experiments [16, 34, 39, 80, 81, 82, 83, 90]. However, the above small time scales of the discharge processes regretfully indicate that it is difficult to acquire experimental data. Therefore, more researchers start to develop proper physical and mathematical models and do accurate numerical simulations to study streamer propagation.

1.2 Mathematical models

Based on experimental studies, scientists have developed many different empirical models, for example the Critical Volume Model proposed by the Renardières Group [81] and its modifications [4, 27, 77], some models for describing the branching phenomenon of streamer [2, 69] and static models for space charges [23, 42, 94]. These empirical models are based on some empirical formulas; as a result, they usually amplify some features during the streamer propagation process but neglect some other features. For example in [2], the authors took too much care about the randomness of streamer propagation; hence their streamer channels spread out around the tip electrode and seldom propagated to the other electrode. Thus, some kinetic models are developed to overcome this problem. For instant, the kinetic model with Monte Carlo simulation [48] and particle-in-cell (PIC) model [78, 87] use the so-called superparticle (clouds of particles) instead of as single particle.

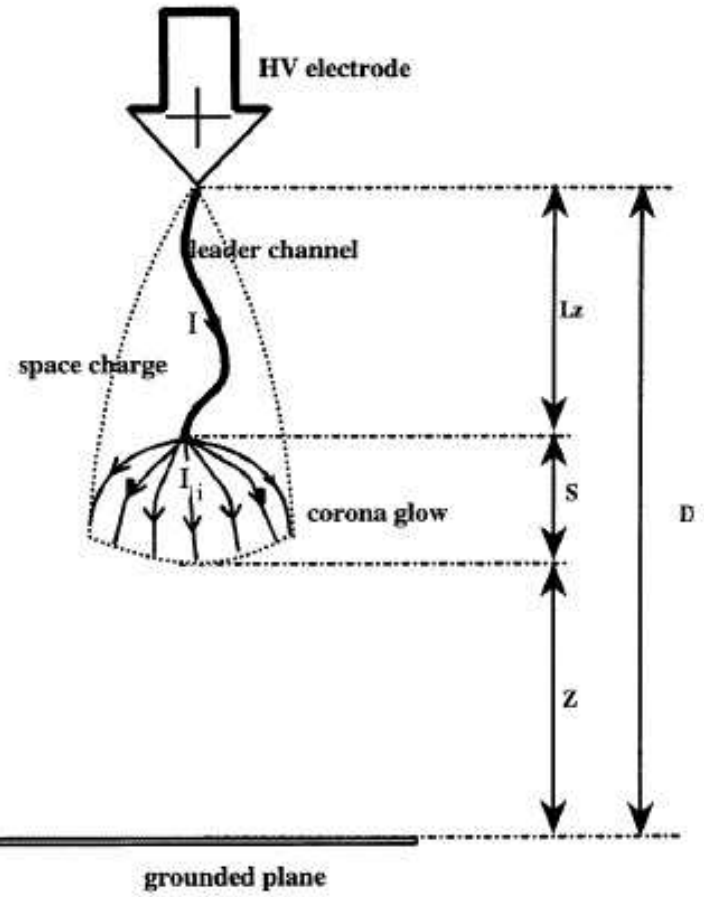

Figure 2. A schematic representation of the leader–streamer system.

Figure 1.1: This figure shows the well-developed streamer and leader. The "corona glow" is also called streamer.

Although kinetic models can simulate the streamer propagation more exactly, it is still difficult to implement because of the large computational cost. Therefore, fluid models have been widely accepted and provided good descriptions of discharge processes [38, 76, 93, 97].

1.2.1 Three-dimensional model

The most common fluid model for streamer propagation is a three-dimensional (3D) model which contains three continuity equations for particle densities of electron N_e, positive ion N_p and negative ion N_n, and a Poisson's equation for electric potential V as follows,

$$\begin{cases} \frac{\partial N_e}{\partial t} + \nabla \cdot (N_e \mathbf{W}_e - \mathbb{D}\nabla N_e) = (\alpha(|\mathcal{E}|) - \eta(|\mathcal{E}|))N_e|\mathbf{W}_e| - \beta N_e N_p + S_{ph}(N_e, \mathcal{E}), \\ \frac{\partial N_p}{\partial t} + \nabla \cdot (N_p \mathbf{W}_p) = \alpha(|\mathcal{E}|)N_e|\mathbf{W}_e| - \beta N_e N_p - \beta N_n N_p + S_{ph}(N_e, \mathcal{E}), \\ \frac{\partial N_n}{\partial t} + \nabla \cdot (N_n \mathbf{W}_n) = \eta(|\mathcal{E}|)N_e|\mathbf{W}_e| - \beta N_n N_p, \\ -\nabla^2 V = \frac{e}{\epsilon}(N_p - N_e - N_n),\ \mathcal{E} = -\nabla V. \end{cases} \tag{1.1}$$

In (1.1), $\mathbf{W}_e$, $\mathbf{W}_p$ and $\mathbf{W}_n$ are the drift velocities for electron, positive ion and negative ion respectively, which equal to the electric field $\mathcal{E}$ multiplied by mobility μ_e, μ_p and μ_n, i.e. $\mathbf{W}_{e,p,n} = \mu_{e,p,n}\mathcal{E}$; $\mathbb{D}$ is the diffusion tensor; $\alpha(|\mathcal{E}|)$ is an impact ionization coefficient described with Townsend's approximation [80], i.e., $\alpha(|\mathcal{E}|) = APe^{BP/|\mathcal{E}|}$, where P is the air pressure in torr and A, B are two parameters. $\eta(|\mathcal{E}|)$ is the electron attachment coefficient and β is the recombination coefficient. $S_{ph}(N_e, \mathcal{E})$ is the photoionization source which can be calculated either by the integral method of Zheleznyak *et al.* [100] or by solving a set of Helmholtz equations [13, 57, 73]; this source term can be neglected in negative streamer [62] or can be equivalent to the background ionization under certain conditions [7, 96]. The constants e and ϵ are called elementary charge and permittivity of vacuum respectively. The physical domain in model (1.1) is the whole space between anode and cathode, therefore we impose the Dirichlet boundary conditions for Poisson's equation at the electrodes. We allow the flux of particles to pass through the boundaries [62], thus we impose homogeneous Neumann boundary conditions for continuity equations at the electrodes.

Various modifications of (1.1) exist in the literature. For example, C. Montijn

only considered electrons, positive ions and the impact ionization source, and ignored the drift term for positive ions [62]; O. Ducasse *et al.* dealt with (1.1) but with constant photoionization source $S_{ph} \equiv 10^{26} m^{-3} \cdot s^{-1}$ [29]; N. L. Aleksandrov further introduced active particles and the reaction between active particles and other charged particles [3]. The reason for them to keep different terms in the fluid model can be seen from the following dimensionless analysis. For simplicity, we only consider the minimal fluid model studied by C. Montijn *et al.* in 2006 [62] in the rest part of this chapter.

Define the scaled variables

$$\tau = \frac{t}{t_0},\ \tilde{x} = \frac{x}{x_0},$$

and

$$\mathbf{E}(\tilde{x},\tau) = \frac{\mathcal{E}(x,t)}{E_0},\ \sigma(\tilde{x},\tau) = \frac{N_e(x,t)}{N_0},\ \rho(\tilde{x},\tau) = \frac{N_p(x,t)}{N_0},\ \phi(\tilde{x},\tau) = \frac{V(x,t)}{V_0}.$$

It is natural to set x_0 to be the length of gap (i.e. the shortest distance between anode and cathode) and set V_0 to be the absolute value of the applied voltage at either anode or cathode. Plugging the above new functions into (1.1), and using the chain rule, we can obtain

$$\begin{cases} \frac{\partial \sigma}{\partial \tau} + \nabla_{\tilde{x}} \cdot (\frac{t_0 \mu_e E_0}{x_0} \sigma \mathbf{E} - \frac{t_0 \mathbb{D}}{x_0^2} \nabla_{\tilde{x}} \sigma) = t_0 \alpha(E_0|\mathbf{E}|) E_0 |\mu_e \mathbf{E}| \sigma, \\ \frac{\partial \rho}{\partial \tau} + \nabla_{\tilde{x}} \cdot (\frac{t_0 \mu_p E_0}{x_0} \rho \mathbf{E}) = t_0 \alpha(E_0|\mathbf{E}|) E_0 |\mu_e \mathbf{E}| \sigma, \\ -\nabla_{\tilde{x}}^2 \phi = \frac{N_0 x_0^2}{V_0} \frac{e}{\epsilon} (\rho - \sigma), \\ \mathbf{E} = -\frac{V_0}{E_0 x_0} \nabla_{\tilde{x}} \phi. \end{cases} \tag{1.2}$$

We set

$$\frac{V_0}{E_0 x_0} = 1,\ \frac{N_0 x_0^2}{V_0} \frac{e}{\epsilon} = 1,\ \frac{t_0 \mu_e E_0}{x_0} = -1 := \mu_\sigma,$$

in (1.2), which means

$$E_0 = \frac{V_0}{x_0},\ t_0 = -\frac{x_0}{\mu_e E_0},\ N_0 = \frac{V_0 \epsilon}{x_0^2 e}, \tag{1.3}$$

and

$$\begin{aligned}
&\tilde{\mathbb{D}} = \frac{t_0 \mathbb{D}}{x_0^2}, \\
&\frac{t_0 \mu_p E_0}{x_0} = \frac{\mu_p}{\mu_e} := \mu_\rho, \\
&t_0 \alpha(E_0|\mathbf{E}|) E_0 |\mu_e \mathbf{E}| = x_0 A P e^{(BP/E_0)/|\mathbf{E}|} |\mathbf{E}| := S|\mathbf{E}| e^{K/|\mathbf{E}|}.
\end{aligned} \tag{1.4}$$

In this way, the dimensionless model becomes (we have changed the time variable back to t)

$$\begin{cases}
\frac{\partial \sigma}{\partial t} + \nabla \cdot (\mu_\sigma \sigma \mathbf{E} - \tilde{\mathbb{D}} \nabla \sigma) = S|\mathbf{E}| e^{K/|\mathbf{E}|} \sigma, \\
\frac{\partial \rho}{\partial t} + \nabla \cdot (\mu_\rho \rho \mathbf{E}) = S|\mathbf{E}| e^{K/|\mathbf{E}|} \sigma, \\
-\nabla^2 \phi = \rho - \sigma, \ \mathbf{E} = -\nabla \phi.
\end{cases} \tag{1.5}$$

In nitrogen under standard atmospheric pressure, by using the data given in [62], one can find that $\mu_\rho \sim 0.009$, which is the reason why the positive ions are considered to be immobile by some scientists [26, 62]. If the recombination coefficient β is taken into consideration, the rescaled coefficient $\beta N_0 t_0$ is equal to 2.9×10^{-4} [65]; therefore, the recombination coefficient could be ignored [104].

1.2.2 Quasi three-dimensional model

The model (1.5) is still a 3D model which is expensive for numerical computation. To save the memory and computation time as well, scientists have considered some simplifications in reducing the dimension. In this thesis, two ways are chosen to reduce the dimension.

The first and more common way is to assume that the particles are distributed with cylindrical symmetry and the physical domain is also symmetric. Therefore, it is easy to apply cylindrical coordinates (r, z, θ) to simplify the 3D model (1.5) to a quasi three-dimensional (quasi 3D) model, assuming that all the physical quantities

are independent of angular variable θ,

$$\begin{cases} \frac{\partial \sigma}{\partial t} + \frac{1}{r}\frac{\partial (r\mu_\sigma \sigma E_r)}{\partial r} + \frac{\partial (\mu_\sigma \sigma E_z)}{\partial z} - \frac{D_r}{r}\frac{\partial}{\partial r}\left(r\frac{\partial \sigma}{\partial r}\right) - D_z\frac{\partial^2 \sigma}{\partial z^2} = S|\mathbf{E}|e^{K/|\mathbf{E}|}\sigma, \\ \frac{\partial \rho}{\partial t} + \frac{1}{r}\frac{\partial (r\mu_\rho \rho E_r)}{\partial r} + \frac{\partial (\mu_\rho \rho E_z)}{\partial z} = S|\mathbf{E}|e^{K/|\mathbf{E}|}\sigma, \\ -\frac{1}{r}\frac{\partial}{\partial r}\left(r\frac{\partial \phi}{\partial r}\right) - \frac{\partial^2 \phi}{\partial z^2} = \rho - \sigma,\ \mathbf{E} = (E_r, E_z)^T = \left(-\frac{\partial \phi}{\partial r}, -\frac{\partial \phi}{\partial z}\right)^T. \end{cases} \tag{1.6}$$

Since the solutions are independent of θ, we can take any longitudinal section to form the two-dimensional domain as shown in the following figure,

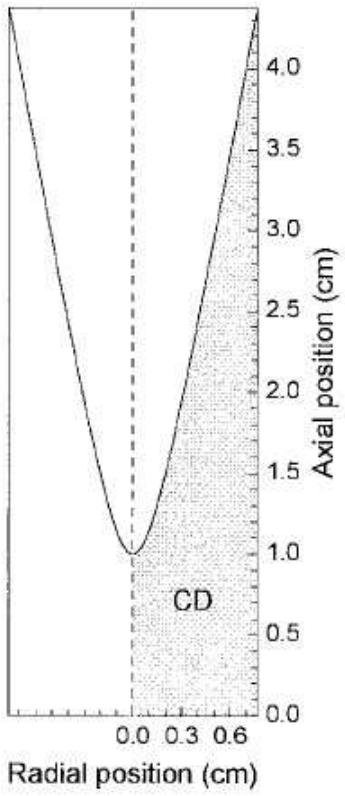

Fig. 1. Sketch of the electrodes and computational domain. The hyperboloid anode is 1 cm above the plane. Computational domain (CD) is the shaded region.

Figure 1.2: The computational domain of quasi 3D model. This figure is cited from [47].

From Figure 1.2, we can see that, in (1.6), the range for axial variable z is still between the electrodes, so the boundary conditions for Poisson's equation in the axial direction (i.e. z-direction) are remained the same. In the physical domain, the range for radial variable r is $[0, \infty]$. Therefore, the quasi 3D model involves a singularity along axis, which is the main difficulty in this model. Besides, it is a half space problem in the radial direction (i.e. r-direction), hence we impose homogeneous Neumann boundary condition for each equation along the z-axis,

$$\frac{\partial \sigma}{\partial r} = \frac{\partial \rho}{\partial r} = \frac{\partial \phi}{\partial r} = 0, \quad \text{at } r = 0. \tag{1.7}$$

1.2.3 Two-dimensional model

Apart from the quasi 3D model, another way to reduce dimension is to make an assumption that the electrodes have infinite length in one direction (say z-direction) and the anode is charged everywhere. Then the discharge will be independent of z-variable. Thus, we can take any cross section (which means to ignore the z-variable) to form a two-dimensional (2D) model under Cartesian coordinates [92]. Then this model reads,

$$\begin{cases} \frac{\partial \sigma}{\partial t} + \frac{\partial(\mu_\sigma \sigma E_x)}{\partial x} + \frac{\partial(\mu_\sigma \sigma E_y)}{\partial y} - D_x \frac{\partial^2 \sigma}{\partial x^2} - D_y \frac{\partial^2 \sigma}{\partial y^2} = S|\mathbf{E}|e^{K/|\mathbf{E}|}\sigma, \\ \frac{\partial \rho}{\partial t} + \frac{\partial(\mu_\rho \rho E_x)}{\partial x} + \frac{\partial(\mu_\rho \rho E_y)}{\partial y} = S|\mathbf{E}|e^{K/|\mathbf{E}|}\sigma, \\ -\left(\frac{\partial^2 \phi}{\partial x^2} + \frac{\partial^2 \phi}{\partial y^2}\right) = \rho - \sigma, \ \mathbf{E} = (E_x, E_y)^T = \left(-\frac{\partial \phi}{\partial x}, -\frac{\partial \phi}{\partial y}\right)^T. \end{cases} \tag{1.8}$$

A typical example of this 2D model is a charged wire with infinite length in a cylinder which is connected to the earth ground. Then the computational domain is between two concentric circles.

1.2.4 Quasi two-dimensional model

To illustrate our numerical methods and to study the advantage and disadvantage of each method, we will demonstrate the numerical tests and comparisons of different

methods when they are applied to the quasi two-dimensional (quasi 2D) model,

$$\begin{cases} \frac{\partial \sigma}{\partial t} + \frac{1}{r}\frac{\partial (r\mu_\sigma \sigma E)}{\partial r} - \frac{D}{r}\frac{\partial}{\partial r}\left(r\frac{\partial \sigma}{\partial r}\right) = S|E|e^{K/|E|}\sigma, \\ \frac{\partial \rho}{\partial t} + \frac{1}{r}\frac{\partial (r\mu_\rho \rho E)}{\partial r} = S|E|e^{K/|E|}\sigma, \\ -\frac{1}{r}\frac{\partial}{\partial r}\left(r\frac{\partial \phi}{\partial r}\right) = \rho - \sigma, E = -\frac{\partial \phi}{\partial r}. \end{cases} \tag{1.9}$$

This model can be regarded as a reduction from a 2D model with central symmetry using polar coordinates to change the spatial variables.

1.2.5 One-dimensional model

We will also demonstrate our numerical tests and comparisons of different methods for the one-dimensional (1D) model,

$$\begin{cases} \frac{\partial \sigma}{\partial t} + \frac{\partial (\mu_\sigma \sigma E)}{\partial z} - D\frac{\partial^2 \sigma}{\partial z^2} = S|E|e^{K/|E|}\sigma, \\ \frac{\partial \rho}{\partial t} + \frac{\partial (\mu_\rho \rho E)}{\partial z} = S|E|e^{K/|E|}\sigma, \\ -\frac{\partial^2 \phi}{\partial z^2} = \rho - \sigma, E = -\frac{\partial \phi}{\partial z}, \end{cases} \tag{1.10}$$

This model is an extreme case under dimensionality reduction.

1.2.6 1.5-dimensional model

If one further assumes in the quasi 3D model that the particle densities only vary in z-direction and are constant along the r-direction with a fixed radius, then the quasi 3D model will be reduced to a 1.5-dimensional (1.5D) model [7, 28, 63]. In this model, the continuity equations have only one dimension which makes them easy to solve, but the Poisson's equation still have to be solved in 2D cylindrical coordinate system. Fortunately, due to the assumption, the Poisson's equation can be solved by the disc method. Suppose that the dimensionless gap length is 1. Let us compute the modified electric field $\mathbf{E}_m(z)$ for any position $z \in [0, 1]$ in this gap. Assume that there is a very thin disc located at $z' \in [0, 1]$ with net particle density

$n(z')$, radius r_d and thickness dz', then this charged disc can generate an electric field at z by

$$\left[0, 0, \frac{1}{2} n(z') \left(\frac{z - z'}{|z - z'|} - \frac{z - z'}{\sqrt{(z - z')^2 + r_d^2}} \right) dz' \right]^T .$$

Thus, $\mathbf{E}_m(z)$ can be obtained by direct integration over all discs,

$$\mathbf{E}_m(z) = \left[0, 0, \frac{1}{2} \int_0^1 n(z') \left(\frac{z - z'}{|z - z'|} - \frac{z - z'}{\sqrt{(z - z')^2 + r_d^2}} \right) dz' \right]^T .$$

Note that, only the third component of modified electric field will be used to solve continuity equations; we will denote it by $E_m(z)$ and call it modified electric field hereafter.

To ensure the zero potential at the ends of the gap, we have to add infinite series of image discharges into the integration theoretically [22]. However, in fact, we only consider the image charge up to few neighboring intervals by using the reflection [28, 102]. Then the final formula to compute the modified electric field should be

$$\begin{aligned} E_m(z) &= \frac{1}{2} \left[\int_{-L}^{z} n(z') \left(1 - \frac{z - z'}{\sqrt{(z - z')^2 + r_d^2}} \right) dz' \right. \\ &\quad \left. + \int_{z}^{1+L} n(z') \left(-1 - \frac{z - z'}{\sqrt{(z - z')^2 + r_d^2}} \right) dz' \right], \end{aligned}$$

where $n(z')$ for $z' \in [-L, 0] \cup [1, 1 + L]$ is computed by reflection. The total electric field should be a combination of modified electric field E_m and applied electric field E_a,

$$E = E_m + E_a,$$

where E_a is a constant if the gap is between two parallel planar electrodes or is given by [31] if the gap is between a pointed and a planar electrode.

As mentioned in [71], it could take at least 90 per cent of total computational time to solve the Poisson's equation in 2D or quasi 3D model numerically. Thus, 1.5D model certainly can simplify and speed up the simulations. Therefore, 1.5D model is usually considered by engineers and physicists to make a balance between engineering and numerical simulation. However, the solution to this model strongly

depends on the values of radius r_d. It is believed that this empirical value should vary for different discharge configurations. In addition, we will see later in Chapter 5 that 1.5D model cannot correctly describe streamer propagation. Hence, we do not want to make great effort to study 1.5D model, although we admit the simplicity of this model. As a result, we will mainly focus on 2D and quasi 3D models in this thesis.

1.3 Literature Review

In recent years, many different numerical methods have been developed to find the approximated solutions of the streamer propagation models introduced in the previous section. In this section, we will first review the results for the 1.5D model and then those for 2D and quasi 3D models.

The earliest numerical study of 1.5D model was done by R. Morrow and J. J. Lowke in 1981 [64]. They used finite difference method to study the negative streamer. They studied a 3cm short gap, and chose a two-step Lax-Wendroff scheme with CFL number 0.05 in spatial discretization. However, they only considered a convection-diffusion system without the ionization source and other effective sources.

After Morrow's first attempt, it became popular to seek numerical solutions of 1.5D model in streamer research. For example, D. Bessières *et al.* (2007) used finite volume method to study negative streamer in a 1cm gap [7]. Although a short gap was considered in this study, they used an adaptive mesh refinement method, called moving mesh method [89], to save the computing time. Their method can be 16 times faster than using uniform mesh [7]. As members of Bessières' group, A. Bourdon *et al.* considered the positive streamer discharges using finite volume method [28]. In their studies, they considered not only ionization source but also attachment, detachment and recombination effects. They also used adaptive refinement technique [21] in space. Besides, in time discretization, a second order Strang operator splitting scheme together with time adaptive integration was used

to increase the accuracy. This study has successfully simulated the propagation of streamer in short gap under different physical configurations.

The continuity equation for electrons in 2D and quasi 3D models is convection dominated if the source terms are not taken into consideration. At the beginning, traditional linear finite difference schemes were used to solve the continuity equations, e.g. Morrow and Lowke's work [64] mentioned above. However, it has been proved in [40, 41] that the those schemes will generate too many numerical oscillations or diffusions. Consequently, Morrow and Lowke's results became unstable in long time simulation.

To overcome the drawback of traditional linear finite difference scheme, flux corrected transport (FCT) technique [11, 12, 99] was applied to finite difference method (FDM) during 1980s and 1990s [25, 26, 64, 97]. The simulation results have shown that the FCT technique can significantly suppress the numerical oscillations [97]. For instant, S. K. Dhali and P. F. Williams studied the discharges in a 0.5cm gap of $SF_6 - N_2$ mixtures between two parallel planar electrodes in 1987 [26]. They attempted to change the attachment coefficient, applied voltage and initial particle distributions to study the effects of these parameters on the discharge processes and the features during streamer development. They have pointed out that the initial status could seldom affect the stationary status of streamers.

However, it is hard for FDM to handle the unstructured meshes or complex geometries. Therefore, after R. Löhner's works in 1988 [53, 54], FCT had been combined to finite element method (FEM) [35, 36, 37, 60, 61]. For example, in 2000, G. E. Georghiou *et al.* considered positive streamer modeled by (1.1) with two dimensions [37]. In their study, they generated an unstructured grid on which there are 4,300 unknowns. However, they only dealt with a 2mm gap, which is too short. As an improvement of Georghiou's work, W.-G. Min *et al.* [61] used the more efficient adaptive mesh refinement method [52] in 2001. Their method can handle a triangular mesh containing up to 8,923 elements. Meanwhile, the length of gap was increased to 5mm. However, Min's simulation was conducted on negative streamer

with only the ionization source, and the refinement procedure was not very efficient.

The good news for FEM-FCT was that FEM could maintain a comparable accuracy as FDM-FCT and was easy to implement on unstructured meshes or complex geometries. But on the other hand, FEM can only conserve the total current instead of the local current [101]; thus, Maxwell's law of total currents is violated. To enforce local current conservation, finite volume method (FVM) becomes popular since 2000 [7, 29, 62, 71].

O. Ducasse *et al.* made progress based on Georghiou's work [37] through the FVM with MUSCL scheme in 2007 [29]. In their study, they also used FEM-FCT method for comparison purpose. Compared with Georghiou's work, they can deal with more unknowns: an unstructured mesh with 16,018 grids in FEM-FCT and a rectangular mesh with 68,769 grids in FVM-FCT. Besides, their computational domain was a complex region, one of whose boundaries is a hyperbola, while Georghiou *et al.* only dealt with a rectangular region. However, the only problem is that they only considered a 1.21mm gap, which was shorter than Georghiou's.

A successful attempt for long gap simulation was made by C. Montijn *et al.* in 2006 [62]. They used the finite volume method for both Poisson's equation and continuity equations. In order to save cost, they also proposed an adaptive mesh refinement strategy such that the Poisson's equation had 93,584 unknowns and each continuity equation had 657,856 unknowns in a 7.5cm gap. However, they only focused on the minimal model (1.6) without the convection term in the continuity equation for positive ions and did not use a precise dimensionless analysis so that their method cannot be extended to other cases.

FVM-FCT was applied in 3D simulations as well. S. Pancheshnyi *et al.* used finite volume method for both the Poisson's equation and continuity equations to carry out a pioneer 3D simulation in 2008 [71]. To save the computer cost, both an adaptive mesh refinement strategy [58] and multi-node parallel implementation are necessary. They used 6 clusters to simulate the propagation of negative streamer modeled by (1.6) in a cubic gap $[-0.25mm, 0.25mm] \times [0, 0.5mm] \times [-0.25mm, 0.25mm]$.

Comparing with FEM, FVM needs a wider stencil to construct high order scheme which will make computation inefficient. This difficulty is caused by the discretization of the diffusion term in FVM on triangular mesh. For example, R. Herbin introduced a four-point FVM scheme to discretize the diffusion term [43]. But his method only had first order accuracy. Therefore, we can see that the simulations done by D. Bessières, O. Ducasse, C. Montijn, S. Pancheshnyi and *et al.* were all based on rectangular meshes.

At the same time, the numerical methods for solving the Poisson's equation is another issue in this thesis. Scientists have made some efforts on this issue. For example in O. Ducasse and his colleagues' work [29], they used finite element method with BiCGSTAB algorithm and finite volume method with Chebyshev SOR algorithm to solve Poisson's equation. They pointed out that the latter scheme is easier to implement and more efficient in simple geometries and the former one required optimization work to reduce both the computational time and memory [29].

The author and his collaborators from Tsinghua University have also done some research work in comparing numerical methods for Poison's equation [44]. They have concluded that the finite difference method (FDM) [7, 62] and discontinuous Galerkin (DG) method [5, 95], the mixed finite element method (MFEM) [14, 15] and least-squares finite element method (LSFEM) [8, 9] can be successfully applied to solve Poisson's equation for 1D model (1.10) and quasi 2D model (1.9). The differences among these methods are as follows. The FDM and DG method directly solve the Poisson's equation, and use the derivative of the numerical solution to approximate the electric field. Conversely, MFEM and LSFEM regard the electric field as an independent variable, thus these two methods can directly derive a solution of high accuracy for electric field since it is the electric field coupled with continuity equations rather than electric potential. When these methods are extended to higher dimensions, FDM will be restricted in rectangular meshes but MFEM and LSFEM can be applied to triangular meshes while DG method is flexible in both

kinds of meshes.

Summarizing the above review, we can conclude that negative streamer has been studied more than positive streamer and short gap (order of millimeters) is considered more than long gap.

1.4 Purpose

As mentioned in Section 1.1, streamer incepts and develops in a time scale of several nanoseconds; hence, experiments are not adequate to study the detailed mechanism and process. Therefore, numerical simulation has begun to play a critical role in this field.

The commonly used model is the fluid model in which the continuity equations are convection dominated if we temporarily ignore the effect of source terms. When solving them, traditional linear numerical schemes usually suffer from numerical dissipation or dispersion or both. On one hand, we usually consider a Gaussian type initial data with steep gradient. It has been found in [62, 104] that the solution of streamer model has large derivatives or even has discontinuities if the gap becomes longer. Dissipative schemes cannot capture this feature and lead to numerical diffusions during simulation. Therefore, a numerical scheme which is able to capture large derivative and discontinuity is required. On the other hand, dispersive schemes will generate numerical oscillations which can make solution inaccurate. This disadvantage usually exists in some higher order schemes which are of high resolution in space and are able to capture huge gradient. Therefore, a numerical algorithm is required to control these oscillations.

As we have seen in Section 1.3, FD-FCT, FEM-FCT and FVM are sequentially applied to solve continuity equations in history. But they have their own disadvantages, such as loss of local conservation and lack of easy extension to complex geometries. Thus, the first purpose of our study is to develop a numerical algorithm which can precisely resolve streamer propagation, can preserve the local conservation

and can be easily extended to complex geometries and unstructured meshes.

To achieve our goals, the so-called Oden-Babuška-Baumann discontinuous Galerkin (OBBDG) method [24, 70, 84] and local discontinuous Galerkin (LDG) method [18, 19, 20, 102] will be applied to solve continuity equations. Both methods are discontinuous Galerkin (DG) methods which use finite element space discretization but allow the solution to have discontinuities along the interface of adjoint elements. Consequently, both methods can capture the discontinuity of the solution, enforce the local conservation, achieve high accuracy and handle the complex regions; in other words, they possess the advantages of FEM and FVM simultaneously. Furthermore, both methods can control the numerical oscillations with the help of a slope limiter [18, 19, 46].

Our second purpose in this thesis is to extend our comparison study on numerical methods for Poisson's equation in 1D and quasi 2D models [44] to 2D and quasi 3D models. We will study the numerical compatibility in the coupling between Poisson's equation and hyperbolic system.

Finally, as mentioned in Section 1.3, most existing simulations were carried out for short gaps; thus, our third purpose is to enlarge the physical domain and elongate the streamer propagation. We choose some typical configurations which are widely used in many literatures and considered longer gaps. Our simulations exhibit some interesting phenomenon and conclude more features during streamer propagation.

Moreover, this thesis could be regarded as a support in the algorithm level to the previous works [101, 104] which lack of convergence result for the numerical methods.

1.5 Outline

This thesis is organized as follows: numerical methods for 1D and quasi 2D models are introduced and compared to study their feasibilities in Chapter 2 and Chapter 3 respectively. Based on the comparison results in Chapter 2 and 3, we will apply

suitable methods to long gap simulations for 2D and quasi 3D models in Chapter 4 and Chapter 5. In particular, the relationship between quasi 3D and 1.5D models will be discussed in Chapter 5. Finally, discussions and conclusions will be presented in Chapter 6.

Chapter 2

Numerical Methods and Results for 1D Model

In this chapter, let us consider the 1D model (1.10)

$$\begin{cases} \frac{\partial \sigma}{\partial t} + \frac{\partial(\mu_\sigma \sigma E)}{\partial z} - D\frac{\partial^2 \sigma}{\partial z^2} = S|E|e^{K/|E|}\sigma, \\ \frac{\partial \rho}{\partial t} + \frac{\partial(\mu_\rho \rho E)}{\partial z} = S|E|e^{K/|E|}\sigma, \\ -\frac{\partial^2 \phi}{\partial z^2} = \rho - \sigma, E = -\frac{\partial \phi}{\partial z}, \end{cases} \tag{2.1}$$

where $(z,t) \in (0,1) \times (0,T)$, and the initial and boundary conditions are posed by

$$\sigma(z,0) = \sigma_0(z),\ \rho(z,0) = \rho_0(z),\ z \in (0,1);$$

$$\phi(0,t) = 0,\ \phi(1,t) = 1;\ \frac{\partial \sigma}{\partial z}(0,t) = \frac{\partial \sigma}{\partial z}(1,t) = \frac{\partial \rho}{\partial z}(0,t) = \frac{\partial \rho}{\partial z}(1,t) = 0.$$

Note that there is an artificial boundary condition for ρ since the equation for ρ is a first order advection equation. This artificial boundary condition will be used to compute numerical flux and slope limiter later.

With the time step size τ, the numerical algorithm is as follows. Assume at any time level $t^n = n\tau$, we have the numerical solutions for particle densities, σ^n and ρ^n. Then we use σ^n and ρ^n to solve the Poisson's equation numerically to obtain ϕ^n. After that, we plug a proper numerical approximation of E^n into continuity

equations to solve for σ^{n+1} and ρ^{n+1}. This process will be continued until $t^{n+1} \geq T$. We will use this algorithm in the later chapters.

Let $0 = z_0 < z_1 < \cdots < z_N = 1$ be a uniform spatial partition of the computational domain $[0, 1]$ such that $z_j = jh$ where $h = \frac{1}{N}$ for $j = 0, 1, \cdots, N$. Denote the subintervals by $I_j = [z_j, z_{j+1}]$, $j = 0, 1, \cdots, N-1$. Let N_i, N_d and N_n denote the sets of labels of interior, Dirichlet boundary and Neumann boundary nodes respectively.

2.1 Numerical methods for Poisson's equation

In this section, we apply three methods to solve Poisson's equation in model (2.1): finite difference method (FDM) [7, 62], discontinuous Galerkin (DG) methods [5, 95] and least-squares finite element method (LSFEM) [8, 9].

In fact, the solution to the original Poisson's equation contains temporal variable t. However, in our iterative numerical algorithm, the Poisson's equation is solved when the right hand side $\rho - \sigma$ is given. Therefore, we consider the Poisson's equation to be independent of temporal variable, namely,

$$-\frac{d^2\phi}{dz^2} = \rho^n - \sigma^n, E = -\frac{d\phi}{dz}.$$

2.1.1 The finite difference method

In this method, the numerical solution for electric potential, ϕ_j is defined in the center of element I_j. The standard second order central difference method reads,

$$-\frac{\phi^n_{j-1} - 2\phi^n_j + \phi^n_{j+1}}{h^2} = \rho^n_j - \sigma^n_j, \text{ for } j = 0, 1, \cdots, N-1, \tag{2.2}$$

where ρ^n_j and σ^n_j are the approximate values of ρ and σ in element centers respectively. The boundary conditions are strongly imposed by introducing ghost cells and linear interpolation,

$$\phi^n_{-1} = 2\phi(0, t^n) - \phi^n_0, \ \phi^n_N = 2\phi(1, t^n) - \phi^n_{N-1}. \tag{2.3}$$

After obtaining the numerical electric potential ϕ, the numerical electric field at each node is defined by

$$E^n|_{z_j} = \frac{\phi^n_{j-1} - \phi^n_j}{h}, \text{ for } j = 0, 1, \cdots, N; \tag{2.4}$$

and the numerical electric field in each element is defined by a constant,

$$E^n|_{I_j} = \frac{\phi^n_{j-1} - \phi^n_{j+1}}{2h}, \text{ for } j = 0, 1, \cdots, N-1. \tag{2.5}$$

2.1.2 The discontinuous Galerkin method

Since this method allows the numerical solution to have discontinuity on the interior nodes, we need to define the numerical solution on each subinterval. Consequently, denote the finite element space by

$$V_k = \{v : v|_{I_j} \in \mathbb{P}_k(I_j), \text{ for } j = 0, 1, \cdots, N-1\}, \tag{2.6}$$

where $\mathbb{P}_k(I_j)$ is the space of polynomials of degree up to k on I_j.

The discontinuity also suggests us to define the average, $\{v\}$, and the jump, $[v]$, of the solution v at each interior node z_j,

$$[v(z_j)] = v(z_j^-) - v(z_j^+), \ \{v\} = \frac{1}{2}[v(z_j^-) + v(z_j^+)], \ \forall j = 1, 2, \cdots, N-1, \tag{2.7}$$

where $v(z^\pm) = \lim_{\epsilon \to 0^+} v(z \pm \epsilon)$. We need to extend the definition of average and jump to the endpoints as well,

$$[v(z_0)] = -v(z_0^+), \ \{v(z_0)\} = v(z_0^+), \ [v(z_N)] = v(z_N^-), \ \{v(z_N)\} = v(z_N^-). \tag{2.8}$$

Define the bilinear form $B_\epsilon : V_k \times V_k \to \mathbb{R}$,

$$\begin{aligned} B_\epsilon(u, v) \ = \ & \sum_{j=0}^{N-1} \int_{I_j} \frac{du}{dz}\frac{dv}{dz} - \sum_{j \in N_i \cup N_d} \left\{ \frac{du}{dz}(z_j) \right\} [v(z_j)] \\ & + \epsilon \sum_{j \in N_i \cup N_d} \left\{ \frac{dv}{dz}(z_j) \right\} [u(z_j)] + \sum_{j \in N_i \cup N_d} \frac{\alpha}{h^\beta} [u(z_j)][v(z_j)], \end{aligned} \tag{2.9}$$

and linear functional $L : V_k \to \mathbb{R}$,

$$L(v) = \int_0^1 (\rho^n - \sigma^n)v + \left(\epsilon \frac{dv}{dz}(z_N) + \frac{\alpha}{h^\beta} v(z_N)\right) \phi(1, t^n). \tag{2.10}$$

Then the DG method is to find $\phi^h \in V_k$ such that

$$B_\epsilon(\phi^h, v) = L(v), \ \forall v \in V_k. \tag{2.11}$$

The DG method has different properties depending on the choice of parameters ϵ, α and β in (2.9). In comparison and practice, we choose $\epsilon = -1$ to form a symmetric linear system which is called symmetric interior penalty Galerkin method (SIPG) and then choose $\alpha = 2$ and $\beta = 1$ to ensure optimal convergence.

Compared with the continuous Galerkin method, we introduce extra interior terms in the scheme; therefore, the electric field is approximated by

$$E^n(z_j) = -\left\{\frac{d\phi^h}{dz}(z_j)\right\} + \frac{\alpha}{h^\beta}[\phi^h(z_j)], \text{ for } j = 1, 2, \cdots, N-1, \tag{2.12}$$

and at the boundary

$$\begin{aligned} E^n(z_0) &= -\frac{d\phi^h}{dz}(z_0) + \frac{\alpha}{h^\beta}(\phi(0, t^n) - \phi^h(z_0)), \\ E^n(z_N) &= -\frac{d\phi^h}{dz}(z_N) + \frac{\alpha}{h^\beta}(\phi^h(z_N) - \phi(1, t^n)). \end{aligned} \tag{2.13}$$

Remark 1. This DG scheme comes directly from the first chapter of [84] in which the derivation of DG scheme is thoroughly introduced.

Remark 2. Note that, in this DG scheme, the jump in both artificial terms (symmetric and penalty terms) is used for numerical solution. Therefore, the scheme is automatically consistent with the weak formulation of Poisson's equation. Furthermore, both artificial terms become weaker when the mesh is finer. In other words, the artificial terms will not affect the convergence of numerical solution for fixed values of artificial parameters.

Remark 3. As suggested in [84] that SIPG can provide optimal convergence rate for all degrees of approximation polynomials compared with non-symmetric interior penalty Galerkin (NIPG, $\epsilon = 1$) and incomplete interior penalty Galerkin (IIPG,

$\epsilon = 0$) methods. Besides, the penalty parameter α in SIPG should be larger than some threshold; otherwise, the numerical solution will not converge to the exact solution.

2.1.3 The least-squares finite element method

This method reformulates the Poisson's equation by a first order differential equation system,

$$\begin{cases} \frac{dE}{dz} = \rho^n - \sigma^n, \\ -\frac{d\phi}{dz} = E, \end{cases} \tag{2.14}$$

then we can treat ϕ and E as independent variables. Usually, we call ϕ the scalar variable and E the flux variable.

Denote the C^0 nodal finite element space by

$$W_k = \{v : v|_{I_j} \in \mathbb{P}_k(I_j), \text{ for } j = 0, 1, \cdots, N-1, \text{ v is continuous in [0,1]}\}.$$

Let

$$W_k^0 = W_k \cap \{v : v(0) = v(1) = 0\},$$

$$W_k^S = W_k \cap \{v : v(0) = \phi(0, t^n), v(1) = \phi(1, t^n)\},$$

and $W_k^F = W_k$ be the spaces for test functions, scalar variable and flux variable respectively.

LSFEM is to minimize a functional

$$J(\phi, E) = \left|\left|\frac{dE}{dz} - (\rho^n - \sigma^n)\right|\right|^2_{L^2(0,1)} + \left|\left|E + \frac{d\phi}{dz}\right|\right|^2_{L^2(0,1)}$$

on $W_k^S \times W_k^F$. By taking the first variation of $J(\phi, E)$, we can find that

$$\begin{aligned}
&\left.\frac{dJ(\phi + t\psi, E + tw)}{dt}\right|_{t=0} \\
= &\left.\frac{d}{dt}\left\{\int_0^1 \left[\frac{d(E+tw)}{dz} - (\rho^n - \sigma^n)\right]^2 + \int_0^1 \left[(E+tw) + \frac{d(\phi+t\psi)}{dz}\right]^2\right\}\right|_{t=0} \\
= &\left. 2\int_0^1 \left[\frac{d(E+tw)}{dz} - (\rho^n - \sigma^n)\right]\frac{dw}{dz} + 2\int_0^1 \left[(E+tw) + \frac{d(\phi+t\psi)}{dz}\right]\left(w + \frac{d\psi}{dz}\right)\right|_{t=0} \\
= &\ 2\int_0^1 \left[\frac{dE}{dz} - (\rho^n - \sigma^n)\right]\frac{dw}{dz} + 2\int_0^1 \left(E + \frac{d\phi}{dz}\right)\left(w + \frac{d\psi}{dz}\right),
\end{aligned}$$

for all $\psi \in W_k^0$ and $w \in W_k^F$. Setting this first variation of $J(\phi, E)$ to be zero, we have

$$\int_0^1 \frac{dE}{dz}\frac{dw}{dz} + \int_0^1 \left(E + \frac{d\phi}{dz}\right)\left(w + \frac{d\psi}{dz}\right) = \int_0^1 (\rho^n - \sigma^n)\frac{dw}{dz}.$$

Therefore, the least-squares finite element method is to find $(\phi^h, E^h) \in (W_k^F \times W_k^S)$ such that

$$B[(\phi^h, E^h), (\psi, w)] = L(w),\ \forall (w, \psi) \in (W_k^F \times W_k^0), \tag{2.15}$$

where the bilinear form $B[(\phi, E), (\psi, w)]$ is defined by

$$B[(\phi, E), (\psi, w)] = \int_0^1 \frac{dE}{dz}\frac{dw}{dz} + \int_0^1 \left(E + \frac{d\phi}{dz}\right)\left(w + \frac{d\psi}{dz}\right), \tag{2.16}$$

and the linear functional $L(w)$ is defined by

$$L(w) = \int_0^1 (\rho^n - \sigma^n)\frac{dw}{dz}. \tag{2.17}$$

Since the flux variable E^h is continuous in this method, the approximate electric field is naturally chosen as $E^n = E^h$.

2.2 Numerical methods for continuity equations

As mentioned in Chapter 1, we apply Oden-Babuška-Baumann discontinuous Galerkin (OBBDG) method [24, 70, 84] and local discontinuous Galerkin (LDG) method [18, 19, 20] from the DG class to solve the continuity equations.

In this section, we will approximate the solutions $\sigma(t)$ and $\rho(t)$ by functions $\sigma^h(t)$ and $\rho^h(t)$ that belong to V_k for all $t \geq 0$. The solutions $\sigma^h(t)$ and $\rho^h(t)$ are referred as the semidiscrete solutions.

2.2.1 The Oden-Babuška-Baumann DG method

In the OBBDG method, firstly, the diffusion term $-D\frac{\partial^2\sigma}{\partial z^2}$ will be discretized by the bilinear form (2.9) with symmetric parameter $\epsilon = 1$ and penalty parameter $\alpha = 0$. Due to the homogeneous Neumann boundary condition, we only consider the interior nodes:

$$B(u,v) = \sum_{j=0}^{N-1} \int_{I_j} D\frac{du}{dz}\frac{dv}{dz} - \sum_{j\in N_i} \left\{ D\frac{du}{dz}(z_j) \right\} [v(z_j)] + \sum_{j\in N_i} \left\{ D\frac{dv}{dz}(z_j) \right\} [u(z_j)]. \tag{2.18}$$

Secondly, the convection terms $\frac{\partial(\mu_P PE)}{\partial z}$ for $P = \sigma$ or ρ will be approximated by an upwind discretization. Denote the upwind value of P by

$$\widehat{P}(z) = \begin{cases} P(z^-), & \text{if } \mu_P E(z) \geq 0, \\ P(z^+), & \text{if } \mu_P E(z) < 0. \end{cases} \tag{2.19}$$

The dependence of the upwind discretization C on E is given by

$$\begin{aligned} C(P,v;E) &= -\sum_{j=0}^{N-1} \int_{I_j} P\mu_P E\frac{dv}{dz} \\ &\quad + \sum_{j\in N_i} \widehat{P}(z_j)\mu_P E(z_j)[v(z_j)] + \sum_{j\in N_n} [P(z_j)\mu_P E(z_j)v(z_j)]. \end{aligned} \tag{2.20}$$

Thirdly, the source term $S|E|e^{K/|E|}\sigma$ is discretized by a linear form

$$L(\sigma, v; E) = \int_0^1 S|E|e^{K/|E|}\sigma v. \tag{2.21}$$

Finally, the semidiscrete scheme of OBBDG method is to find $\sigma^h(t), \rho^h(t) \in V_k$ such that

$$\int_0^1 (\sigma^h(0) - \sigma_0(z))v = \int_0^1 (\rho^h(0) - \rho_0(z))v = 0, \ \forall v \in V_k; \tag{2.22}$$

and

$$\begin{aligned}\int_0^1 \frac{\partial \sigma^h}{\partial t} v + C(\sigma^h(t), v; E(t)) + B(\sigma^h(t), v) = L(\sigma^h(t), v; E(t)),\ \forall v \in V_k,\\ \int_0^1 \frac{\partial \rho^h}{\partial t} v + C(\rho^h(t), v; E(t)) = L(\sigma^h(t), v; E(t)),\ \forall v \in V_k,\end{aligned} \tag{2.23}$$

for $t > 0$.

2.2.2 The local discontinuous Galerkin method

The diffusion term is directly discretized in the OBBDG method. In the LDG method, an auxiliary variable is introduced to convert diffusion term to a first order term; and the new equation for the auxiliary variable is also of first order.

More precisely, the auxiliary variable is

$$q = \frac{\partial \sigma}{\partial z}.$$

Hence, the continuity equations are converted into

$$\begin{cases} \frac{\partial \sigma}{\partial t} + \frac{\partial(\mu_\sigma \sigma E - Dq)}{\partial z} = S|E|e^{K/|E|}\sigma, \\ \frac{\partial \rho}{\partial t} + \frac{\partial(\mu_\rho \rho E)}{\partial z} = S|E|e^{K/|E|}\sigma, \\ q = \frac{\partial \sigma}{\partial z}. \end{cases} \tag{2.24}$$

The source term is also discretized by the same linear form in OBBDG method,

$$L(\sigma, v; E) = \int_0^1 S|E|e^{K/|E|}\sigma v.$$

Then the LDG method is to find $\sigma^h(t), \rho^h(t), q^h(t) \in V_k$ such that

$$\int_0^1 (\sigma^h(0) - \sigma_0(z))v = \int_0^1 (\rho^h(0) - \rho_0(z))v = 0,\ \forall v \in V_k; \tag{2.25}$$

and

$$\int_0^1 q^h(t)v = \sum_{j=0}^{N} \widehat{\sigma^h}(z_j)[v(z_j)] - \sum_{j=0}^{N-1} \int_{I_j} \sigma^h(t)\frac{dv}{dz},\ \forall v \in V_k, \tag{2.26}$$

$$\begin{aligned}\int_0^1 \frac{\partial \sigma^h}{\partial t} v \;&+\; S\sum_{j=0}^{N}\big(\mu_\sigma E(z_j)\widetilde{\sigma^h}(z_j) - D\widehat{q^h}(z_j)\big)[v(z_j)] \\ &-\; \sum_{j=0}^{N-1}\int_{I_j}(\sigma^h\mu_\sigma E(t) - Dq^h)\frac{dv}{dz} \\ &=\; L(\sigma^h(t), v; E(t)),\ \forall v \in V_k, \end{aligned} \tag{2.27}$$

$$\begin{aligned}\int_0^1 \frac{\partial \rho^h}{\partial t} v \;&+\; \sum_{j=0}^{N}\big(\mu_\rho E(z_j)\widetilde{\rho^h}(z_j)\big)[v(z_j)] - \sum_{j=0}^{N-1}\int_{I_j}\rho^h\mu_\rho E(t)\frac{dv}{dz} \\ &=\; L(\sigma^h(t), v; E(t)),\ \forall v \in V_k, \end{aligned} \tag{2.28}$$

for all $t > 0$.

In (2.26)-(2.28), the numerical flux in convection terms is also defined by

$$\widetilde{P^h}(z) = \begin{cases} P^h(z^-), & \text{if } \mu_P E(z) \geq 0, \\ P^h(z^+), & \text{if } \mu_P E(z) < 0, \end{cases}$$

for $P = \sigma$ or ρ. The numerical fluxes, $\widehat{\sigma^h}$ and $\widehat{q^h}$, defined in discretization of diffusion term and auxiliary equation are chosen according to the alternating principle, i.e.,

$$\widehat{\sigma^h}(z) = \sigma^h(z^+),\ \widehat{q^h}(z) = q^h(z^-), \tag{2.29}$$

or

$$\widehat{\sigma^h}(z) = \sigma^h(z^-),\ \widehat{q^h}(z) = q^h(z^+), \tag{2.30}$$

to ensure the stability and conservation law in semidiscrete level.

Remark 1. One may refer to [18] for the detailed derivation of LDG scheme and the proof of stability.

Remark 2. Because the boundary conditions for the equation of σ are

$$\frac{\partial \sigma}{\partial z}(0,t) = \frac{\partial \sigma}{\partial z}(1,t) = 0,$$

the boundary conditions for the auxiliary equation $q = \frac{\partial \sigma}{\partial z}$ should be

$$q(0,t) = q(1,t) = 0.$$

However, this auxiliary equation is a first order equation. Thus, we only use one boundary condition according to the choice of $\widehat{q^h}$.

2.2.3 Fully discrete formulation

We choose some local basis functions of $\mathbb{P}_k(I_j)$ such that

$$\mathbb{P}_k(I_j) = span\{P_0, P_1, \cdots, P_k\},$$

for all subintervals I_j. Then the global basis functions $\{\Phi_{j,l}\}$ for finite element space V_k are defined by extending the local basis functions in the following way:

$$\Phi_{j,l}(z) = \begin{cases} P_l(z), & \text{if } z \in I_j, \\ 0, & \text{otherwise.} \end{cases}$$

Therefore, the DG solutions can be expanded by

$$P^h(z,t) = \sum_{j=0}^{N-1} \sum_{l=0}^{k} c_{j,l}(t)\Phi_{j,l}(z),$$

for $P^h(t) = \sigma^h(t)$, $\rho^h(t)$ and $q^h(t)$. Generally speaking, plugging this expansion into OBBDG or LDG scheme and setting test functions to be $\Phi_{m,n}$ for $m = 0, 1, \cdots, N-1$ and $n = 0, 1, \cdots, k$ can yield a linear system of ordinary differential equations with unknown vector $\mathbf{c} = (c_{j,l})$:

$$\mathbf{M}\frac{d\mathbf{c}(t)}{dt} = \mathbf{F}(\mathbf{c}, t),$$

where the matrix $\mathbf{M} = (M_{j,l;m,n})$ with

$$M_{j,l;m,n} = \int_0^1 \Phi_{j,l}\Phi_{m,n},$$

is called the mass matrix.

Next, we will discretize the time derivatives in above schemes by using finite differences in time.

In the semidiscrete scheme of OBBDG or LDG method, the equations defining the approximate solution $\sigma^h(t)$ and $\rho^h(t)$ can be rewritten in ODE form

$$\begin{cases} \frac{d}{dt}\sigma^h(t) = S_h(\sigma^h(t), E(t)), \\ \frac{d}{dt}\rho^h(t) = R_h(\rho^h(t), \sigma^h(t), E(t)), \end{cases} \tag{2.31}$$

after inverting the mass matrix [19].

Since DG methods are suited for high order approximation in space [84], we can combine them with high order time discretization such as Runge-Kutta methods. In this thesis, we apply a third order total variation diminishing Runge-Kutta (TVDRK3) method [86].

Suppose at each time level $t^n = n\tau$, we have already approximated $E(t^n)$ by E^n. Let $\sigma^n = \sigma^h(t^n)$, $\rho^n = \rho^h(t^h)$ and $q^n = q^h(t^n)$ for all $n \geq 0$. Then the fully discrete formulation from t^n to t^{n+1} is as follows.

- Set $\sigma^{(0)} = \sigma^n$ and $\rho^{(0)} = \rho^n$.
- Stage 1. Compute $\sigma^{(1)} = \sigma^{(0)} + \tau S_h(\sigma^{(0)}, E^n)$ and $\rho^{(1)} = \rho^{(0)} + \tau R_h(\rho^{(0)}, \sigma^{(0)}, E^n)$.
- Stage 2. Compute $\sigma^{(2)} = \frac{3}{4}\sigma^{(0)} + \frac{1}{4}\sigma^{(1)} + \frac{1}{4}\tau S_h(\sigma^{(1)}, E^n)$ and $\rho^{(2)} = \frac{3}{4}\rho^{(0)} + \frac{1}{4}\rho^{(1)} + \frac{1}{4}\tau R_h(\rho^{(1)}, \sigma^{(1)}, E^n)$.
- Stage 3. Compute $\sigma^{(3)} = \frac{1}{3}\sigma^{(0)} + \frac{2}{3}\sigma^{(2)} + \frac{2}{3}\tau S_h(\sigma^{(2)}, E^n)$ and $\rho^{(3)} = \frac{1}{3}\rho^{(0)} + \frac{2}{3}\rho^{(2)} + \frac{2}{3}\tau R_h(\rho^{(2)}, \sigma^{(2)}, E^n)$.
- Set $\sigma^{n+1} = \sigma^{(3)}$ and $\rho^{n+1} = \rho^{(3)}$.

Note that in LDG method, we need to solve (2.26) before Stage ν by using $\sigma^{(\nu-1)}$ then plug the solution of q^h into S_h.

We will omit this part in the later chapters since the same temporal discrete scheme is used for the other models.

2.2.4 The slope limiter

As mentioned in Chapter 1, a slope limiter is desired to avoid nonphysical solutions. The slope limiter proposed by Krivodonova [46] will be applied in our work. To explain this slope limiter, we firstly assume the numerical solution in the element I_j can be presented by

$$U_j = \sum_{l=0}^{p} c_{j,l} P_l(\xi), \tag{2.32}$$

where P_l is the l-th order Legendre polynomial and $\xi = \frac{z-(j+1/2)h}{h/2}$.

The slope limiter works from the highest order coefficient in (3.37) by reconstructing $c_{j,l}$ with

$$\hat{c}_{j,l} = minmod(c_{j,l}, \alpha_l(c_{j+1,l-1} - c_{j,l-1}), \alpha_l(c_{j,l-1} - c_{j-1,l-1})), \tag{2.33}$$

where the parameter α_l should statisfy

$$\frac{1}{2(2l-1)} \leq \alpha_l \leq 1, \tag{2.34}$$

and the minmod function is defined by

$$minmod(a,b,c) = \begin{cases} s\min\{|a|,|b|,|c|\}, & \text{if } s = sign(a) = sign(b) = sign(c), \\ 0, & \text{otherwise.} \end{cases}$$

In practice, the parameter α_l is set to be 1 to make the numerical solution least diffusive. If $\hat{c}_{j,l} = c_{j,l}$ for all j at some level l, then the slope limiter stops [46]. Note that the lowest order coefficient does not need to be limited because of the orthogonality of Legendre polynomials.

This slope limiter should be applied after each stage in TVDRK3 method. In addition, this slope limiter is also necessary for the auxiliary variable q^h in LDG method.

2.3 Numerical comparisons and application

To make our methods comparable, we choose linear polynomial approximation in DG method and LSFEM method so that they are expected to have second order of accuracy. Assume the number of element in each method is N, then the number of unknowns in one single time step are given in the following table. Suppose the combinatorial algorithm is denoted by A+B where Method A and B are applied to solve Poisson's equation and continuity equation respectively. In the view of efficiency, we only consider four combinations: FDM+LDG, FDM+OBBDG, SIPG+OBBDG and LSFEM+OBBDG.

Continuity equations		Poisson's equation		
OBBDG	LDG	FDM	SIPG	LSFEM
$3 \cdot 2 \cdot 2N$	$3 \cdot 3 \cdot 2N$	N	$2N$	$2N+2$

Table 2.1: Number of unknowns in one single time step for different methods. Note that there are three stages in TVDRK3 method and on each stage we have to solve two (three) equations for the OBBDG method (LDG method) respectively. Additionally, the Poisson's equation is only solved once in one single time step.

The comparisons are carried on a double-headed streamer propagation example with experiment data [97]. The gap length is 1cm and the applied voltage is 52kV. The gas between electrodes are nitrogen at 300K under standard atmospheric pressure $P = 760$ torr. After nondimensionlization, the coefficients in model (2.1) are $\mu_\rho = 0.009$, $D = 9.0716E-5$, $S = 4332$, $K = -3.9315$, and initial data is set to be

$$\sigma(z,0) = \rho(z,0) = 0.0035 + 3.4752 \times 10^3 \times \exp\{-[(z-0.5)/0.027]^2\}.$$

The terminal time is set to be $T = 0.1$ which corresponds to 5ns. To compare the convergence rate in space for each coupled method, the time step is taken to be very small. The 'exact' solutions are numerically defined by using very fine mesh, namely $h = \frac{1}{2048}$, and tiny time step size $\tau = 10^{-5}$. In order to compare the convergence rate in space for each coupled method, the time step is chosen as small enough. The results from Table 2.2 - 2.5 show that if the mesh size is smaller than some threshold, all the four methods are acceptable since the physical quantities can obtain their desired convergence rate in each method. Besides, the errors for particle densities in FDM+LDG method is much less than the other methods. Therefore, this comparison indicates that all the four methods can be used to simulate the 1D streamer propagation and FDM+LDG method is the best one among them.

From the previous comparison, it can be found that all of the four numerical methods are competitive candidates for solving the streamer propagation models in terms of accuracy. If the discharge region has a simple geometry, e.g. the gap

		$h_0 = \frac{1}{64}$	$h_0/2$	$h_0/2^2$	$h_0/2^3$	$h_0/2^4$
FDM	error	0.0135	0.0123	0.0035	4.7084E-4	4.1914E-5
+LDG	rate	-	0.1322	1.7976	2.9115	3.4898
FDM	error	0.0538	0.0293	0.0086	0.0022	4.5700E-4
+OBBDG	rate	-	0.8787	1.7688	1.9855	2.2463
SIPG	error	0.0851	0.0457	0.0134	0.0034	7.0012E-4
+OBBDG	rate	-	0.8986	1.7708	1.9825	2.2739
LSFEM	error	0.0626	0.0347	0.0098	0.0024	4.9211E-4
+OBBDG	rate	-	0.8497	1.8301	2.0254	2.2847

Table 2.2: Error and convergence rate for σ in 1D comparison.

		$h_0 = \frac{1}{64}$	$h_0/2$	$h_0/2^2$	$h_0/2^3$	$h_0/2^4$
FDM	error	0.0137	0.0123	0.0035	4.7227E-4	4.5860E-5
+LDG	rate	-	0.1571	1.7973	2.9076	3.3643
FDM	error	0.0540	0.0293	0.0086	0.0022	4.5739E-4
+OBBDG	rate	-	0.8827	1.7688	1.9853	2.2453
SIPG	error	0.0851	0.0457	0.0134	0.0034	7.0030E-4
+OBBDG	rate	-	0.8987	1.7708	1.9825	2.2736
LSFEM	error	0.0627	0.0347	0.0098	0.0024	4.9212E-4
+OBBDG	rate	-	0.8521	1.8302	2.0254	2.2847

Table 2.3: Error and convergence rate for ρ in 1D comparison.

		$h_0 = \frac{1}{64}$	$h_0/2$	$h_0/2^2$	$h_0/2^3$	$h_0/2^4$
FDM	error	8.4380E-4	5.3150E-5	1.4045E-5	3.3630E-6	6.0467E-7
+LDG	rate	-	3.9887	1.9200	2.0622	2.4756
FDM	error	8.2013E-4	5.8894E-5	9.3893E-6	1.9641E-6	3.7919E-7
+OBBDG	rate	-	3.7996	2.6490	2.2571	2.3729
SIPG	error	2.2345E-4	3.4253E-5	4.9606E-6	1.9926E-6	5.1926E-7
+OBBDG	rate	-	2.7057	2.7876	1.3159	1.9401
LSFEM	error	1.8601E-4	1.3564E-5	3.0023E-6	7.1625E-7	1.4327E-7
+OBBDG	rate	-	3.7775	2.1757	2.0676	2.3217

Table 2.4: Error and convergence rate for ϕ in 1D comparison.

		$h_0 = \frac{1}{64}$	$h_0/2$	$h_0/2^2$	$h_0/2^3$	$h_0/2^4$
SIPG	error	0.0029	8.1787E-4	1.5831E-4	8.8592E-5	3.4534E-5
+OBBDG	rate	-	1.7121	2.4613	0.8375	1.3592
LSFEM	error	0.0116	0.0010	1.0819E-4	1.8186E-5	3.2629E-6
+OBBDG	rate	-	3.5392	3.2113	2.5727	2.4786

Table 2.5: Error and convergence rate for E in 1D comparison.

between two parallel plates, FDM+LDG or FDM+OBBDG will be applied because of its easy implementation. On the other hand, if the geometry is complex, e.g. the point-to-plate gap, one must choose SIPG+OBBDG or LSFEM+OBBDG.

In this Chapter, since we are dealing with 1D model, we choose FDM+LDG to simulate the streamer propagation in a 1cm gap of nitrogen. The mesh size is $\triangle z = \frac{1}{1024}$ and $\triangle t = 2 \times 10^{-5}$.

The dynamics is shown in Figure 2.1. From this figure, we can see that the electron density increases very fast (see the left top one) and the net charge density is significantly less than the electron density (see the left bottom one), which mean that ionization plays a leading role in the discharge process. This is consistent with discharge mechanism. However, particle densities tend to infinity before the particles arrive the boundary which is contrary to the experimental observation. Therefore, 1D model is not suitable to describe the streamer propagation.

2.4 A study of effects of parameters in source terms

Since ionization source term is dominant, we want to study the effects of parameter S and K in this term. To make the effects observable, we consider a milder case:

$$\mu_\sigma = -1,\ \mu_\rho = 0.5,\ D = 10^{-4},$$

and

$$\sigma(z,0) = \rho(z,0) = \exp\{-100(z-0.5)^2\}.$$

We are going to change the values of S or K successively to demonstrate the influence.

We firstly focus on the number densities of particles. Fix $S = 100$ and let K decrease, which means the gap length is fixed but the background electric field is decreased; then from Figure 2.2, we can see that the maximum density of electrons

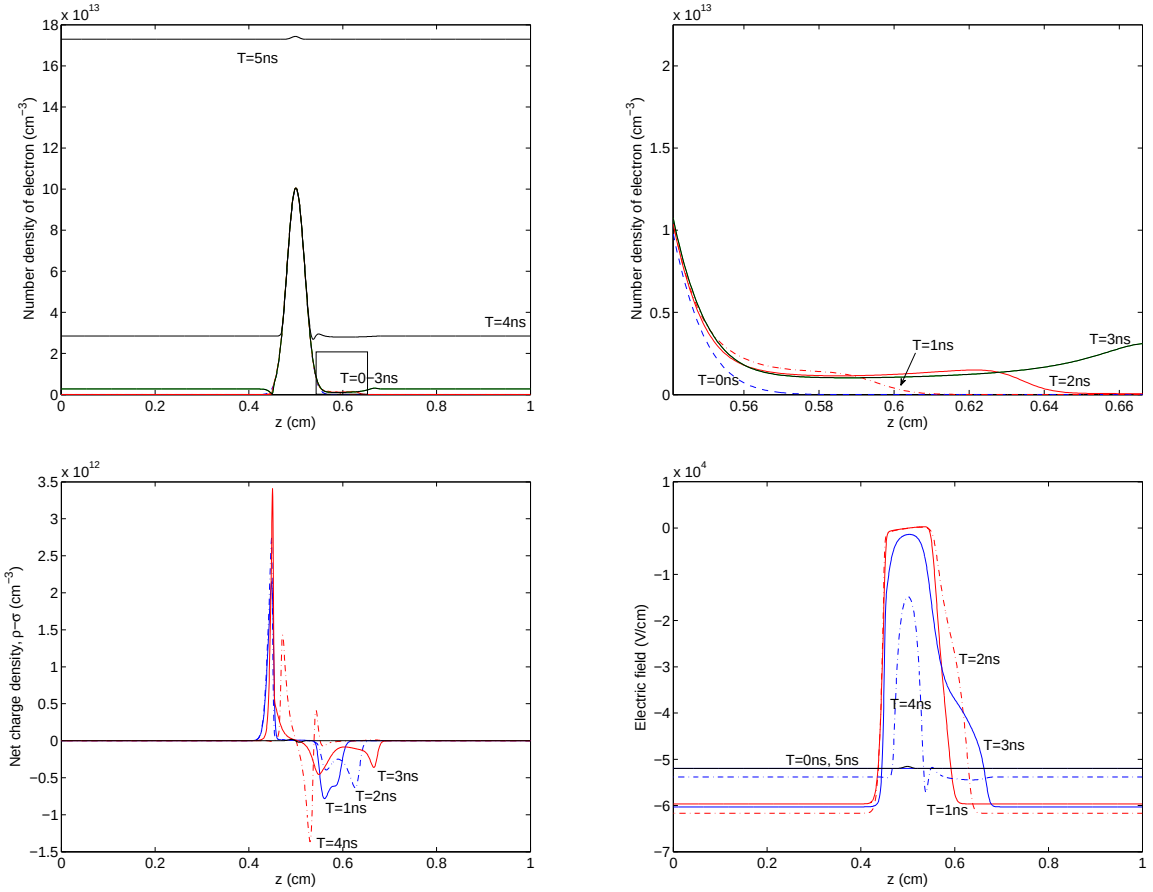

Figure 2.1: The profiles of a double headed streamer propagation in 1D simulation at different time. The left top figure shows the number density of electron, in which the rectangular box is zoomed in and shown in the right top figure. The left bottom figure shows the number density of net charge. The right bottom figure shows the electric field.

or positive ions decreases rapidly and the drift velocity of particles is also decreased. In addition, if the electric field is small enough, positive ions move in the opposite direction with electrons, which means the convection term starts to dominate. If we fix $K = -5$ and increase S, which means the background electric field is kept the same but the gap length is enlarged; we can observe from Figure 2.3 that the maximum density of electrons or positive ions increase slowly and the drift velocity is almost unaffected. This result indicates that background electric field is the essential factor in streamer propagation and long streamer propagation is more stable than short streamer propagation.

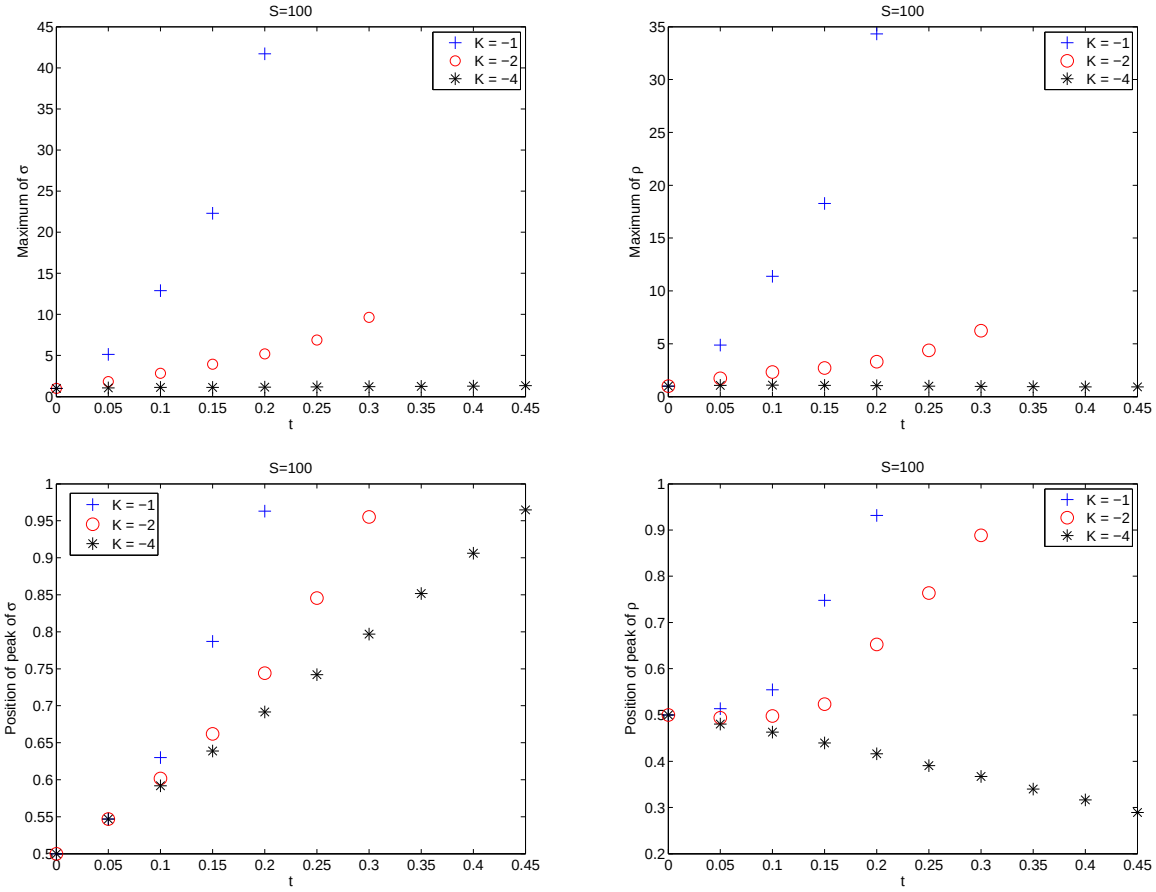

Figure 2.2: Effects of different K on particle densities. The first row shows the maximum number density of electrons and positive ions and the second row shows the maximum points.

Then we simply study the effect of different S and K on electric potential and field in Figure 2.4. It can be concluded that both larger background electric field and shorter gap can speed up and amplify the modification of space electric field. However, the effect on electric potential is not so obvious.

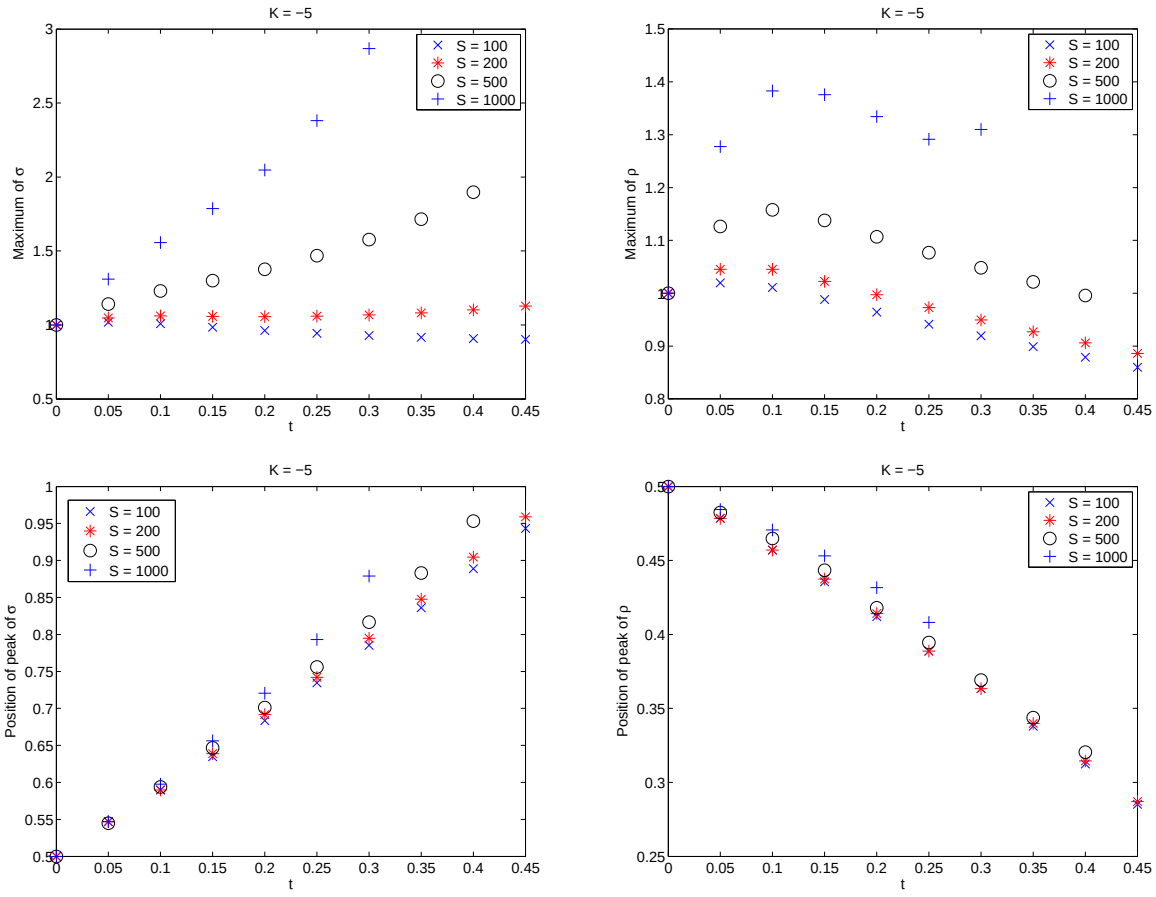

Figure 2.3: Effects of different S on particle densities. The first row shows the maximum number density of electrons and positive ions and the second row shows the maximum points.

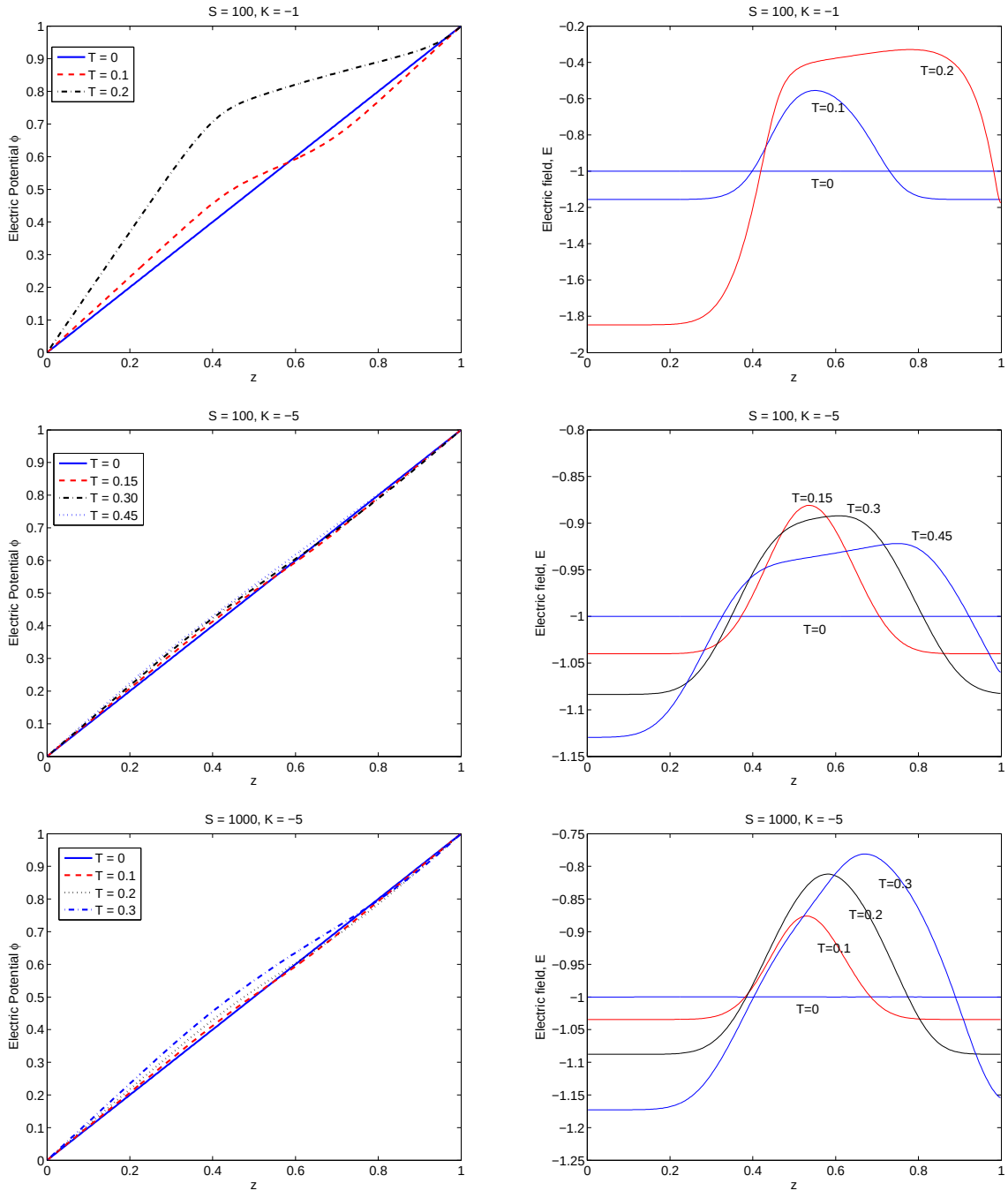

Figure 2.4: Effects of different S and K on electric potential (left column) and field (right column). Since there is no apparent characteristics for electric field and potential, we simply present the profiles at different time.

Chapter 3

Numerical Methods and Results for Quasi 2D Model

In this chapter, we focus on the behavior of the solution in quasi 2D model (1.9),

$$\begin{cases} \frac{\partial \sigma}{\partial t} + \frac{1}{r}\frac{\partial (r\mu_\sigma \sigma E)}{\partial r} - \frac{D}{r}\frac{\partial}{\partial r}\left(r\frac{\partial \sigma}{\partial r}\right) = S|E|e^{K/|E|}\sigma, \\ \frac{\partial \rho}{\partial t} + \frac{1}{r}\frac{\partial (r\mu_\rho \rho E)}{\partial r} = S|E|e^{K/|E|}\sigma, \\ -\frac{1}{r}\frac{\partial}{\partial r}\left(r\frac{\partial \phi}{\partial r}\right) = \rho - \sigma, E = -\frac{\partial \phi}{\partial r}. \end{cases} \tag{3.1}$$

The computational domain can generally be assumed as $\Omega = [r^0, 1]$. The initial condition is posed by

$$\sigma(r, 0) = \sigma_0(r),\ \rho(r, 0) = \rho_0(r),\ r \in \Omega.$$

The boundary conditions for continuity equations are still the homogeneous Neumann type. But the boundary conditions for Poisson's equation are set up distinctively in two different cases. Similar with the previous chapter, the boundary condition at inflow boundary for the equation of ρ is the true boundary condition; the other one is the artificial boundary condition.

Case 1, $r^0 = 0$. In this case, the computational domain before changing of variable is a disc which includes the origin $r = 0$. Thus, the boundary conditions for Poisson's equation are given by the follows. At $r = 0$, we impose Neumann

boundary condition $\frac{\partial \phi}{\partial r} = 0$ to avoid irregularity; and at $r = 1$, a Dirichlet boundary condition is imposed to assure the well-poseness. In fact, there is no truly physical application in such case. In this work, this case is used to test and compare our algorithms and to study the extensions of our method to quasi three-dimensional model [104].

Case 2, $r^0 > 0$. In this case, the former domain is a ring which excludes the origin. So it is possible to impose Dirichlet boundary conditions, $\phi(r^0, t) = 0$ and $\phi(1, t) = 1$ or -1.

Generally speaking, let $r^0 = r_0 < r_1 < \cdots < r_N = 1$ be a uniform spatial partition of computational domain $[r^0, 1]$ such that $r_j = r^0 + jh$ where $h = \frac{1-r^0}{N}$ for $j = 0, 1, \cdots, N$. Denote the subintervals by $I_j = [r_j, r_{j+1}]$, $j = 0, 1, \cdots, N-1$. The definitions of other notations are inherited from Chapter 2.

The main difficulty in quasi 2D model is the factor $\frac{1}{r}$. When r^0 is closed to 0, this factor becomes singular. Suppose there is a function $u(x, y) \equiv u(\sqrt{x^2 + y^2})$ defined on a 2D domain $\Omega = \{(x, y) : R_0^2 < x^2 + y^2 < R_1^2\}$ with central symmtry and the test function is denoted by v. By applying polar coordinate to change the variable, i.e., $r = \sqrt{x^2 + y^2}$, we can obtain

$$\int_\Omega (\triangle u) v dx dy = 2\pi \int_{R_0}^{R_1} \frac{1}{r} \frac{d}{dr} \left(r \frac{du}{dr} \right) v r dr = 2\pi \int_{R_0}^{R_1} \frac{1}{r} \frac{d}{dr} \left(r \frac{du}{dr} \right) \cdot (rv) dr.$$

Therefore, to overcome the singularity caused by $\frac{1}{r}$, new test function rv, where v is the test function in the previous chapter, is applied in Galerkin-type schemes in this chapter. By using integration by part, we can have

$$\int_\Omega (\triangle u) v dx dy = 2\pi \left[r \frac{du}{dr} \Big|_{R_0}^{R_1} - \int_{R_0}^{R_1} r \frac{du}{dr} \frac{dv}{dr} \right].$$

This will help us to establish the numerical schemes. Note that the factor 2π will be canceled during derivation.

3.1 Numerical methods for Poisson's equation

Similar to Chapter 2, finite difference method (FDM) and discontinuous Galerkin (DG) method will be applied to solve Poisson's equation in quasi 2D model. The only difference is that mixed finite element method [14, 15] will replace least-squares finite element method to participate in comparisons.

Similarly, we consider the Poisson's equation in (3.1) to be independent of temporal variable t,

$$-\frac{1}{r}\frac{d}{dr}\left(r\frac{d\phi}{dr}\right) = \rho^n - \sigma^n.$$

3.1.1 The finite difference method

In this method, the numerical solution for electric potential, ϕ_j is defined in the center of element I_j. Let r_j^C be the center of subinterval I_j. We use the standard second order central difference to approximate $-\frac{1}{r}\frac{d}{dr}\left(r\frac{d\phi}{dr}\right)$:

$$\begin{aligned}
& -\frac{1}{r}\frac{d}{dr}\left(r\frac{d\phi}{dr}\right)\Big|_{r=r_j^C} \\
\approx\ & -\frac{1}{r_j^C}\frac{\left(r\frac{d\phi}{dr}\right)_{j+\frac{1}{2}} - \left(r\frac{d\phi}{dr}\right)_{j-\frac{1}{2}}}{h} \\
\approx\ & -\frac{1}{r_j^C}\frac{r_{j+\frac{1}{2}}\frac{\phi_{j+1}-\phi_j}{h} - r_{j-\frac{1}{2}}\frac{\phi_j-\phi_{j-1}}{h}}{h} \\
=\ & -\frac{1}{r_j^C}\frac{\left(r_j^C+\frac{1}{2}h\right)(\phi_{j+1}-\phi_j) - \left(r_j^C-\frac{1}{2}h\right)(\phi_j-\phi_{j-1})}{h^2} \\
=\ & -\frac{\phi_{j+1}-2\phi_j+\phi_{j-1}}{h^2} - \frac{\phi_{j+1}-\phi_{j-1}}{2hr_j^C}.
\end{aligned}$$

Therefore, the FDM reads,

$$-\frac{\phi_{j-1}^n - 2\phi_j^n + \phi_{j+1}^n}{h^2} - \frac{\phi_{j+1}^n - \phi_{j-1}^n}{2hr_j^C} = \rho_j^n - \sigma_j^n, \text{ for } j = 0, 1, \cdots, N-1, \quad (3.2)$$

where ρ_j^n and σ_j^n are the approximate values of ρ and σ in element centers. The boundary conditions are strongly imposed by introducing ghost cells. If the boundary condition is imposed by Dirichlet type, then a linear interpolation will be used.

If the boundary condition is given by Neumann type, then we use reflection. After obtaining the numerical electric potential ϕ, the numerical electric field at each node is defined by

$$E^n|_{r_j} = \frac{\phi^n_{j-1} - \phi^n_j}{h}, \text{ for } j = 0, 1, \cdots, N; \tag{3.3}$$

and the numerical electric field in each element is defined by a constant,

$$E^n|_{I_j} = \frac{\phi^n_{j-1} - \phi^n_{j+1}}{2h}, \text{ for } j = 0, 1, \cdots, N-1. \tag{3.4}$$

3.1.2 The discontinuous Galerkin method

We apply the ideas in [6] to derive the numerical scheme for this method. Firstly, we reformulate the Poisson's equation by a first order system

$$\begin{cases} \frac{1}{r}\frac{d(rE)}{dr} = \rho^n - \sigma^n, \\ -\frac{d\phi}{dr} = E. \end{cases} \tag{3.5}$$

Multiplying the first and second equation by our new test functions rv and rF respectively, integrating over one single subinterval I_j, and using integration by parts, we can obtain

$$\begin{aligned} rEv|_{r_j}^{r_{j+1}} - \textstyle\int_{I_j} rE\frac{dv}{dr} &= \textstyle\int_{I_j}(\rho^n - \sigma^n)rv, \\ \textstyle\int_{I_j} E \cdot rF = -\phi rF|_{r_j}^{r_{j+1}} &+ \textstyle\int_{I_j} \phi\frac{d(rF)}{dr}. \end{aligned}$$

Thus, we consider a general formulation: to find $\phi^h \in V_k$ and $E^h \in V_k$ such that for all subintervals I_j, we have

$$r\hat{E}v\Big|_{r_j}^{r_{j+1}} - \textstyle\int_{I_j} rE^h\frac{dv}{dr} = \textstyle\int_{I_j}(\rho^n - \sigma^n)rv, \ \forall v \in V_k, \tag{3.6}$$

$$\textstyle\int_{I_j} E^h \cdot rF = -\hat{\phi}rF\Big|_{r_j}^{r_{j+1}} + \textstyle\int_{I_j} \phi^h\frac{d(rF)}{dr}, \ \forall F \in V_k, \tag{3.7}$$

where $\hat{E}$ and $\hat{\phi}$ are called numerical fluxes which will be defined properly later. If we add over all subintervals I_j, then we can get

$$\sum_{j=0}^{N-1} r\hat{E}v\Big|_{r_j}^{r_{j+1}} - \sum_{j=0}^{N-1}\int_{I_j} rE^h\frac{dv}{dr} = \int_\Omega(\rho^n - \sigma^n)rv, \ \forall v \in V_k, \tag{3.8}$$

and

$$\int_\Omega E^h \cdot rF = -\sum_{j=0}^{N-1} \hat{\phi} rF\Big|_{r_j}^{r_{j+1}} + \sum_{j=0}^{N-1} \int_{I_j} \phi^h \frac{d(rF)}{dr}, \ \forall F \in V_k. \tag{3.9}$$

By using the definition of jump and average (which are defined in Chapter 2), it is not difficult to prove that

$$\begin{aligned} \sum_{j=0}^{N-1} ra(r)B(r)|_{r_j}^{r_{j+1}} &= \sum_{j=0}^{N} r_j[a(r_j)B(r_j)] \\ &= \sum_{j=1}^{N-1} r_j(\{a(r_j)\}[B(r_j)] + [a(r_j)]\{B(r_j)\}) \\ &\quad + \sum_{j=0,N} r_j\{a(r_j)\}[B(r_j)], \end{aligned} \tag{3.10}$$

for two piecewise continuously differentiable functions $a(r)$ and $B(r)$.

If we set $a = v, B = \hat{E}$ and $a = \hat{\phi}, B = F$ respectively in (3.10), and insert the results into (3.8) and (3.9), then we can find that

$$\begin{aligned} &\sum_{j=1}^{N-1} r_j(\{v(r_j)\}[\hat{E}(r_j)] + [v(r_j)]\{\hat{E}(r_j)\}) + \sum_{j=0,N} r_j\{v(r_j)\}[\hat{E}(r_j)] \\ -\ &\sum_{j=0}^{N-1} \int_{I_j} rE^h \frac{dv}{dr} = \int_\Omega (\rho^n - \sigma^n) rv, \ \forall v \in V_k, \end{aligned} \tag{3.11}$$

and

$$\begin{aligned} &-\sum_{j=1}^{N-1} r_j(\{\hat{\phi}(r_j)\}[F(r_j)] + [\hat{\phi}(r_j)]\{F(r_j)\}) - \sum_{j=0,N} r_j\{\hat{\phi}(r_j)\}[F(r_j)] \\ +\ &\sum_{j=0}^{N-1} \int_{I_j} \phi^h \frac{d(rF)}{dr} = \int_\Omega E^h \cdot rF, \ \forall F \in V_k. \end{aligned} \tag{3.12}$$

Therefore, by setting $a = \phi^h, B = F$ in (3.10), using (3.12) and noticing

$$\sum_{j=0}^{N-1} ra(r)B(r)|_{r_j}^{r_{j+1}} = \sum_{j=0}^{N-1} \int_{I_j} \frac{d(raB)}{dr},$$

we have

$$\begin{aligned}
&\sum_{j=1}^{N-1} r_j(\{\phi^h(r_j)\}[F(r_j)] + [\phi^h(r_j)]\{F(r_j)\}) + \sum_{j=0,N} r_j\{\phi^h(r_j)\}[F(r_j)] \\
= &\sum_{j=0}^{N-1}\int_{I_j}\frac{d(r\phi^h F)}{dr} = \sum_{j=0}^{N-1}\int_{I_j}\left(rF\frac{d\phi^h}{dr} + \phi^h\frac{d(rF)}{dr}\right) \\
= &\sum_{j=0}^{N-1}\int_{I_j}\left(E^h + \frac{d\phi^h}{dr}\right)rF + \sum_{j=1}^{N-1} r_j(\{\hat{\phi}(r_j)\}[F(r_j)] + [\hat{\phi}(r_j)]\{F(r_j)\}) \\
&+ \sum_{j=0,N} r_j\{\hat{\phi}(r_j)\}[F(r_j)],
\end{aligned}$$

or equivalently,

$$\begin{aligned}
\sum_{j=0}^{N-1}\int_{I_j}\left(E + \frac{d\phi^h}{dr}\right)rF \;=\; &\sum_{j=1}^{N-1} r_j(\{\phi^h(r_j) - \hat{\phi}(r_j)\}[F(r_j)] + [\phi^h(r_j) - \hat{\phi}(r_j)]\{F(r_j)\}) \\
&+ \sum_{j=0,N} r_j\{\phi^h(r_j) - \hat{\phi}(r_j)\}[F(r_j)]. \qquad (3.13)
\end{aligned}$$

If we take $F = \frac{dv}{dr}$ in each subinterval in (3.13) and combine the resulting equation with (3.11), we can obtain

$$\begin{aligned}
&\sum_{j=0}^{N-1}\int_{I_j} r\frac{d\phi^h}{dr}\frac{dv}{dr} + \sum_{j=1}^{N-1} r_j(\{v(r_j)\}[\hat{E}(r_j)] + [v(r_j)]\{\hat{E}(r_j)\}) + \sum_{j=0,N} r_j\{v(r_j)\}[\hat{E}(r_j)] \\
- &\sum_{j=1}^{N-1} r_j\left(\{\phi(r_j) - \hat{\phi}(r_j)\}\left[\frac{dv}{dr}(r_j)\right] + [\phi(r_j) - \hat{\phi}(r_j)]\left\{\frac{dv}{dr}(r_j)\right\}\right) \\
- &\sum_{j=0,N} r_j\{\phi(r_j) - \hat{\phi}(r_j)\}\left[\frac{dv}{dr}(r_j)\right] = \int_\Omega(\rho^n - \sigma^n)rv,\ \forall v \in V_k. \qquad (3.14)
\end{aligned}$$

Different choices for the numerical fluxes $\hat{\phi}$ and $\hat{E}$ in (3.14) can lead to different DG methods proposed in literature. In this thesis, the numerical flux $\hat{E}$ is defined by

$$\begin{cases}
\hat{E}(r_j^+) = \hat{E}(r_j^-) = -\left\{\frac{d\phi^h}{dr}(r_j)\right\} + \frac{\alpha}{h^\beta}[\phi^h(r_j)], & \text{if } j = 1, \cdots, N-1, \\
\hat{E}(r_j^\pm) = -\frac{d\phi}{dr}(r_j^\pm, t^n) = 0, & \text{if } r_j \text{ is Neumann node}, \\
\hat{E}(r_j^\pm) = -\frac{d\phi^h}{dr}(r_j^\pm) \mp \frac{\alpha}{h^\beta}(\phi^h(r_j^\pm) - \phi(r_j, t^n)), & \text{if } r_j \text{ is Dirichlet node},
\end{cases} \qquad (3.15)$$

where $\alpha \geq 0$ and $\beta > 0$; and the numerical flux $\hat{\phi}$ is defined by

$$\begin{cases} \hat{\phi}(r_j^{\pm}) = \{\phi^h(r_j)\} \pm c[\phi^h(r_j)], & \text{if } j = 1, \cdots, N-1, \\ \hat{\phi}(r_j^{\pm}) = \phi^h(r_j^{\pm}), & \text{if } r_j \text{ is Neumann node}, \\ \hat{\phi}(r_j^{\pm}) = \phi^h(r_j^{\pm}) - (2c+1)(\phi^h(r_j^{\pm}) - \phi(r_j, t^n)), & \text{if } r_j \text{ is Dirichlet node}, \end{cases} \tag{3.16}$$

for any real number c.

By inserting the numerical fluxes into (3.14) and letting $\epsilon = -(2c+1)$, we can get

$$\begin{aligned} & \sum_{j=0}^{N-1} \int_{I_j} r \frac{d\phi^h}{dr} \frac{dv}{dr} + \sum_{j=1}^{N-1} r_j \left(- \left\{ \frac{d\phi^h}{dr}(r_j) \right\} + \frac{\alpha}{h^\beta} [\phi^h(r_j)] \right) [v(r_j)] \\ + & \sum_{j \in N_d} r_j \left(- \left\{ \frac{d\phi^h}{dr}(r_j) \right\} [v_j] + \frac{\alpha}{h^\beta} (\phi^h(r_j) - \phi(r_j, t^n)) v(r_j) \right) \\ + & \epsilon \sum_{j=1}^{N-1} r_j [\phi^h(r_j)] \left\{ \frac{dv}{dr}(r_j) \right\} + \epsilon \sum_{j \in N_d} r_j \left([\phi^h(r_j)] \left\{ \frac{dv}{dr}(r_j) \right\} - \phi(r_j, t^n) \left[\frac{dv}{dr}(r_j) \right] \right) \\ = & \int_\Omega (\rho^n - \sigma^n) r v, \ \forall v \in V_k. \end{aligned} \tag{3.17}$$

Therefore, if we define the bilinear form $B_\epsilon : V_k \times V_k \to \mathbb{R}$,

$$\begin{aligned} B_\epsilon(u, v) = & \sum_{j=0}^{N-1} \int_{I_j} r \frac{du}{dr} \frac{dv}{dr} - \sum_{j \in N_i \cup N_d} r_j \left\{ \frac{du}{dr}(r_j) \right\} [v(r_j)] \\ & + \epsilon \sum_{j \in N_i \cup N_d} r_j \left\{ \frac{dv}{dr}(r_j) \right\} [u(r_j)] + \sum_{j \in N_i \cup N_d} r_j \frac{\alpha}{h^\beta} [u(r_j)][v(r_j)], \end{aligned} \tag{3.18}$$

and linear form $L : V_k \to \mathbb{R}$,

$$L(v) = \int_\Omega (\rho - \sigma) r v + \sum_{j \in N_d} r_j \left(\epsilon \left[\frac{dv}{dr}(r_j) \right] + \frac{\alpha}{h^\beta} v(r_j) \right) \phi(r_j, t^n), \tag{3.19}$$

then the DG method is to find $\phi^h \in V_k$ such that

$$B_\epsilon(\phi^h, v) = L(v), \ \forall v \in V_k. \tag{3.20}$$

We choose SIPG method ($\epsilon = -1$) in practice and choose $\alpha = 2$ and $\beta = 1$ to ensure optimal convergence.

The electric field is approximated by

$$E^n(r_j) = -\left\{\frac{d\phi^h}{dr}(r_j)\right\} + \frac{\alpha}{h^\beta}[\phi^h(r_j)], \text{ for } j = 1, 2, \cdots, N-1. \tag{3.21}$$

At the boundary, if it is Case 1 on Page 37, we set

$$\begin{aligned} E^n(r_0) &= -\frac{d\phi^h}{dr}(r_0), \\ E^n(r_N) &= -\frac{d\phi^h}{dr}(r_N) + \frac{\alpha}{h^\beta}(\phi^h(r_N) - \phi(1, t^n)); \end{aligned} \tag{3.22}$$

if it is Case 2 on Page 38, then we set

$$\begin{aligned} E^n(r_0) &= -\frac{d\phi^h}{dr}(r_0) + \frac{\alpha}{h^\beta}(\phi(r^0, t^n) - \phi^h(r_0)), \\ E^n(r_N) &= -\frac{d\phi^h}{dr}(r_N) + \frac{\alpha}{h^\beta}(\phi^h(r_N) - \phi(1, t^n)). \end{aligned} \tag{3.23}$$

Remark. Similar with the traditional DG scheme in previous chapter, the jump in both artificial terms (symmetric and penalty terms) is used for numerical solution. Therefore, the artificial terms will still not affect the convergence of numerical solution for fixed values of artificial parameters. Besides, the requirement for optimal convergence is the same as that in traditional DG scheme.

3.1.3 The mixed finite element method

This method also reformulates the Poisson's equation by a first order system [15],

$$\begin{cases} \frac{1}{r}\frac{d(rE)}{dr} = \rho^n - \sigma^n, \\ -\frac{d\phi}{dr} = E, \end{cases} \tag{3.24}$$

then we can treat ϕ and E as independent variables. Usually, we call ϕ the scalar variable and E the flux variable.

Denote the C^0 nodal finite element space by

$$W_k = \{v : v|_{I_j} \in \mathbb{P}_k(I_j), \text{ for } j = 0, 1, \cdots, N-1, \text{ v is continuous in } [r^0, 1]\}.$$

Let $W_k^1 = W_k \cap \{v : v(r^0) = 0\}$ or $W_k^2 = W_k$ be the space for flux variable in Case 1 or Case 2. Due to stability, the space for scalar variable should satisfy the so-called

inf-sup condition [14, 15]. For example if we choose $k = 1$, then the space for scalar variable is identically equal to the piecewise constant finite element space V_0 defined in Chapter 2 for continuity equations. More generally, the finite element space for scalar variable is defined by

$$V = \{v : v = \frac{dw}{dr} \text{ for some } w \in W_k\} = V_{k-1}.$$

By multiplying the equations in (3.24) by the test functions $r\psi$ and rw for $\psi \in V_{k-1}$ and $w \in W_k^i$ respectively, applying integration by parts to the second equation and using the boundary conditions, the weak formulation for MFEM is to find $(E^h, \phi^h) \in W_k^1 \times V_{k-1}$ such that

$$\begin{cases} -\int_\Omega \psi \frac{d(rE^h)}{dr} = -\int_\Omega (\rho - \sigma) r\psi, \ \forall \psi \in V_{k-1}, \\ \int_\Omega rE^h w + \phi(1, t^n)w(1) - \int_\Omega \phi^h \frac{d(rw)}{dr} = 0, \ \forall w \in W_k^1; \end{cases} \tag{3.25}$$

or to find $(E^h, \phi^h) \in W_k^2 \times V_{k-1}$ such that

$$\begin{cases} -\int_\Omega \psi \frac{d(rE^h)}{dr} = -\int_\Omega (\rho^n - \sigma^n) r\psi, \ \forall \psi \in V_{k-1}, \\ \int_\Omega rE^h w + \phi(1, t^n)w(1) - r^0\phi(r^0, t^n)w(r^0) - \int_\Omega \phi^h \frac{d(rw)}{dr} = 0, \ \forall w \in W_k^2. \end{cases} \tag{3.26}$$

Since the flux variable E^h is continuous in this method, the approximate electric field is naturally chosen as $E^n = E^h$.

The reason why we use MFE rather than LSFEM comes from two simple numerical tests. In these two tests, we compare the results from continuous Galerkin method (CG), MFEM and LSFEM with linear polynomial approximation.

Example 1. Consider

$$\begin{cases} \frac{1}{r}\frac{d}{dr}\left(r\frac{d\phi}{dr}\right) = 1, \text{ in } (0, 1) \\ \phi'(0) = 0, \ \phi(1) = 1, \end{cases}$$

whose exact solution is

$$\phi = \frac{3}{4} + \frac{1}{4}r^2.$$

		$h_0 = 1/16$	$h_0/2$	$h_0/2^2$	$h_0/2^3$
CG	error	9.6305E-5	2.4079E-5	6.0190E-6	1.5046E-6
	order	-	1.9998	2.0002	2.0001
MFE	error	0.0045	0.0023	0.0011	5.6381E-4
	order	-	0.9993	0.9998	1.0000
LS	error	9.8487E-5	2.4628E-5	6.1566E-6	1.5390E-6
	order	-	1.9996	2.0001	2.0001

Table 3.1: Error and convergence rate for ϕ in Example 1 of quasi 2D test.

		$h_0 = 1/16$	$h_0/2$	$h_0/2^2$	$h_0/2^3$
CG	error	0.0064	0.0032	0.0016	7.9733E-4
	order	-	0.9984	0.9995	0.9999
MFE	error	7.0705E-18	7.6120E-18	1.4591E-17	1.0693E-17
	order	-	-	-	-
LS	error	1.4365E-5	3.5952E-6	8.9905E-7	2.2478E-7
	order	-	1.9984	1.9996	1.9999

Table 3.2: Error and convergence rate for $E = -\phi'$ in Example 1 of quasi 2D test.

This is an example for Case 1. The comparisons are shown in Tables 3.1 and 3.2.

Example 2. Consider

$$\begin{cases} \frac{1}{r}\frac{d}{dr}\left(r\frac{d\phi}{dr}\right) = 0, \text{ in } (0.05, 1) \\ \phi(0.05) = 0, \ \phi(1) = 1, \end{cases}$$

whose exact solution is

$$\phi = 1 - \frac{\ln r}{\ln 0.05}.$$

This is an example for Case 2. The comparisons are shown in Tables 3.3 and 3.4.

		$h_0 = 1/16$	$h_0/2$	$h_0/2^2$	$h_0/2^3$
CG	error	0.0032	8.8972E-4	2.3011E-4	5.8079E-5
	order	-	1.8555	1.9510	1.9862
MFE	error	0.0143	0.0057	0.0026	0.0013
	order	-	1.3264	1.1446	1.0442
LS	error	0.0132	0.0047	0.0013	3.4884E-4
	order	-	1.4942	1.8046	1.9426

Table 3.3: Error and convergence rate for ϕ in Example 2 of quasi 2D test.

Tables 3.1 - 3.4 suggest that MFEM is the best method for both of Example 1 and Example 2 if we want an accurate $E = -\frac{d\phi}{dr}$. Although LSFEM has the same order of accuracy for E as MFE, it requires a finer partition.

3.2 Numerical methods for continuity equations

The same numerical methods as in Chapter 2 will be applied in this model.

		$h_0 = 1/16$	$h_0/2$	$h_0/2^2$	$h_0/2^3$
CG	error	0.0746	0.0394	0.0201	0.0101
	order	-	0.9216	0.9737	0.9926
MFE	error	0.0158	0.0043	0.0011	2.7835E-4
	order	-	1.8729	1.9624	1.9900
LS	error	0.0542	0.0195	0.0056	0.0014
	order	-	1.4757	1.8122	1.9475

Table 3.4: Error and convergence rate for $E = -\phi'$ in Example 2 of quasi 2D test.

3.2.1 The Oden-Babuška-Baumann DG method

In this method, firstly, the diffusion term $-\frac{D}{r}\frac{\partial}{\partial r}\left(r\frac{\partial \sigma}{\partial r}\right)$ will be discretized by the bilinear form (3.18) with symmetric parameter $\epsilon = 1$ and penalty parameter $\alpha = 0$. Because of the homogeneous Neumann boundary condition, we only consider interior nodes:

$$\begin{aligned} B(u,v) &= \sum_{j=0}^{N-1}\int_{I_j} rD\frac{du}{dz}\frac{dv}{dz} - \sum_{j\in N_i} r_j\left\{D\frac{du}{dr}(r_j)\right\}[v(r_j)] \\ &+ \sum_{j\in N_i} r_j\left\{D\frac{dv}{dr}(r_j)\right\}[u(r_j)]. \end{aligned} \tag{3.27}$$

Secondly, the convection terms $\frac{1}{r}\frac{\partial(r\mu_P PE)}{\partial r}$ for $P = \sigma$ or ρ will be discretized by

$$\begin{aligned} C(P,v;E) &= -\sum_{j=0}^{N-1}\int_{I_j} rP\mu_P E\frac{dv}{dr} + \sum_{j\in N_i} r_j\widehat{P}(r_j)\mu_P E(r_j)[v(r_j)] \\ &+ \sum_{n\in N_n} r_j[P(r_j)\mu_P E(r_j)v(r_j)], \end{aligned} \tag{3.28}$$

where the numerical flux is defined by

$$\widehat{P}(r) = \begin{cases} P(r^-), & \text{if } \mu_P E(r) \geq 0, \\ P(r^+), & \text{if } \mu_P E(r) < 0. \end{cases}$$

Finally, the source term $S|E|e^{K/|E|}\sigma$ is discretized by a linear form

$$L(\sigma, v; E) = \int_\Omega S|E|e^{K/|E|}\sigma rv. \tag{3.29}$$

Thus, the OBBDG method is to find $\sigma^h(t), \rho^h(t) \in V_k$ such that,

$$\int_\Omega (\sigma^h(0) - \sigma_0(r))rv = \int_\Omega (\rho^h(0) - \rho_0(r))rv = 0,\ \forall v \in V_k; \tag{3.30}$$

and

$$\begin{aligned} &\int_\Omega \frac{\partial \sigma^h}{\partial t} rv + C(\sigma^h(t), v; E(t)) + B(\sigma^h(t), v) = L(\sigma^h(t), v; E(t)),\ \forall v \in V_k, \\ &\int_\Omega \frac{\partial \rho^h}{\partial t} rv + C(\rho^h(t), v; E(t)) = L(\sigma^h(t), v; E(t)),\ \forall v \in V_k, \end{aligned} \tag{3.31}$$

for all $t > 0$.

3.2.2 The local discontinuous Galerkin method

Defining an auxiliary variable

$$q = \frac{\partial \sigma}{\partial r},$$

then the continuity equations become

$$\begin{cases} \frac{\partial \sigma}{\partial t} + \frac{1}{r}\frac{\partial [r(\mu_\sigma \sigma E - Dq)]}{\partial r} = S|E|e^{K/|E|}\sigma, \\ \frac{\partial \rho}{\partial t} + \frac{1}{r}\frac{\partial (r\mu_\rho \rho E)}{\partial r} = S|E|e^{K/|E|}\sigma, \\ q = \frac{\partial \sigma}{\partial r}. \end{cases} \tag{3.32}$$

Multiplying each equation by our new test functions rv, integrating over subinterval I_j and using integration by parts, we can obtain

$$\int_{I_j} qrv = [\sigma rv]|_{r_j}^{r_{j+1}} - \int_{I_j} \sigma \frac{d(rv)}{dr},$$

$$\int_{I_j} \frac{\partial \sigma}{\partial t} rv + [r(\mu_\sigma \sigma E - Dq)v]|_{r_j}^{r_{j+1}} - \int_{I_j} r(\mu_\sigma \sigma E - Dq)\frac{dv}{dr} = \int_{I_j} S|E|e^{K/|E|}\sigma rv,$$

and

$$\int_{I_j} \frac{\partial \rho}{\partial t} rv + [r\mu_\rho \rho E v]|_{r_j}^{r_{j+1}} - \int_{I_j} r\mu_\rho \rho E \frac{dv}{dr} = \int_{I_j} S|E|e^{K/|E|}\sigma rv.$$

We shall replace the boundary terms by some proper fluxes to get

$$\int_{I_j} qrv = [\hat{\sigma} rv]|_{r_j}^{r_{j+1}} - \int_{I_j} \sigma \frac{d(rv)}{dr},$$

$$\int_{I_j} \frac{\partial \sigma}{\partial t} rv + [r(\mu_\sigma \tilde{\sigma} E - D\hat{q})v]|_{r_j}^{r_{j+1}} - \int_{I_j} r(\mu_\sigma \sigma E - Dq)\frac{dv}{dr} = \int_{I_j} S|E| e^{K/|E|} \sigma r v,$$

and

$$\int_{I_j} \frac{\partial \rho}{\partial t} rv + [r\mu_\rho \tilde{\rho} E v]|_{r_j}^{r_{j+1}} - \int_{I_j} r\mu_\rho \rho E \frac{dv}{dr} = \int_{I_j} S|E| e^{K/|E|} \sigma r v.$$

The weak formulation is obtained by adding over all subintervals, using the definition of jump,

$$\int_\Omega qrv = \sum_{j=0}^{N} r_j \hat{\sigma}(r_j)[v(r_j)] - \sum_{j=0}^{N-1} \int_{I_j} \sigma \frac{d(rv)}{dr},$$

$$\begin{aligned} \int_\Omega \frac{\partial \sigma}{\partial t} rv \quad &+ \quad \sum_{j=0}^{N} r_j (\mu_\sigma \tilde{\sigma}(r_j) E(r_j) - D\hat{q}(r_j))[v(r_j)] - \sum_{j=0}^{N-1} \int_{I_j} r(\mu_\sigma \sigma E - Dq)\frac{dv}{dr} \\ &= \quad \int_\Omega S|E| e^{K/|E|} \sigma r v, \end{aligned}$$

and

$$\int_\Omega \frac{\partial \rho}{\partial t} rv + \sum_{j=0}^{N} r_j \mu_\rho \tilde{\rho}(r_j) E(r_j)[v(r_j)] - \sum_{j=0}^{N-1} \int_{I_j} r\mu_\rho \rho E \frac{dv}{dr} = \int_\Omega S|E| e^{K/|E|} \sigma r v,$$

for all test functions v.

In the discretization level, the LDG method is to find $\sigma^h(t), \rho^h(t), q^h(t) \in V_k$ such that

$$\int_\Omega (\sigma^h(0) - \sigma_0(r)) rv = \int_\Omega (\rho^h(0) - \rho_0(r)) rv = 0, \ \forall v \in V_k; \tag{3.33}$$

and

$$\int_\Omega q^h(t) rv = \sum_{j=0}^{N} r_j \widehat{\sigma^h}(r_j)[v(r_j)] - \sum_{j=0}^{N-1} \int_{I_j} \sigma^h(t) \frac{d(rv)}{dr}, \ \forall v \in V_k, \tag{3.34}$$

$$\begin{aligned} \int_\Omega \frac{\partial \sigma^h}{\partial t} rv \quad &+ \quad \sum_{j=0}^{N} r_j \big(\mu_\sigma E(r_j) \widetilde{\sigma^h}(r_j) - D\widehat{q^h}(r_j)\big)[v(r_j)] \\ &- \quad \sum_{j=0}^{N-1} \int_{I_j} r(\sigma^h(t)\mu_\sigma E(t) - Dq^h(t))\frac{dv}{dr} \\ &= \quad L(\sigma^h(t), v; E(t)), \ \forall v \in V_k, \end{aligned} \tag{3.35}$$

$$\begin{aligned}\int_\Omega \frac{\partial \rho^h}{\partial t} rv &+ \sum_{j=0}^{N} r_j\big(\mu_\rho E(r_j)\widetilde{\rho^h}(r_j)\big)[v(r_j)] - \sum_{j=0}^{N-1}\int_{I_j} r\rho^h \mu_\rho E^n \frac{dv}{dr} \\ &= L(\sigma^h(t), v; E(t)),\ \forall v \in V_k, \end{aligned} \tag{3.36}$$

for all $t > 0$, where the linear form L has the same definition as (3.29). And the definition of numerical fluxes is the same as that in Section 2.2.2:

$$\widetilde{P^h}(r) = \begin{cases} P^h(r^-), & \text{if } \mu_P E(r) \geq 0, \\ P^h(r^+), & \text{if } \mu_P E(r) < 0, \end{cases}$$

for $P = \sigma$ or ρ is the convective flux;

$$\widehat{\sigma^h}(r) = \sigma^h(r^+),\ \widehat{q^h}(r) = q^h(r^-),$$

or

$$\widehat{\sigma^h}(r) = \sigma^h(r^-),\ \widehat{q^h}(r) = q^h(r^+),$$

is the diffusive flux.

Remark. Because the boundary conditions for the equation of σ are

$$\frac{\partial \sigma}{\partial r}(r^0, t) = \frac{\partial \sigma}{\partial r}(1, t) = 0,$$

the boundary conditions for the auxiliary equation $q = \frac{\partial \sigma}{\partial r}$ should be

$$q(r^0, t) = q(1, t) = 0.$$

However, this auxiliary equation is a first order equation. Thus, we only use one boundary condition according to the choice of $\widehat{q^h}$.

3.2.3 The slope limiter

It is expected that the cell average of numerical solution would not be changed by the slope limiter [19]. Due to the orthogonality of Legendre polynomials, the cell average is automatically preserved in 1D model. However, since the test function in the quasi 2D model is rv instead of v, the cell average is computed by a weight r

in the integration. Thus, compared with the slope limiter in 1D model, there is one more step in the slope limiter for quasi 2D model: to limit the lowest order coefficient to preserve the cell average. More precisely, suppose the numerical solution in the element I_j is still presented by

$$U_j = \sum_{l=0}^{p} c_{j,l} P_l(\xi), \tag{3.37}$$

where P_l is the l-th order Legendre polynomial and $\xi = \frac{r-(j+1/2)h}{h/2}$. After reconstructing the coefficients $\{c_{j,l}\}$ for $j = 0, 1, \cdots, N-1$ and $l = 1, 2, \cdots, p$, we reconstruct $c_{j,0}$ by

$$\int_{I_j} \sum_{l=0}^{p} \hat{c}_{j,l} P_l(\xi) r dr = \int_{I_j} \sum_{l=0}^{p} c_{j,l} P_l(\xi) r dr. \tag{3.38}$$

3.3 Numerical comparisons and applications

In the view of efficiency, by regarding Table 2.1 again, we only consider four combinations: FDM+LDG, FDM+OBBDG, SIPG+OBBDG and MFEM+OBBDG as well.

Accuracy test 1. $r^0 = 0$.

Under this configuration, the initial data for continuity equations is well separated to avoid constant initial solution to Poisson's equation; otherwise, the solutions of continuity equations remain the same as initial data. Therefore, there is no real experiment to satisfy this requirement. Only accuracy test for different methods is shown. Note that, this test is used to compare different strategies and study the extensions to quasi three-dimensional model [104].

The dimensionless parameters are set by [97],

$$\mu_\sigma = -2,\ \mu_\rho = -1,\ D = 10^{-4},\ S = 1000,\ K = -5;$$

the initial data is

$$\sigma(r, 0) = \exp\{-100r^2\},\ \rho(r, 0) = \exp\{-100(r-1)^2\};$$

and the Dirichlet boundary condition at the right endpoint is

$$\phi(1,t) = 0.$$

The terminal time is $T = 0.5$. The 'exact' solutions are numerically defined by using very fine mesh, namely $h = \frac{1}{1024}$, and tiny time step size $\tau = 10^{-5}$. In order to compare the convergence rate in space for each coupled method, the time step is chosen as small enough. The comparisons from Tables 3.5 - 3.8 indicate that if the mesh size is small enough, all the four methods are acceptable since all the physical quantities can obtain their desired convergence rate in each method. Hence, all the four methods can be used to simulate the quasi 2D streamer propagation when the computational domain contains the origin. In addition, none of them is particularly prominent.

		$h_0 = \frac{1}{32}$	$h_0/2$	$h_0/2^2$	$h_0/2^3$	$h_0/2^4$
FDM	error	0.0010	2.7767E-4	8.2409E-5	2.4836E-5	6.5115E-6
+LDG	rate	-	1.9098	1.7525	1.7304	1.9314
FDM	error	9.5691E-4	2.0306E-4	5.0001E-5	1.2706E-5	2.9361E-6
+OBBDG	rate	-	2.2365	2.0219	1.9764	2.1136
SIPG	error	9.2227E-4	1.8626E-4	4.5483E-5	1.1488E-5	2.7061E-6
+OBBDG	rate	-	2.3079	2.0339	1.9852	2.0859
MFEM	error	9.2247E-4	1.8617E-4	4.4937E-5	1.1317E-5	2.6420E-6
+OBBDG	rate	-	2.3089	2.0506	1.9895	2.0987

Table 3.5: Error and convergence rate for σ in Accuracy test 1 of quasi 2D comparison.

Accuracy test 2 and application. $r^0 > 0$

The numerical comparisons are carried out for a streamer propagation between coaxial circles which have been used in [85] for semiconductor mateiral. In the

		$h_0 = \frac{1}{32}$	$h_0/2$	$h_0/2^2$	$h_0/2^3$	$h_0/2^4$
FDM	error	0.0182	0.0049	0.0014	3.5623E-4	8.0545E-5
+LDG	rate	-	1.8878	1.8092	1.9764	2.1449
FDM	error	0.0182	0.0049	0.0014	3.5623E-4	8.0545E-5
+OBBDG	rate	-	1.8877	1.8093	1.9764	2.1449
SIPG	error	0.0185	0.0049	0.0014	3.4212E-4	7.8791E-5
+OBBDG	rate	-	1.9302	1.8151	2.0137	2.1184
MFEM	error	0.0174	0.0048	0.0013	3.3525E-4	7.6774E-5
+OBBDG	rate	-	1.8663	1.8267	2.0078	2.1266

Table 3.6: Error and convergence rate for ρ in Accuracy test 1 of quasi 2D comparison.

		$h_0 = \frac{1}{32}$	$h_0/2$	$h_0/2^2$	$h_0/2^3$	$h_0/2^4$
FDM	error	1.4470E-4	4.5521E-5	1.2672E-5	3.3403E-6	8.6001E-7
+LDG	rate	-	1.6684	1.8449	1.9236	1.9576
FDM	error	1.4469E-4	4.5524E-5	1.2672E-5	3.3403E-6	8.6001E-7
+OBBDG	rate	-	1.6683	1.8449	1.9236	1.9576
SIPG	error	0.0130	0.0029	7.0998E-4	1.7816E-4	4.0111E-5
+OBBDG	rate	-	2.1495	2.0500	1.9946	2.1511
MFEM	error	0.0347	0.0171	0.0085	0.0041	0.0018
+OBBDG	rate	-	1.0223	1.0138	1.0362	1.1611

Table 3.7: Error and convergence rate for ϕ in Accuracy test 1 of quasi 2D comparison.

		$h_0 = \frac{1}{32}$	$h_0/2$	$h_0/2^2$	$h_0/2^3$	$h_0/2^4$
SIPG	error	0.0551	0.0225	0.0092	0.0039	0.0016
+OBB	rate	-	1.2934	1.2861	1.2309	1.2898
MFEM	error	0.0057	0.0015	3.7874E-4	9.1864E-5	1.9365E-5
+OBBDG	rate	-	1.9133	1.9929	2.0437	2.2461

Table 3.8: Error and convergence rate for E in Accuracy test 1 of quasi 2D comparison.

experiment, the material is a solid, but here we consider the discharge be in nitrogen. The radius of outer circle is 1 cm and the radius of inner circle is 1 mm. A high negative voltage, -6.6 kV is applied to the wire to generate discharge. Thus, the boundary conditions for Poisson's equation are imposed by,

$$\phi(0.1, t) = -1, \ \phi(1, t) = 0.$$

The other dimensionless parameters are from [97] and

$$D_r = 2190 \, \frac{\text{cm}^2}{\text{s}}.$$

The initial data is concentrated around the inner circle,

$$N_e(r, 0) = N_p(r, 0) = 10^8 + 10^{14} \exp\{-[(r - 0.1)/0.021]^2\} \ \text{cm}^{-3}.$$

The terminal time is $T = 0.1$ which is corresponding to 10 ns. The 'exact' solutions are numerically defined by using very fine mesh, namely $h = \frac{1}{2048}$, and tiny time step size $\tau = 10^{-5}$. In order to compare the convergence rate in space for each coupled method, the time step is chosen as small enough. The comparisons from Tables 3.9 - 3.12 indicate that σ, ϕ and E can obtain their desired convergence rate in all of the four methods if the mesh size is small enough. However, from Table 3.10, FDM+LDG and FDM+OBBDG is suboptimal for ρ. This result indicates that FDM is not very suitable in simulating the quasi 2D streamer propagation.

Therefore, we recommend that SIPG+OBBDG is the best method for quasi 2D model. In addition, in this case, the mesh size should be smaller than that in previous test.

		$h_0 = \frac{1}{64}$	$h_0/2$	$h_0/2^2$	$h_0/2^3$	$h_0/2^4$
FDM	error	0.0047	0.0011	2.6046E-4	6.0794E-5	1.2759E-5
+LDG	rate	-	2.0452	2.1217	2.0991	2.2524
FDM	error	0.0047	0.0013	2.5982E-4	5.5842E-5	1.7109E-5
+OBBDG	rate	-	1.8396	2.3270	2.2181	1.7066
SIPG	error	0.0048	0.0012	2.9612E-4	7.4108E-5	1.8088E-5
+OBBDG	rate	-	1.9757	2.0412	1.9985	2.0346
MFEM	error	0.0047	0.0013	2.6153E-4	5.5835E-5	1.7103E-5
+OBBDG	rate	-	1.8569	2.3248	2.2277	1.7069

Table 3.9: Error and convergence rate for σ in Accuracy test 2 of quasi 2D comparison.

From the previous comparisons, we pick up SIPG+OBBDG to simulate the streamer propagation between coaxial circles. The mesh size is $\triangle r = \frac{0.9}{1024}$ and $\triangle t = 1 \times 10^{-5}$. The dynamics are shown in Figure 3.1. From this figure, we can observe that the net charge density is significantly less than electron density by two orders which again proves the ionization source is dominant. From the right top figure, the gap is filled with negatively charged particles which form a negative streamer moving towards the right anode because the electric field is negative (see the right bottom one). From the dynamics of electric potential and field, we can see that there is an obvious difference in the trend between $T = 0$ and $T > 0$.

		$h_0 = \frac{1}{64}$	$h_0/2$	$h_0/2^2$	$h_0/2^3$	$h_0/2^4$
FDM	error	0.0045	0.0012	3.8231E-4	1.5344E-4	5.7398E-5
+LDG	rate	-	1.9324	1.6327	1.3171	1.4186
FDM	error	0.0045	0.0012	3.7991E-4	1.5315E-4	5.8506E-5
+OBBDG	rate	-	1.9388	1.6349	1.3107	1.3883
SIPG	error	0.0047	0.0012	3.0958E-4	8.3709E-5	2.1456E-5
+OBBDG	rate	-	1.9590	1.9773	1.8869	1.9640
MFEM	error	0.0045	0.0010	2.2878E-4	5.2578E-5	1.6734E-5
+OBBDG	rate	-	2.1088	2.1889	2.1214	1.6516

Table 3.10: Error and convergence rate for ρ in Accuracy test 2 of quasi 2D comparison.

		$h_0 = \frac{1}{64}$	$h_0/2$	$h_0/2^2$	$h_0/2^3$	$h_0/2^4$
FDM	error	0.0221	0.0067	0.0012	9.6402E-5	1.9800E-5
+LDG	rate	-	1.7219	2.5164	3.5993	2.2836
FDM	error	0.0236	0.0068	0.0013	1.3337E-4	2.7401E-5
+OBBDG	rate	-	1.8050	2.4268	3.2377	2.2831
SIPG	error	0.0134	0.0039	8.7572E-4	1.4746E-5	2.5383E-5
+OBBDG	rate	-	1.7614	2.1721	2.5701	2.5384
MFEM	error	0.0100	0.0035	0.0013	5.4734E-4	2.4045E-4
+OBBDG	rate	-	1.5293	1.4667	1.2006	1.1867

Table 3.11: Error and convergence rate for ϕ in Accuracy test 2 of quasi 2D comparison.

		$h_0 = \frac{1}{64}$	$h_0/2$	$h_0/2^2$	$h_0/2^3$	$h_0/2^4$
SIPG	error	0.0498	0.0166	0.0042	0.0010	3.8263E-4
+OBBDG	rate	-	1.5875	1.9940	1.9895	1.4536
MFEM	error	0.0341	0.0112	0.0027	5.2027E-4	1.0154E-4
+OBBDG	rate	-	1.6056	2.0431	2.3865	2.3573

Table 3.12: Error and convergence rate for E in Accuracy test 2 of quasi 2D comparison.

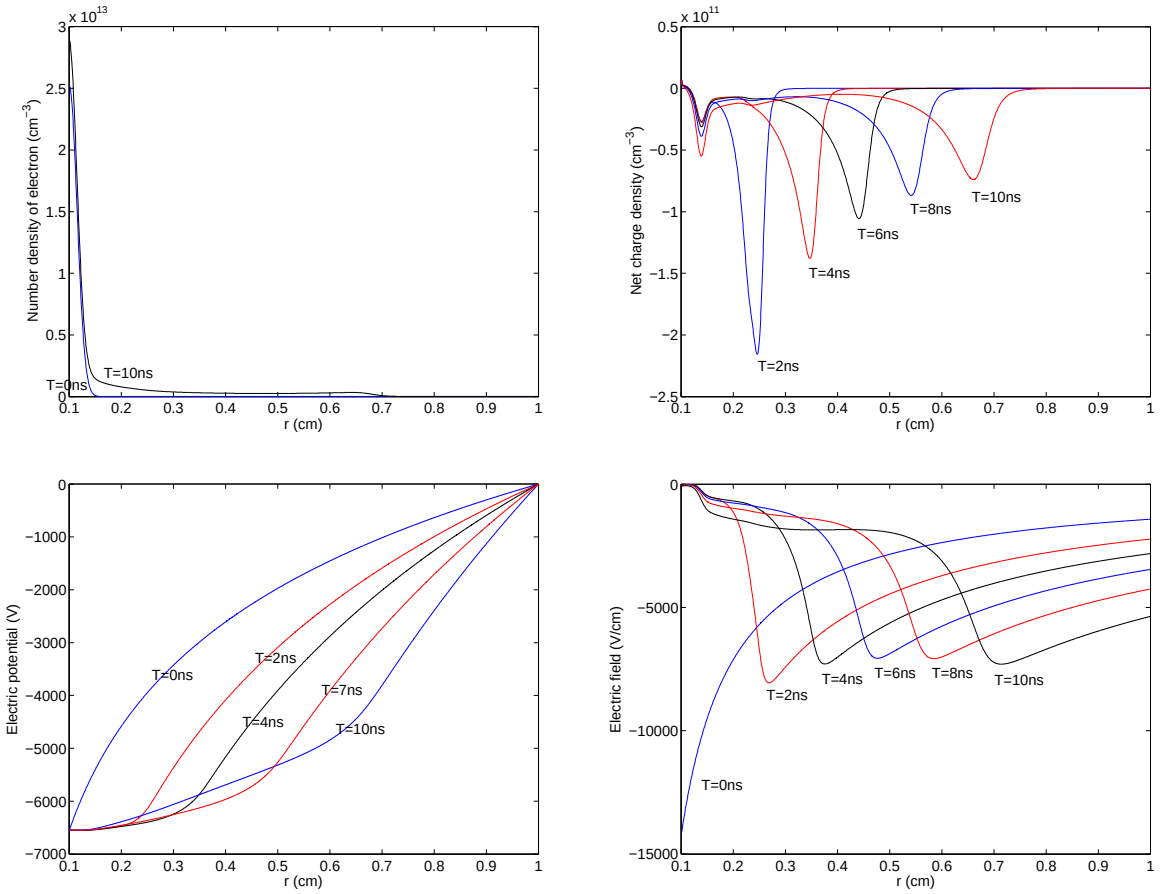

Figure 3.1: The dynamics results of a quasi 2D simulation for streamer propagation between coaxial circles at different time. The left top figure shows the number density of electron and the right top figure shows the number density of net charge. The bottom figures show the electric potential and field.

3.4 A study of effects of parameters in source terms

Similar to Chapter 2, we want to study the effects of parameters S and K in the ionization source term. To make the effects observable, we consider a milder case:

$$\mu_\sigma = -1,\ \mu_\rho = 0.5,\ D = 10^{-4},$$

and

$$\sigma(r,0) = \rho(r,0) = \exp\{-100(r-0.1)^2\}.$$

Figure 3.2 shows effects of different S or K on maximum particle densities. It can be seen that the maximum particle densities increase rapidly when K becomes larger but slowly when S increases. This coincides the conclusion in Chapter 2.

Figure 3.3 shows effects of different S or K on the maximum and maximum points of net charge density. It is indicated that both larger K and larger S can amplify the maximum of net charge density and speed up the propagation of the negative streamer.

Figure 3.4 shows the effects of different S or K on the electric potential and field. It can be concluded again that both larger background electric field and shorter gap can speed up and amplify the modification of space electric field.

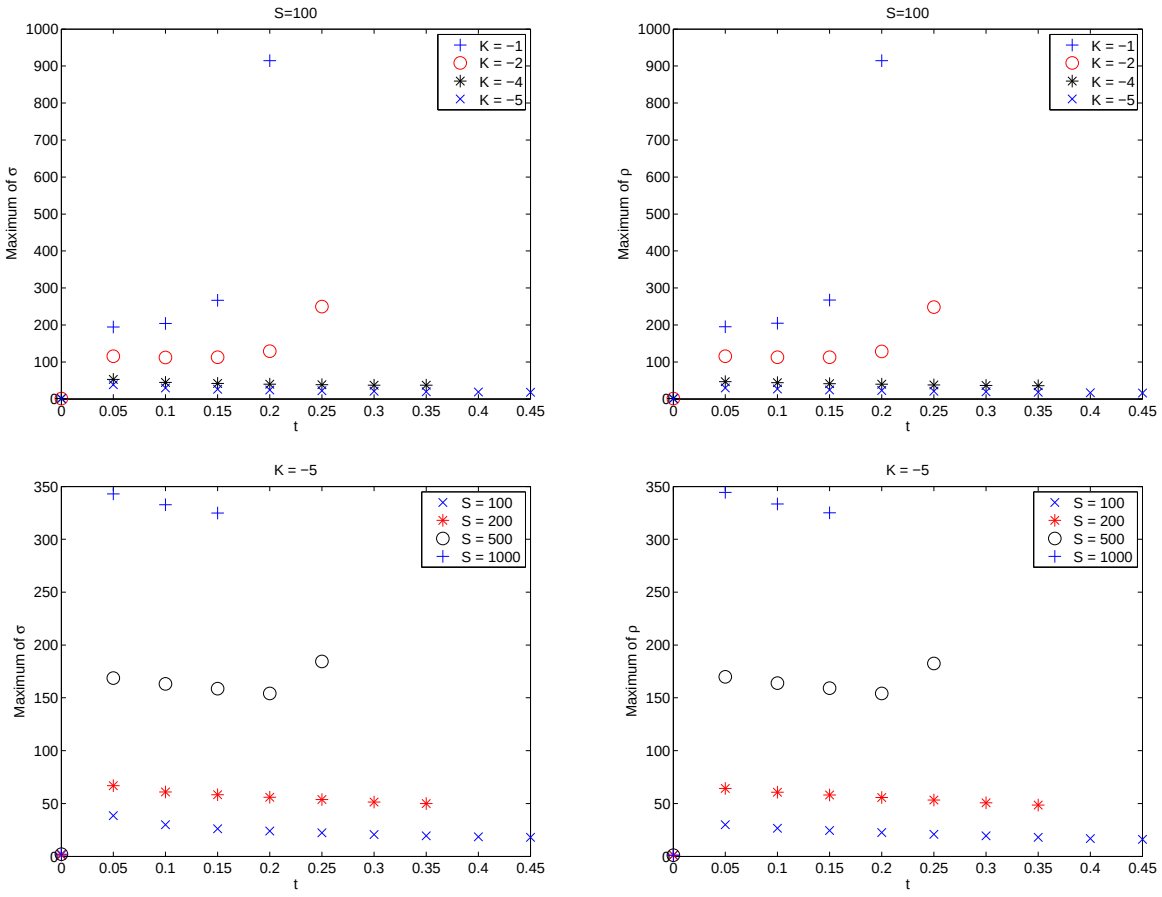

Figure 3.2: Effects of different S or K on maximum particle densities. The first row shows the situations of number density of electron or positive ion when S is fixed. The second row shows the same situations when K is fixed.

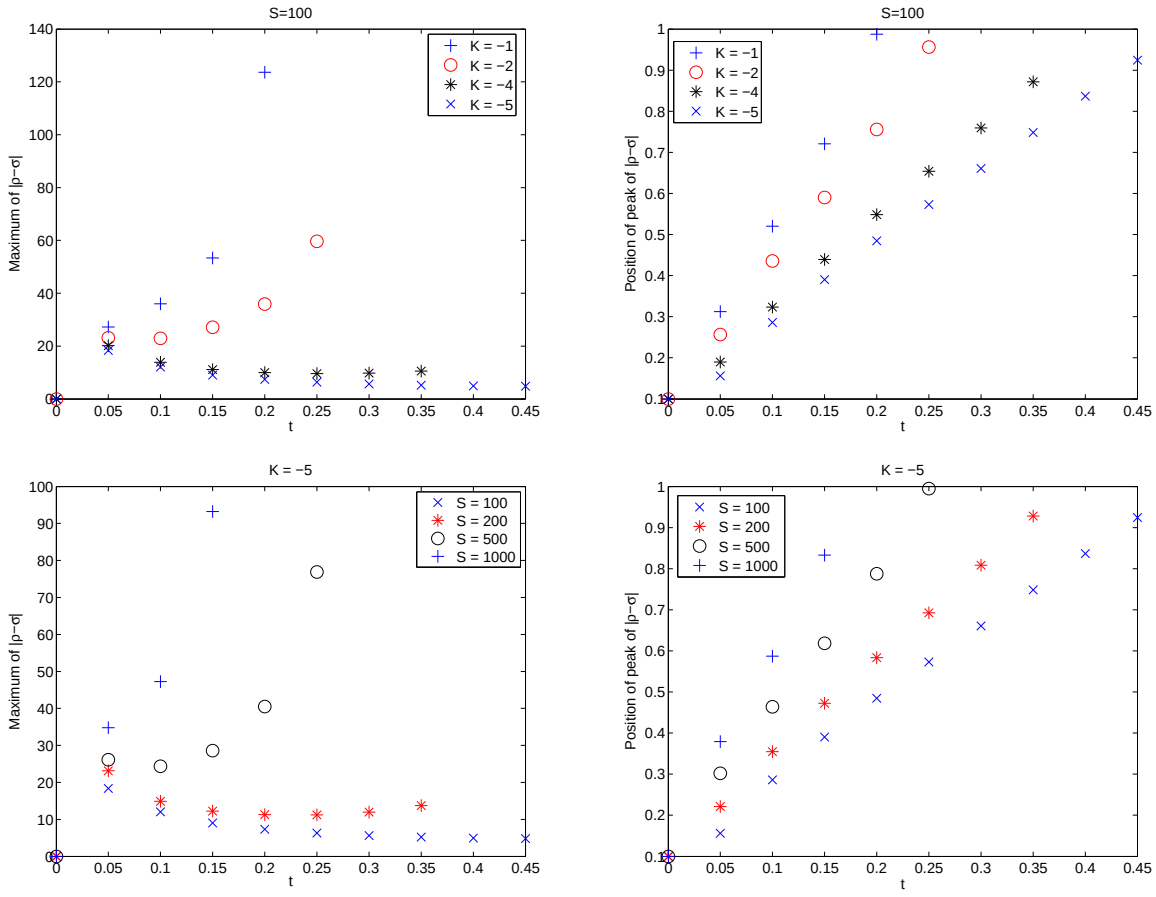

Figure 3.3: Effects of different S or K on net charge density. The first row shows the situations of number density of electron or positive ion when S is fixed. The second row shows the same situations when K is fixed.

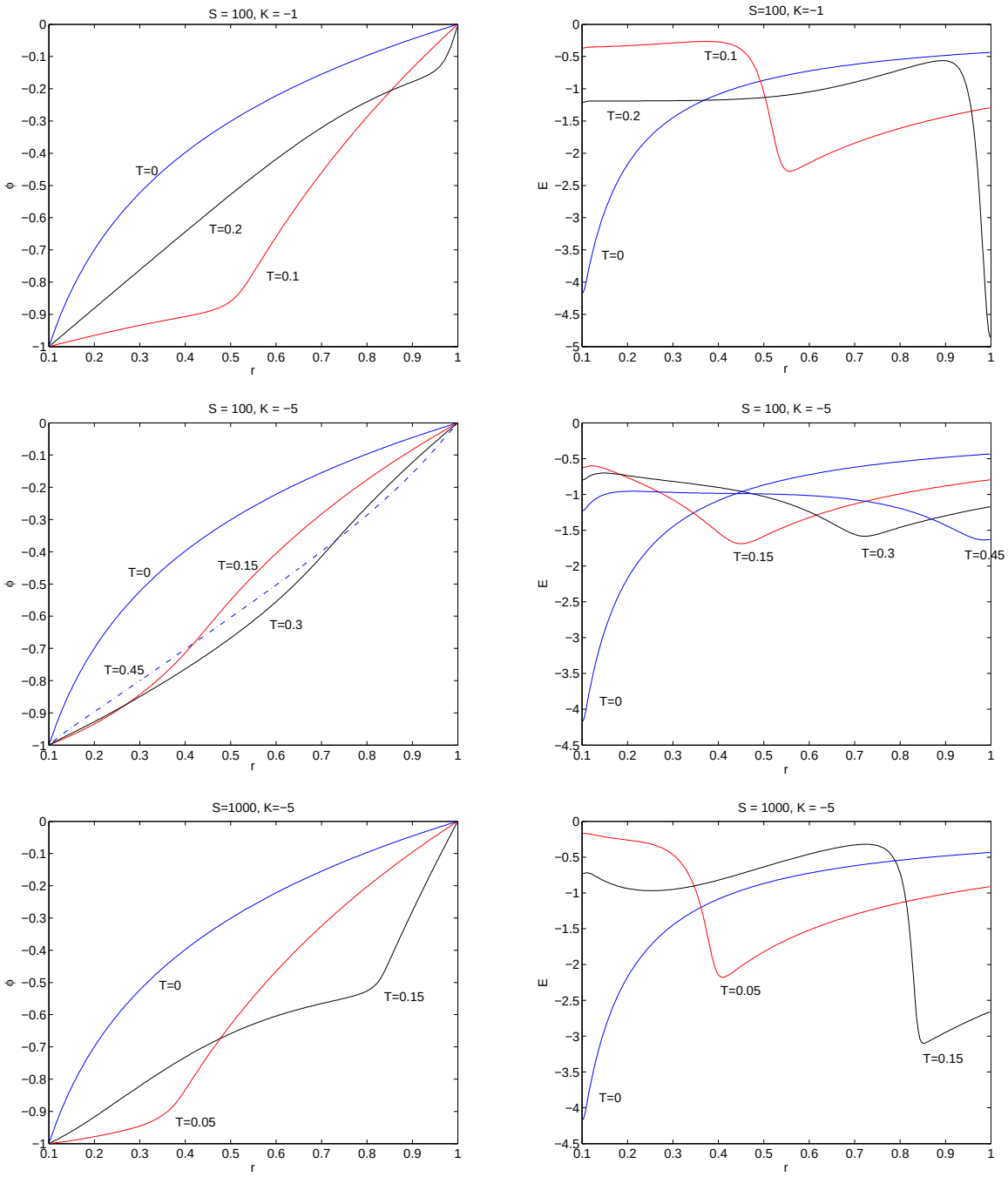

Figure 3.4: Effects of different S or K on the electric potential and field.

Chapter 4

Numerical Methods and Results for 2D Model

Let us consider 2D model (1.8). To facilitate the interpretation of numerical schemes, the 2D model is rewritten by

$$\begin{cases} \frac{\partial \sigma}{\partial t} + \nabla \cdot (\mu_\sigma \sigma \mathbf{E} - \mathbb{D}\nabla\sigma) = S|\mathbf{E}|e^{K/|\mathbf{E}|}\sigma, \ (x,y) \in \Omega, t > 0, \\ \frac{\partial \rho}{\partial t} + \nabla \cdot (\mu_\rho \rho \mathbf{E}) = S|\mathbf{E}|e^{K/|\mathbf{E}|}\sigma, \ (x,y) \in \Omega, t > 0, \\ -\nabla^2 \phi = \rho - \sigma, \ \mathbf{E} = -\nabla\phi, \ (x,y) \in \Omega, t > 0, \end{cases} \tag{4.1}$$

where we consider a rectangular domain $\Omega = (0, L_x) \times (0, L_y)$ for simplicity and $\mathbb{D} = \begin{pmatrix} D_x & 0 \\ 0 & D_y \end{pmatrix}$ is the diffusion coefficient matrix.

The initial and boundary conditions are posed by

$$\sigma(x,y,0) = \sigma_0(x,y), \ \rho(x,y,0) = \rho_0(x,y), \ (x,y) \in \Omega;$$

$$\frac{\partial \sigma}{\partial \mathbf{n}} = \frac{\partial \rho}{\partial \mathbf{n}} = 0 \ \text{ on } \partial\Omega;$$

$$\phi(x,0,t) = 0, \ \phi(x,L_y,t) = 1, \ \frac{\partial \phi}{\partial x}(0,y,t) = \frac{\partial \phi}{\partial x}(L_x,y,t) = 0,$$

where $\partial\Omega$ is the boundary of the domain Ω and $\mathbf{n}$ is the unit normal vector to the boundary exterior to Ω. Please refer to the following figure.

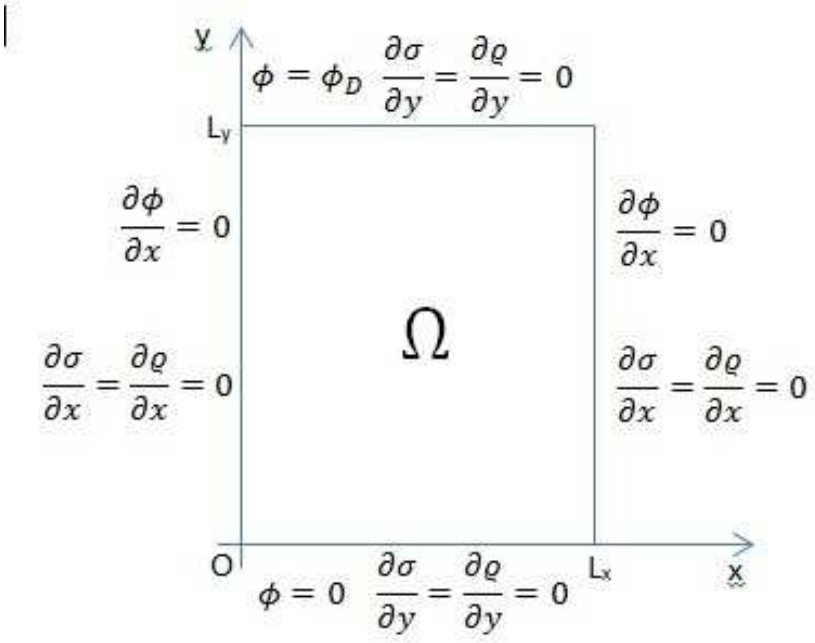

Figure 4.1: Boundary conditions for 2D model.

Note again that only the boundary conditions at inflow boundary of equation for ρ is the true boundary condition. The rest are used to compute numerical flux and slope limiter.

Let $\mathcal{E}_h$ be a partition of Ω such that $\mathcal{E}_h = \cup_{i=1}^{N} K_i$, where K_i is called element and h is the maximum element diameter. Assume the edges are denoted by e. Denote the sets of edges which belong to the Dirichlet boundary, the Neumann boundary and the interior of Ω by Γ_D, Γ_N and Γ_I respectively.

4.1 Numerical methods for Poisson's equation

If the computational domain has a simple geometry, for instant, the double-headed streamer propagation between two parallel planar electrodes, the finite difference

method (FDM) introduced by U. Ebert *et al.* [62] will be applied based on a uniform rectangular partition. However, if the geometry is complex, for example the Corbino disk [85, 92], rectangular partition will not work. In this case, we have to use a triangular partition on which the above FDM cannot be applied, but the discontinuous Galerkin (DG) methods [5, 95], the mixed finite element method (MFEM) [14, 15] and the least-squares finite element method (LSFEM) [8, 9] could do a good job. Besides, DG method can be also implemented on rectangular partition, therefore it will compete with FDM in simple geometries.

Before introducing the numerical methods, we suppose the computational domain is always $\Omega = (0, L_x)\times(0, L_y)$ for simplicity and rewrite the boundary condition on the Dirichlet boundary as

$$\phi(x, y) = \phi_D(x, y), \text{ on } \Gamma_D.$$

4.1.1 The finite difference method

In this method, the numerical solution for Poisson's equation is defined in the center of elements. Suppose that there are N_x rectangles in x-direction and N_y rectangles in y-direction in a uniform mesh. Let $\triangle x = \frac{L_x}{N_x}$ and $\triangle y = \frac{L_y}{N_y}$. Let the coordinates of the center of element $K_{i,j}$ be $x_i = (i - \frac{1}{2})\triangle x$ and $y_j = (j - \frac{1}{2})\triangle y$ and let $\phi_{i,j}$ approximate $\phi(x_i, y_j)$. The standard second order central approximation reads,

$$-\frac{\phi^n_{i-1,j} - 2\phi^n_{i,j} + \phi^n_{i+1,j}}{(\triangle x)^2} - \frac{\phi^n_{i,j-1} - 2\phi^n_{i,j} + \phi^n_{i,j+1}}{(\triangle y)^2} = \rho^n_{i,j} - \sigma^n_{i,j}, \tag{4.2}$$

for $i = 1, 2, \cdots, N_x$ and $j = 1, 2, \cdots, N_y$, where $\rho^n_{i,j}$ and $\sigma^n_{i,j}$ are the values of ρ and σ in element centers respectively. The boundary conditions are strongly imposed by introducing ghost cells. If the boundary condition is imposed by Dirichlet type, then a linear interpolation will be used. If the boundary condition is given by Neumann type, then we use reflection.

$$\phi^n_{0,j} = \phi^n_{1,j},\ \phi^n_{N_x+1,j} = \phi^n_{N_x,j},\ j = 1, 2, \cdots, N_y;$$

$$\phi^n_{i,0} = 2\phi_D(x_i, 0) - \phi^n_{i,1},\ \phi^n_{i,N_y+1} = 2\phi_D(x_i, 1) - \phi^n_{i,N_y},\ i = 1, 2, \cdots, N_x.$$

Next, we need to define the numerical approximation of $\mathbf{E}^n$. Since the geometry is very simple, we can directly define $\mathbf{E}^n \cdot \mathbf{n}$ along the edge of any element K_{ij}.

$$\begin{aligned}
&\text{On the top edge: } \mathbf{E}^n \cdot \mathbf{n} = \frac{\phi^n_{i,j} - \phi^n_{i,j+1}}{\triangle y};\\
&\text{on the bottom edge: } \mathbf{E}^n \cdot \mathbf{n} = \frac{\phi^n_{i,j-1} - \phi^n_{i,j}}{\triangle y};\\
&\text{on the left edge: } \mathbf{E}^n \cdot \mathbf{n} = \frac{\phi^n_{i-1,j} - \phi^n_{i,j}}{\triangle x};\\
&\text{on the right edge: } \mathbf{E}^n \cdot \mathbf{n} = \frac{\phi^n_{i,j} - \phi^n_{i+1,j}}{\triangle x}.
\end{aligned} \tag{4.3}$$

And we define $\mathbf{E}^n$ in the interior as

$$\mathbf{E}^n = \left(\frac{\phi^n_{i-1,j} - \phi^n_{i+1,j}}{2\triangle x}, \frac{\phi^n_{i,j-1} - \phi^n_{i,j+1}}{2\triangle y} \right)^T. \tag{4.4}$$

4.1.2 The discontinuous Galerkin method

Denote the finite element space by

$$V_k = \{v : v|_{K_i} \in \mathbb{P}_k(K_i), \text{ for } i = 1, 2, \cdots, N\},$$

where $\mathbb{P}_k(K_i)$ is the space of polynomials of degree up to k on K_i.

Suppose $e \in \Gamma_I$ is shared by two adjacent elements K_i and K_j, we define the average $\{\cdot\}$ and the jump $[\cdot]$ for scalar-valued function v and vector-valued function $\mathbf{u}$ as follows. Firstly, let

$$v_i = \lim_{x \in K_i, x \to \partial K_i} v(x), \ \mathbf{u}_i = \lim_{x \in K_i, x \to \partial K_i} \mathbf{u}(x).$$

Then we define

$$\{v\} = \frac{1}{2}(v_i + v_j), \ \{\mathbf{u}\} = \frac{1}{2}(\mathbf{u}_i + \mathbf{u}_j), \tag{4.5}$$

and

$$[v] = v_i \mathbf{n}_i + v_j \mathbf{n}_j, \ [\mathbf{u}] = \mathbf{u}_i \cdot \mathbf{n}_i + \mathbf{u}_j \cdot \mathbf{n}_j, \tag{4.6}$$

where $\mathbf{n}_i$ ($\mathbf{n}_j$) is the unit outer normal of element K_i (K_j).

If $e \in \Gamma_D \cup \Gamma_N$ is the edge of some element K_i, then the average and jump are defined only from one side,

$$\{v\} = v_i,\ \{\mathbf{u}\} = \mathbf{u}_i;\ [v] = v_i\mathbf{n}_i,\ [\mathbf{u}] = \mathbf{u}_i \cdot \mathbf{n}_i. \tag{4.7}$$

Define the symmetric bilinear form $B_\epsilon : V_k \times V_k \to \mathbb{R}$,

$$\begin{aligned} B_\epsilon(u,v) &= \sum_{K_i} \int_{K_i} \nabla u \cdot \nabla v - \sum_{e \in \Gamma_I \cup \Gamma_D} \int_e \{\nabla u\} \cdot [v] \\ &+ \epsilon \sum_{e \in \Gamma_I \cup \Gamma_D} \int_e \{\nabla v\} \cdot [u] + \sum_{e \in \Gamma_I \cup \Gamma_D} \frac{\alpha_e}{|e|^\beta} \int_e [u] \cdot [v], \end{aligned} \tag{4.8}$$

and linear form $L : V_k \to \mathbb{R}$,

$$L(v) = \int_\Omega (\rho^n - \sigma^n)v + \sum_{e \in \Gamma_D} \int_e \left(\epsilon \nabla v \cdot \mathbf{n} + \frac{\alpha_e}{|e|^\beta} v \right) \phi_D. \tag{4.9}$$

Then the DG method is to find $\phi^h \in V_k$ such that

$$B_\epsilon(\phi^h, v) = L(v),\ \forall v \in V_k. \tag{4.10}$$

The DG method has different properties depending on the choice of parameters ϵ, α_e and β. Here we choose $\epsilon = -1$ to form a symmetric linear system which leads to symmetric interior penalty Galerkin (SIPG) method and choose

$$\beta = 1,\ \alpha_e = \begin{cases} 3k(k+1), & \text{if } e \in \Gamma_I, \\ 6k(k+1), & \text{if } e \in \Gamma_D \cup \Gamma_N, \end{cases}$$

to ensure optimal convergence.

The numerical approximation of electric field is derived from ϕ^h by the following way. In each element,

$$\mathbf{E}^n = -\nabla \phi^h. \tag{4.11}$$

Along the edge, since ϕ^h is allowed to be discontinuous, there is a penalty term in the above scheme,

$$\mathbf{E}^n = \begin{cases} -\{\nabla \phi^h\} + \frac{\alpha_e}{|e|^\beta}[\phi^h], & \text{if } e \in \Gamma_I, \\ -\nabla \phi^h, & \text{if } e \in \Gamma_N, \\ -\nabla \phi^h + \frac{\alpha_e}{|e|^\beta}(\phi^h - \phi_D)\mathbf{n}, & \text{if } e \in \Gamma_D. \end{cases} \tag{4.12}$$

Remark 1. One can refer to [5] for the derivation of DG scheme for elliptic problem. The different choices of ϵ, α_e and β comes from different settings of numerical fluxes (see Table 3.1 and 3.2 in [5]). For the proof of optimal convergence of a variety of DG methods, one can refer to [84].

Remark 2. Note that, in this DG scheme, the jump in both artificial terms (symmetric and penalty terms) is used for numerical solution. Therefore, the scheme is automatically consistent with the weak formulation of Poisson's equation. Furthermore, both artificial terms become weaker when the mesh is finer. In other words, the artificial terms will not affect the convergence of numerical solution for fixed values of artificial parameters.

Remark 3. As suggested in [84] that SIPG can provide optimal convergence rate for all degrees of approximation polynomials compared with non-symmetric interior penalty Galerkin (NIPG, $\epsilon = 1$) and incomplete interior penalty Galerkin (IIPG, $\epsilon = 0$) methods. The convergence rate for the later two methods are suboptimal for even degrees. To ensure the optimal convergence, β should be larger than some critical value (this value only depends on dimension) for superpenalization. Besides, the penalty parameter α in SIPG should be larger than some threshold; otherwise, the numerical solution will not converge to the exact solution.

4.1.3 The mixed finite element method

In this method, the Poisson's equation is reformulated by a first order differential equation system,

$$\begin{cases} \nabla \cdot \mathbf{E} = \rho^n - \sigma^n, \\ -\nabla\phi = \mathbf{E}, \end{cases} \tag{4.13}$$

then we can treat ϕ and $\mathbf{E}$ as independent variables which means $\mathbf{E}$ can be directly solved instead of being derived from approximation of ϕ. Usually, we call ϕ the scalar variable and $\mathbf{E}$ the flux variable. Define the space

$$H_N(\Omega, div) = \{\mathbf{v} \in H(\Omega, div) : \mathbf{v} \cdot \mathbf{n} = 0 \text{ on } \Gamma_N\},$$

where

$$H(\Omega, div) = \{\mathbf{v} \in \mathbf{L}^2 : \nabla \cdot \mathbf{v} \in L^2\}.$$

By multiplying the equations in (4.13) by test functions in L^2 and $H_N(\Omega, div)$ respectively, applying integration by parts to the second equation and using the boundary conditions, the MFEM is to seek a pair $(\phi, \mathbf{E}) \in L^2 \times H_N(\Omega, div)$ such that

$$\begin{cases} \int_\Omega \mathbf{E} \cdot \mathbf{v} - \int_\Omega \phi \nabla \cdot \mathbf{v} = -\int_{\Gamma_D} \phi_D \mathbf{v} \cdot \mathbf{n}, & \forall \mathbf{v} \in H_N(\Omega, div), \\ -\int_\Omega \psi \nabla \cdot \mathbf{E} = -\int_\Omega (\rho^n - \sigma^n)\psi, & \forall \psi \in L^2. \end{cases} \tag{4.14}$$

Define the conforming, finite dimensional subspace of $H_N(\Omega, div)$ in the discretization level [30],

$$\begin{aligned} W_F^{mfem} \quad = \quad & \{\mathbf{v} \in H_N(\Omega, div) : v|_{K_i} \in W_k(K_i), \text{ for } i = 1, \cdots, N; \\ & \mathbf{v} \cdot \mathbf{n} \text{ is continuous across all the edges.}\}. \end{aligned} \tag{4.15}$$

There are two kinds of approximating space $W_k(K)$. One is called Raviart-Thomas (RT_k) space, the other is called Brezzi-Douglas-Marini (BDM_k) space;

$$RT_k(K) \equiv (\mathbb{P}_k(K))^2 + \mathbf{x}\mathbb{P}_k(K), \ BDM_k \equiv (\mathbb{P}_k(K))^2.$$

Although ϕ and $\mathbf{E}$ are independent variables in MFEM, we still have to define the subspace of L^2 for scalar variable according to the definition of W_F^{mfem} such that the so-called inf-sup (stability) condition is satisfied; more precisely,

$$W_S^{mfem} = \nabla \cdot W_F^{mfem}. \tag{4.16}$$

Therefore, the discretization scheme for MFEM is to find $(\phi^h, \mathbf{E}^h) \in W_S^{mfem} \times W_F^{mfem}$ such that

$$\begin{cases} \int_\Omega \mathbf{E}^h \cdot \mathbf{v} - \int_\Omega \phi^h \nabla \cdot \mathbf{v} = -\int_{\Gamma_D} \phi_D \mathbf{v} \cdot \mathbf{n}, & \forall \mathbf{v} \in W_F^{mfem}, \\ -\int_\Omega \psi \nabla \cdot \mathbf{E}^h = -\int_\Omega (\rho^n - \sigma^n)\psi, & \forall \psi \in W_S^{mfem}. \end{cases} \tag{4.17}$$

Since $\mathbf{E}^h \cdot \mathbf{n}$ is continuous across the edges by the definition of subspace. Thus, the approximate electric field is naturally chosen as $\mathbf{E}^n = \mathbf{E}^h$.

4.1.4 The least-squares finite element method

The LSFEM starts from (4.13). But the difference is that we want to minimize a functional

$$J(\phi, \mathbf{E}) = ||\nabla \cdot \mathbf{E} - (\rho^n - \sigma^n)||^2_{L^2(\Omega)} + ||\mathbf{E} + \nabla\phi||^2_{\mathbf{L}^2(\Omega)}$$

on $H^1_D \times H_N(\Omega, div)$, where $H^1_D = \{\psi \in H^1 : \psi = \phi_D \text{ on } \Gamma_D\}$ and $H_N(\Omega, div)$ is given in MFEM.

The choices of finite dimensional subspaces in LSFEM are not required to satisfy the inf-sup condition, thus it is relatively easier to define some simple conforming subspaces. Denote the C^0 nodal finite element subspace by

$$W_k = \{v : v|_{K_i} \in \mathbb{P}_k(K_i), \text{ for } i = 1, 2, \cdots, N, v \text{ in continuous in } \Omega\}.$$

Let

$$W_S^{lsfem} = W_k \cap \{v : v|_{\Gamma_D} = \phi_D\} \tag{4.18}$$

and

$$W_F^{lsfem} = (W_k)^2 \cap \{\mathbf{v} : \mathbf{v} \cdot \mathbf{n} = 0, \text{ on } \Gamma_N\} \tag{4.19}$$

be the subspace for scalar variable and flux variable respectively. Let $W_k^0 = W_k \cap \{v : v|_{\Gamma_D} = 0\}$ be the space for test functions.

By taking the first variation of the functional $J(\phi, \mathbf{E})$, we can obtain

$$\begin{aligned}
& \left.\frac{dJ(\phi + t\psi, \mathbf{E} + t\mathbf{v})}{dt}\right|_{t=0} \\
= \; & \frac{d}{dt}\left\{\int_\Omega [\nabla \cdot (\mathbf{E} + t\mathbf{v}) - (\rho^n - \sigma^n)]^2 + \int_\Omega |(\mathbf{E} + t\mathbf{v}) + \nabla(\phi + t\psi)|^2\right\}\Big|_{t=0} \\
= \; & 2\int_\Omega [\nabla \cdot (\mathbf{E} + t\mathbf{v}) - (\rho^n - \sigma^n)](\nabla \cdot \mathbf{v}) + 2\int_\Omega [(\mathbf{E} + t\mathbf{v}) + \nabla(\phi + t\psi)] \cdot (\mathbf{v} + \nabla\psi)\Big|_{t=0} \\
= \; & 2\int_\Omega [\nabla \cdot \mathbf{E} - (\rho^n - \sigma^n)](\nabla \cdot \mathbf{v}) + 2\int_\Omega (\mathbf{E} + \nabla\phi) \cdot (\mathbf{v} + \nabla\psi),
\end{aligned}$$

for all $\psi \in H^1_0$ and $\mathbf{v} \in H_N(\Omega, div)$. Letting the first variation be equal to zero, we can have

$$\int_\Omega (\nabla \cdot \mathbf{E})(\nabla \cdot \mathbf{v}) + \int_\Omega (\mathbf{E} + \nabla\phi) \cdot (\mathbf{v} + \nabla\psi) = \int_\Omega (\rho^n - \sigma^n)(\nabla \cdot \mathbf{v}).$$

Therefore, we define the bilinear form

$$B[(\phi, \mathbf{E}); (\psi, \mathbf{v})] = \int_\Omega (\nabla \cdot \mathbf{E})(\nabla \cdot \mathbf{v}) + \int_\Omega (\mathbf{E} + \nabla\phi) \cdot (\mathbf{v} + \nabla\psi), \tag{4.20}$$

and a linear functional

$$L(\mathbf{v}) = \int_\Omega (\nabla \cdot \mathbf{v})(\rho^n - \sigma^n). \tag{4.21}$$

Then the LSFEM is to find the pair $(\phi^h, \mathbf{E}^h) \in W_S^{lsfem} \times W_F^{lsfem}$ such that

$$B[(\phi^h, \mathbf{E}^h); (\psi, \mathbf{v})] = L(\mathbf{v}),\ \forall (\psi, \mathbf{v}) \in W_k^0 \times W_F^{lsfem}. \tag{4.22}$$

Since the flux variable $\mathbf{E}^h$ is continuous in LSFEM, $\mathbf{E}_h \cdot \mathbf{n}$ is automatically continuous across the edges. Thus, the approximate electric field is naturally chosen as $\mathbf{E}^n = \mathbf{E}^h$.

Remark 1: Here we use the C^0 nodal finite element subspace; however, other subspaces such as RT_k or BDM_k are feasible as well. If we want to make the accuracy comparable for different methods, we should apply RT_0 or BDM_1.

Remark 2: C^0 nodal finite element subspace is relatively easier for implementation than RT_k and BDM_k. However, it is suggested in [9] that the use of nodal subspace for flux variable will degrade the accuracy while the use of RT_k or BDM_k subspace can result in the local conservation and optimal L^2-convergence of the flux variable. The only nodal subspace that can derive the optimal L^2 error estimate is the piecewise linear subspace defined on a uniform criss-cross grid [32].

4.2 Numerical method for continuity equations

As we know, an auxiliary equation has to be solved in every single time step in LDG method. As a result, LDG method requires more computational time than OBBDG method. Therefore, we only choose OBBDG method for solving continuity equations in 2D and quasi 3D simulations.

4.2.1 The Oden-Babuška-Baumann DG method

By the derivation in [84], the diffusion term $-\nabla\cdot(\mathbb{D}\nabla\sigma)$ is discretized by the bilinear form (4.8) with symmetric parameter $\epsilon = 1$ and penalty parameter $\alpha_e = 0$. Due to the homogeneous Neumann boundary condition, we only consider the interior edges:

$$B(u,v) = \sum_{i=1}^{N}\int_{K_i}\mathbb{D}\nabla u\cdot\nabla v - \sum_{e\in\Gamma_I}\int_e\{\mathbb{D}\nabla u\}\cdot[v] + \sum_{e\in\Gamma_I}\int_e\{\mathbb{D}\nabla v\}\cdot[u]. \tag{4.23}$$

The convection terms $\nabla\cdot(\mu_P P\mathbf{E})$ for $P = \sigma$ or ρ is discretized by

$$\begin{aligned} C(P,v;\mathbf{E}) &= -\sum_{i=1}^{N}\int_{K_i}P(\mu_P\mathbf{E}\cdot\nabla v) + \sum_{e\in\Gamma_I}\int_e\widehat{P}(\mu_P\mathbf{E}\cdot[v]) \\ &+ \sum_{e\in\Gamma_N}\int_e P(\mu_P\mathbf{E}\cdot\mathbf{n})v, \end{aligned} \tag{4.24}$$

with numerical flux

$$\widehat{P} = \begin{cases} P_i, & \text{if } \mu_P\mathbf{E}\cdot\mathbf{n}_i \geq 0, \\ P_j, & \text{if } \mu_P\mathbf{E}\cdot\mathbf{n}_i < 0, \end{cases} \tag{4.25}$$

for any interior edge $e = K_i \cap K_j$. And the source term $S|\mathbf{E}|e^{K/|\mathbf{E}|}\sigma$ is discretized by a linear form,

$$L(\sigma,v;\mathbf{E}) = \int_\Omega S|\mathbf{E}|e^{K/|\mathbf{E}|}\sigma v. \tag{4.26}$$

Therefore, the OBBDG method is to find $\sigma^h(t), \rho^h(t) \in V_k$ such that

$$\int_\Omega(\sigma^h(0)-\sigma_0)v = \int_\Omega(\rho^h(0)-\rho_0)v = 0,\ \forall v\in V_k; \tag{4.27}$$

and

$$\begin{aligned} &\int_\Omega\frac{\partial\sigma^h}{\partial t}v + C(\sigma^h(t),v;\mathbf{E}(t)) + B(\sigma^h(t),v) = L(\sigma^h(t),v;\mathbf{E}(t)),\ \forall v\in V_k, \\ &\int_\Omega\frac{\partial\rho^h}{\partial t}v + C(\rho^h(t),v;\mathbf{E}(t)) = L(\sigma^h(t),v;\mathbf{E}(t)),\ \forall v\in V_k, \end{aligned} \tag{4.28}$$

for all $t > 0$.

4.2.2 The slope limiter

In contrast to 1D simulation, one may construct rectangular or triangular mesh for 2D simulation according to the computational domain. Although the slope limiters used in the rectangular and triangular element cases will have some difference, their essential motivation is same: (1) to preserve the cell average, (2) to lessen the gradient of numerical solutions.

The slope limiter on rectangular mesh. If the partition is based on rectangular elements, we assume that the partition $\mathcal{E}_h$ is uniform with mesh size $\triangle x$ and $\triangle y$, the element centered at (x_i, y_j) is denoted by $K_{i,j} = [x_i - \triangle x/2, x_i + \triangle x/2] \times [y_j - \triangle y/2, y_j + \triangle y/2]$. One can construct a tensor-product basis, then the numerical solution in element $K_{i,j}$ can be presented by

$$U_{i,j} = \sum_{p,q=0}^{p+q=k} u_{i,j}^{p,q} \phi_p(\xi) \psi_q(\eta), \tag{4.29}$$

where $\xi = \frac{x-x_i}{\triangle x/2}$, $\eta = \frac{y-y_j}{\triangle y/2}$. One can still use Legendre polynomials.

If $k = 1$ (piecewise linear approximation), the limiter is exactly the same as in [19]. The reconstructed coefficients $\tilde{u}_{i,j}^{1,0}$ and $\tilde{u}_{i,j}^{0,1}$ are given by

$$\tilde{u}_{i,j}^{1,0} = minmod(u_{i,j}^{1,0}, u_{i+1,j}^{0,0} - u_{i,j}^{0,0}, u_{i,j}^{0,0} - u_{i-1,j}^{0,0}),$$

and

$$\tilde{u}_{i,j}^{0,1} = minmod(u_{i,j}^{0,1}, u_{i,j+1}^{0,0} - u_{i,j}^{0,0}, u_{i,j}^{0,0} - u_{i,j-1}^{0,0}),$$

where the minmod function is defined by

$$minmod(a, b, c) = \begin{cases} s \min\{|a|, |b|, |c|\}, & \text{if } s = sign(a) = sign(b) = sign(c), \\ 0, & \text{otherwise.} \end{cases}$$

Here, we do not apply the total variation bounded (TVB) minmod function since it requires a TVB constant which is an empirical value differs from case to case.

If $k > 1$, the limiter becomes more complicated. To reconstruct the coefficients $u_{i,j}^{p,0}$ and $u_{i,j}^{0,q}$, we directly apply the one-dimensional limiter [46] in corresponding

direction (refer to (2.33) and (2.34)). When both p and q are positive, which means the coefficient $u_{i,j}^{p,q}$ corresponds to the mixed partial derivatives, we have to use the coefficients in both x- and y-directions at the previous level to reconstruct $u_{i,j}^{p,q}$. This reconstruction is given by [46]

$$\begin{aligned}\tilde{u}_{i,j}^{p,q} = minmod\left(u_{i,j}^{p,q}, \alpha_q(u_{i,j+1}^{p,q-1} - u_{i,j}^{p,q-1}), \alpha_q(u_{i,j}^{p,q-1} - u_{i,j-1}^{p,q-1}),\right. \\ \left.\alpha_p(u_{i+1,j}^{p-1,q} - u_{i,j}^{p-1,q}), \alpha_p(u_{i,j}^{p-1,q} - u_{i-1,j}^{p-1,q})\right),\end{aligned} \tag{4.30}$$

where

$$\frac{1}{2\sqrt{4n^2-1}} \leq \alpha_n \leq \sqrt{\frac{2n-1}{2n+1}}. \tag{4.31}$$

The upper bound for α_n leads to the least diffusive solution, thus it will be used in practice.

The slope limiter on triangular mesh. If the partition is based on triangular meshes, we apply the hierarchical reconstruction (HR) technique proposed by Yingjie Liu, Chi-Wang Shu and *et. al.* [50, 98]. The idea of HR is to use a series of first order reconstructions to reconstruct a high order polynomial hierarchically such that the cell averages of various orders of derivatives of the polynomial are unchanged during the reconstruction process. Here, we explain the reconstruction process for linear approximation.

Suppose the numerical solution on element K_i can be represented by

$$u_i(x - x_i, y - y_i) = u_i(0,0) + \partial_x u_i(0,0)(x - x_i) + \partial_y u_i(0,0)(y - y_i), \tag{4.32}$$

where (x_i, y_i) is the centroid of K_i. Let $\{K_i, K_{i_1}, K_{i_2}, K_{i_3}\}$ be a set of element K_i and its adjacent elements. Our job is to find a new linear polynomial

$$L_i(x - x_i, y - y_i) = \widetilde{u}_i(0,0) + \partial_x \widetilde{u}_i(0,0)(x - x_i) + \partial_y \widetilde{u}_i(0,0)(y - y_i) \tag{4.33}$$

to replace $u_i(x - x_i, y - y_i)$ by preserving the cell averages.

Since there are three unknowns in the reconstruction polynomial, we can preserve the cell averages on K_i itself and its two different adjacent cells. Therefore, it is able to form three different stencils: $\{K_i, K_{i_2}, K_{i_3}\}$, $\{K_i, K_{i_3}, K_{i_1}\}$ and $\{K_i, K_{i_1}, K_{i_2}\}$;

and we are able to find three reconstructions based on each of these stencils. Take the first stencil for example, denote the reconstructed polynomial by L_{i_1}. Preserving cell averages implies

$$\frac{1}{|K_j|}\int_{K_j} L_{i_1}(x-x_i, y-y_i)dxdy = \frac{1}{|K_j|}\int_{K_j} u_j(x-x_j, y-y_j)dxdy \tag{4.34}$$

for $j = i, i_2, i_3$. There are three equations so that the coefficients in (4.33) are uniquely determined.

Once we obtain all the three linear polynomials L_{i_1}, L_{i_2} and L_{i_3} (they are called candidates in [98].), the reconstructed linear polynomial for element K_i is a convex combination of these polynomials,

$$L_i(x-x_i, y-y_i) = \sum_{j=1}^{3} w_j L_{i_j}(x-x_i, y-y_i). \tag{4.35}$$

The weights are designed such that the reconstructed polynomial is free of discontinuity [98]. Set

$$w_j = \frac{\alpha_j}{\sum_{k=1}^{3}\alpha_k}, \tag{4.36}$$

where

$$\alpha_j = \frac{d_j}{[\epsilon + (\partial_x \widetilde{u}_{i_j}(0,0))^2 + (\partial_y \widetilde{u}_{i_j}(0,0))^2]^2} \tag{4.37}$$

with

$$d_j = \frac{1/\theta_j}{\sum_{k=1}^{3} 1/\theta_k} \tag{4.38}$$

and θ_j is the condition number of the coefficient matrix in solving the linear equations (4.34) on the j-th stencil.

If the approximated polynomial $u_i(x-x_i, y-y_i)$ is of degree n which is larger than one, then for $m = n, n-1, \cdots, 2$ we take all possible combinations of the $(m-1)$th order partial derivatives of $u_i(x-x_i, y-y_i)$ to find all the possible candidates for reconstructing the coefficients in the mth degree term. After that, we apply the above procedure to reconstruct the coefficients in first and zero-th degree term. Readers can find more details in [50, 98].

4.3 Numerical tests and comparisons

Since we use nodal and piecewise linear subspace in LSFEM, we have to choose linear polynomial approximation in OBBDG method and SIPG method and choose RT_0 and BDM_1 subspaces in MFEM to make our methods comparable.

The method for solving continuity equations is fixed by OBBDG method, thus in Table 4.1 we want to analyze the number of unknowns in one single time step for each method to solve Poisson's equation. For simplicity, the tests and comparisons will be carried out in a rectangular domain. Firstly, we generate a uniform rectangular mesh to compare FDM and SIPG method. Then based on this rectangular partition, we apply the criss-cross grid to compare MFEM, LSFEM and SIPG method. Suppose there are N_x rectangles in x-direction and N_y rectangles in y-direction. Dirichlet boundary conditions are posed on two horizontal boundaries and the other two are posed by Neumann boundary conditions. From this table, it can be concluded that FDM is more efficient than SIPG on rectangular mesh. On triangular mesh, the efficiency can be ranged by: $RT_0 >$ LSFEM $>$ SIPG $> BDM_1$, where ">" means more efficient.

Method	No. of unknowns
FDM	N_xN_y
Rectangular SIPG	$3N_xN_y$
Triangular SIPG	$12N_xN_y$
RT_0 MFEM	$6N_xN_y + N_x - N_y$
BDM_1 MFEM	$2(6N_xN_y + N_x - N_y)$
LSFEM	$6N_xN_y + N_x + N_y - 1$

Table 4.1: Number of unknowns in one single time step for different methods to solve Poisson's equation.

Test 1. Rectangular mesh. In this test, we only compare FDM+OBBDG method

and SIPG+OBBDG method. Consider Model (1.5) on a rectangular domain $\Omega = [0,1]\times[0,2]$ with toy parameters: $S = 1000$, $K = -5$, $\mu_\sigma = -1$, $\mu_\rho = 0.5$, $\mathbb{D} = 10^{-4}\mathbf{I}$. The background electric field is given by $\mathbf{E}|_{t=0} = (0,-1)^T$. The initial data of continuity equations is

$$\sigma|_{t=0} = \rho|_{t=0} = \exp\{-25[(z-0.5)^2 + (y-0.5)^2]\}.$$

The terminal time is set to be $T = 0.5$. The 'exact' solutions are numerically defined by using very fine mesh, namely $h = \frac{1}{128}$, and tiny time step size $\tau = 10^{-4}$. In order to compare the convergence rate in space for each coupled method, the time step is chosen as small enough. The results from Tables 4.2 - 4.4 indicate that both methods can converge and have the same order of accuracy. This means FDM+OBBDG method is on a par with SIPG+OBBDG method from accuracy point of view. But we recommend FDM+OBBDG method in simulation by considering efficiency.

		$h_0 = \frac{1}{8}$	$h_0/2$	$h_0/2^2$	$h_0/2^3$
FDM	error	0.0838	0.0274	0.0080	0.0023
+OBBDG	rate	-	1.6121	1.7683	1.7842
SIPG	error	0.0763	0.0248	0.0080	0.0023
+OBBDG	rate	-	1.6189	1.6366	1.7647

Table 4.2: Error and convergence rate for σ in 2D comparison based on rectangular mesh.

Test 2. Triangular mesh. In this test, we compare SIPG+OBBDG, LSFEM+OBBDG, RT_0+OBBDG and BDM_1+OBBDG methods. For simplicity, we consider the similar toy model with Test 1, except that the computational domain is $\Omega = [0,1]\times[0,1]$ and terminal time is $T = 0.1$. The 'exact' solutions are numerically defined by using very fine mesh, namely $h = \frac{1}{128}$, and tiny time step size $\tau = 10^{-4}$. In order to compare the convergence rate in space for each coupled method, the time step is chosen as small enough. From Tables 4.5 - 4.8, we can observe that (1) the convergence

		$h_0 = \frac{1}{8}$	$h_0/2$	$h_0/2^2$	$h_0/2^3$
FDM	error	0.0872	0.0276	0.0095	0.0029
+OBBDG	rate	-	1.6592	1.5382	1.7202
SIPG	error	0.0781	0.0261	0.0095	0.0029
+OBBDG	rate	-	1.5817	1.4562	1.7196

Table 4.3: Error and convergence rate for ρ in 2D comparison based on rectangular mesh.

		$h_0 = \frac{1}{8}$	$h_0/2$	$h_0/2^2$	$h_0/2^3$
FDM	error	0.0068	0.0022	7.5749E-4	2.3246E-4
+OBBDG	rate	-	1.6595	1.5755	1.7043
SIPG	error	0.0055	0.0018	6.2495E-4	1.8246E-4
+OBBDG	rate	-	1.5739	1.5511	1.7762

Table 4.4: Error and convergence rate for ϕ in 2D comparison based on rectangular mesh.

rate for particle density is only 1 in RT_0+OBBDG method while it is closed to 2 in the rest three methods; (2) the convergence rate for electric potential is about 1 in RT_0 or BDM_1+OBBDG method while it is about 2 in the other two methods; (3) the convergence rate for electric field is 1 in SIPG and RT_0+OBBDG methods while it is nearly 2 in the other two methods. These observations coincide with the expected theoretical results. From the accuracy point of view, one can simply conclude that LSFEM+OBBDG method should be the best choices if all the physical quantities are expected to have the highest accuracy. If we relax this requirement, SIPG+OBBDG or BDM_1+OBBDG could be taken into consideration. From the efficiency point of view, we would like to take a look at the memory cost in each method. It is found from Table 4.9 that (1) RT_0+OBBDG method is the worst one since it is of low resolution and cost much memory; (2) SIPG+OBBDG is actually more suitable to be applied into simulation than LSFEM+OBBDG method since the former method costs much less memory than the latter. In addition, Figure 4.2 shows the average time cost (unit: second) in a single step in each method. This result also recommends that SIPG+OBBDG method is more efficient than LSFEM/BDM_1+OBBDG method.

4.4 Numerical simulation

Example 1. Streamer bifurcation in a double-headed propagation.

This example is used to illustrate the bifurcation phenomenon in streamer propagation. In this simulation, we not only consider electrons and positive ions, but also take care of negative ions. We ignore the effects due to photoionization and diffusion of electrons. In addition, we assume that particle mobilities, impact ionization coefficient, attachment coefficient and recombination coefficient are all dependent

		$h_0 = \frac{1}{8}$	$h_0/2$	$h_0/2^2$	$h_0/2^3$
SIPG	error	0.0252	0.0073	0.0019	5.2221E-4
+OBBDG	rate	-	1.7947	1.9002	1.8962
LSFEM	error	0.0248	0.0071	0.0019	5.0995E-4
+OBBDG	rate	-	1.7945	1.9084	1.8992
RT_0	error	0.1739	0.0978	0.0527	0.0269
+OBBDG	rate	-	0.8305	0.8909	0.9733
BDM_1	error	0.0248	0.0071	0.0019	5.0999E-4
+OBBDG	rate	-	1.7952	1.9081	1.8988

Table 4.5: Error and convergence rate for σ in 2D comparison based on triangular mesh.

		$h_0 = \frac{1}{8}$	$h_0/2$	$h_0/2^2$	$h_0/2^3$
SIPG	error	0.0204	0.0062	0.0018	4.7288E-4
+OBBDG	rate	-	1.7164	1.7677	1.9466
LSFEM	error	0.0198	0.0060	0.0018	4.5522E-4
+OBBDG	rate	-	1.7301	1.7679	1.9473
RT_0	error	0.1554	0.0862	0.0484	0.0260
+OBBDG	rate	-	0.8509	0.8321	0.8986
BDM_1	error	0.0199	0.0060	0.0018	4.5529E-4
+OBBDG	rate	-	1.7306	1.7684	1.9479

Table 4.6: Error and convergence rate for ρ in 2D comparison based on triangular mesh.

		$h_0 = \frac{1}{8}$	$h_0/2$	$h_0/2^2$	$h_0/2^3$
SIPG	error	8.4389E-5	2.1507E-5	5.1824E-6	1.1109E-6
+OBBDG	rate	-	1.9722	2.0531	2.2219
LSFEM	error	2.0042E-4	5.2748E-5	1.3348E-5	3.1536E-6
+OBBDG	rate	-	1.9259	1.9825	2.0815
RT_0	error	0.0361	0.0181	0.0090	0.0045
+OBBDG	rate	-	1.0000	1.0000	1.0000
BDM_1	error	0.0361	0.0181	0.0090	0.0045
+OBBDG	rate	-	1.0000	1.0000	1.0000

Table 4.7: Error and convergence rate for ϕ in 2D comparison based on triangular mesh.

		$h_0 = \frac{1}{8}$	$h_0/2$	$h_0/2^2$	$h_0/2^3$
SIPG	error	0.0024	0.0012	5.8485E-4	2.6160E-4
+OBBDG	rate	-	1.0058	1.0346	1.1607
LSFEM	error	5.8821E-4	1.5971E-4	4.2639E-5	1.1274E-5
+OBBDG	rate	-	1.8809	1.9052	1.9192
RT_0	error	0.0026	0.0013	6.3681E-4	3.3134E-4
+OBBDG	rate	-	1.0144	1.0010	0.9466
BDM_1	error	4.8136E-4	1.2151E-4	3.0509E-5	7.6432E-6
+OBBDG	rate	-	1.9861	1.9937	1.9970

Table 4.8: Error and convergence rate for $\mathbf{E}$ in 2D comparison based on triangular mesh.

Method	Memory cost
SIPG+OBBDG	511.855M
RT_0+OBBDG	4.061G
BDM_1+OBBDG	9.886G
LSFEM+OBBDG	6.659G

Table 4.9: The memory cost for each method in the numerical tests under triangular mesh when $h = \frac{1}{64}$.

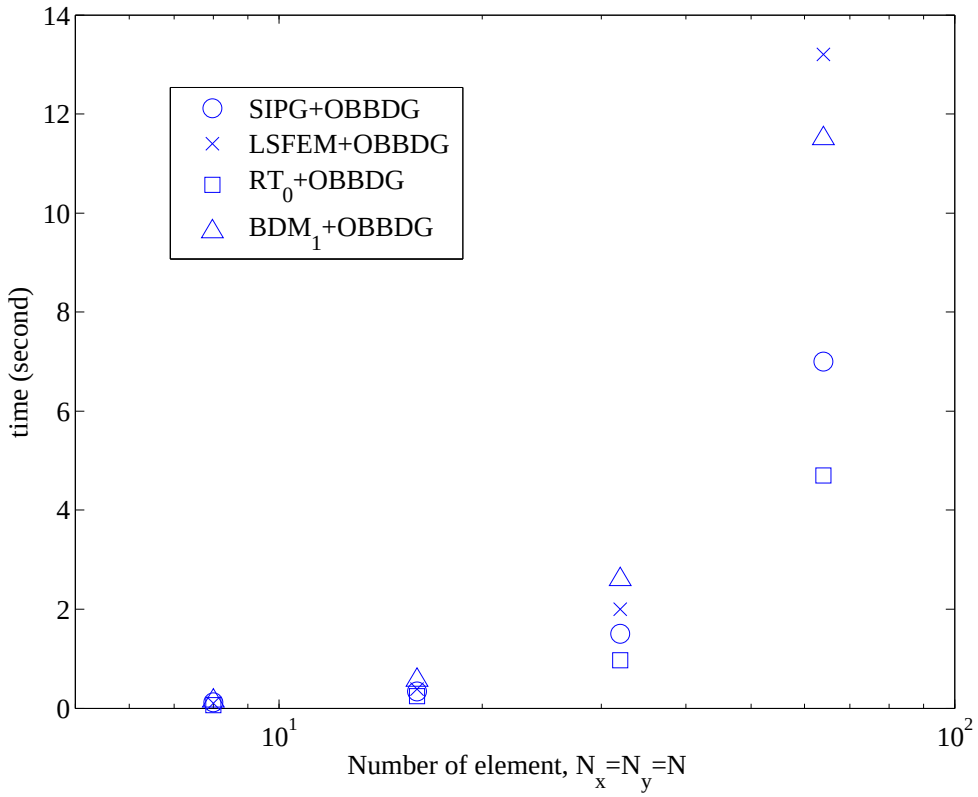

Figure 4.2: The average time cost in one single step for each method in the numerical tests under triangular mesh.

on electric field. Thus, we consider the following model,

$$\begin{cases} \frac{\partial N_e}{\partial t} + \nabla \cdot (N_e \mathbf{W}_e) = (\alpha(|\mathcal{E}|) - \eta(|\mathcal{E}|))N_e|\mathbf{W}_e| - \beta N_e N_p, \\ \frac{\partial N_p}{\partial t} + \nabla \cdot (N_p \mathbf{W}_p) = \alpha(|\mathcal{E}|)N_e|\mathbf{W}_e| - \beta N_e N_p - \beta N_n N_p, \\ \frac{\partial N_n}{\partial t} + \nabla \cdot (N_n \mathbf{W}_n) = \eta(|\mathcal{E}|)N_e|\mathbf{W}_e| - \beta N_n N_p, \\ -\nabla^2 V = \frac{e}{\epsilon}(N_p - N_e - N_n),\ \mathcal{E} = -\nabla V, \end{cases} \tag{4.39}$$

where the drift velocities $\mathbf{W}_{e,p,n}$, ionization coefficient $\alpha(|\mathcal{E}|)$, electron attachment coefficient $\eta(|\mathcal{E}|)$ and recombination coefficient β are taken from [65].

Consider a 5m gap between two parallel planar electrodes and a background electric field $[0, 3000]\ kV/m$. The truncated domain is $[0, 1m] \times [0, 5m]$. The initial data is given by [92],

$$N_e(x, y, 0) = N_p(x, y, 0) = 10^{20} \exp\left\{ -\left(\frac{x - 0.5m}{0.05m}\right)^2 - \left(\frac{y - 2.5m}{0.05m}\right)^2 \right\} + 10^6\ m^{-3},$$

and $N_n(x, y, 0) = 0$. The gas pressure is set to be atmospheric pressure.

By letting $x_0 = 5m,\ V_0 = 1.5 \times 10^7\ V,\ t_0 = 10^{-7}\ s$ and denoting $\tilde{x} = \frac{x}{x_0}$, $\tilde{y} = \frac{y}{x_0}$, $\tau = \frac{t}{t_0}$, $N_0 = \frac{V_0 \epsilon}{e x_0^2}$,

$$\sigma(\tilde{x}, \tilde{y}, \tau) = \frac{N_e(x, y, t)}{N_0},\ \rho(\tilde{x}, \tilde{y}, \tau) = \frac{N_p(x, y, t)}{N_0},\ \delta(\tilde{x}, \tilde{y}, \tau) = \frac{N_n(x, y, t)}{N_0},$$

$$\phi(\tilde{x}, \tilde{y}, \tau) = \frac{V(x, y, t)}{V_0},\ \mathbf{E} = \frac{\mathcal{E}}{V_0/x_0},$$

$$\mathbf{v}_{e,p,n}(\mathbf{E}) = \frac{\mathbf{W}_{e,p,n}(\mathcal{E})}{x_0/t_0},\ \tilde{\alpha}(|\mathbf{E}|) = x_0\alpha(|\mathcal{E}|),\ \tilde{\eta}(|\mathbf{E}|) = x_0\eta(|\mathcal{E}|),\ \tilde{\beta} = N_0 t_0 \beta,$$

we can obtain the following dimensionless model,

$$\begin{cases} \frac{\partial \sigma}{\partial \tau} + \nabla \cdot (\sigma \mathbf{v}_e) = (\tilde{\alpha}(|\mathbf{E}|) - \tilde{\eta}(|\mathbf{E}|))\sigma|\mathbf{v}_e| - \tilde{\beta}\sigma\rho, \\ \frac{\partial \rho}{\partial \tau} + \nabla \cdot (\rho \mathbf{v}_p) = \tilde{\alpha}(|\mathbf{E}|)\sigma|\mathbf{v}_e| - \tilde{\beta}\sigma\rho - \tilde{\beta}\rho\delta, \\ \frac{\partial \delta}{\partial \tau} + \nabla \cdot (\delta \mathbf{v}_n) = \tilde{\eta}(|\mathbf{E}|)\sigma|\mathbf{v}_e| - \tilde{\beta}\rho\delta, \\ -\nabla^2\phi = (\rho - \sigma - \delta),\ \mathbf{E} = -\nabla\phi, \end{cases} \tag{4.40}$$

in the computational domain $\Omega = (0, 0.2) \times (0, 1)$ with boundary conditions,

$$\phi(x, 0, t) = 0,\ \phi(x, 1, t) = 1,\ \frac{\partial \phi}{\partial x}(0, y, t) = \frac{\partial \phi}{\partial x}(0.2, y, t) = 0;$$

$$\nabla\sigma \cdot \mathbf{n} = \nabla\rho \cdot \mathbf{n} = \nabla\delta \cdot \mathbf{n} = 0 \text{ on } \partial\Omega.$$

In this simulation, the mesh size is chosen to be $\triangle x = \triangle y = \frac{1}{2000}$; the time step size is $\triangle t = 10^{-5}$ which corresponds to $10^{-3} ns$. Totally, there are 800,000 elements.

Firstly, we show the dynamics of electron density. Figure 4.3 shows that the first corona expands at the beginning then two new electron avalanches incept and move towards the electrodes after some time. We can clearly observe these two avalanches at 15ns. From Figure 4.4, one can observe that the upper electron avalanche keeps moving towards the anode but the lower avalanche begins to bifurcate. Later on, more and more branches forms in the lower avalanche from 25ns to 30ns as shown in Figure 4.5. Especially, from the right figure in Figure 4.5, it is shown that the electron density in the first corona becomes less and less which means the discharge in the first corona gradually terminates; meanwhile, more and more electrons gather in the two lowest branches so that two new streamer channels form there. If we track these new streamer channels, we can see from Figure 4.6 that they ceaselessly elongate and move towards the cathode with some angle.

Next, we show that the net charge density and electric field together. From Figure 4.7, we can see that there are two streamers with different polarities shortly after the beginning of discharge. The upper one is a negative streamer and the lower one is positive. These two streamers move in opposite direction but modify the background electric field in the same way: strengthening the electric field around their fronts and weakening the electric field behind them. In addition, the negative streamer has a larger area than the negative streamer. This shows the situation before the occurrence of bifurcation.

In Figure 4.8, it can be seen that the bifurcation phenomenon occurs at about 30ns. Compared with the profile at 10ns, the positive streamer is wider but shorter than the negative streamer. This change of shape is because of that the negative streamer propagates faster than the negative streamer. The modified electric field due to the positive streamer can attract electrons and negative ions so that the positive streamer develops. But the positive streamer propagates slowly, hence, there is enough time for particles to gather. After bifurcation occurs, more and more particles continue gathering around the positive streamer as shown in Figure 4.9. Then one single positive streamer splits into two new streamers. There two new

positive streamers develop and move towards the cathode, driven by the modified electric field around their heads. Moreover, the gathering of particles will enhance the recombination effect so that the positive streamer has lower charged particle density than negative streamer.

As for the negative streamer, it always moves away rapidly before plenty of particles gather around it, although it also develops. Therefore, negative streamer keeps shape and its channel is elongated during propagation. From Figure 4.10 and Figure 4.11, it can be estimated that the negative streamer propagates with velocity about $6.9 \times 10^7\ m/s$ which coincides with experimental data. Compared with the positive streamers, the negative streamer is more stable and is affected mainly by the background electric field.

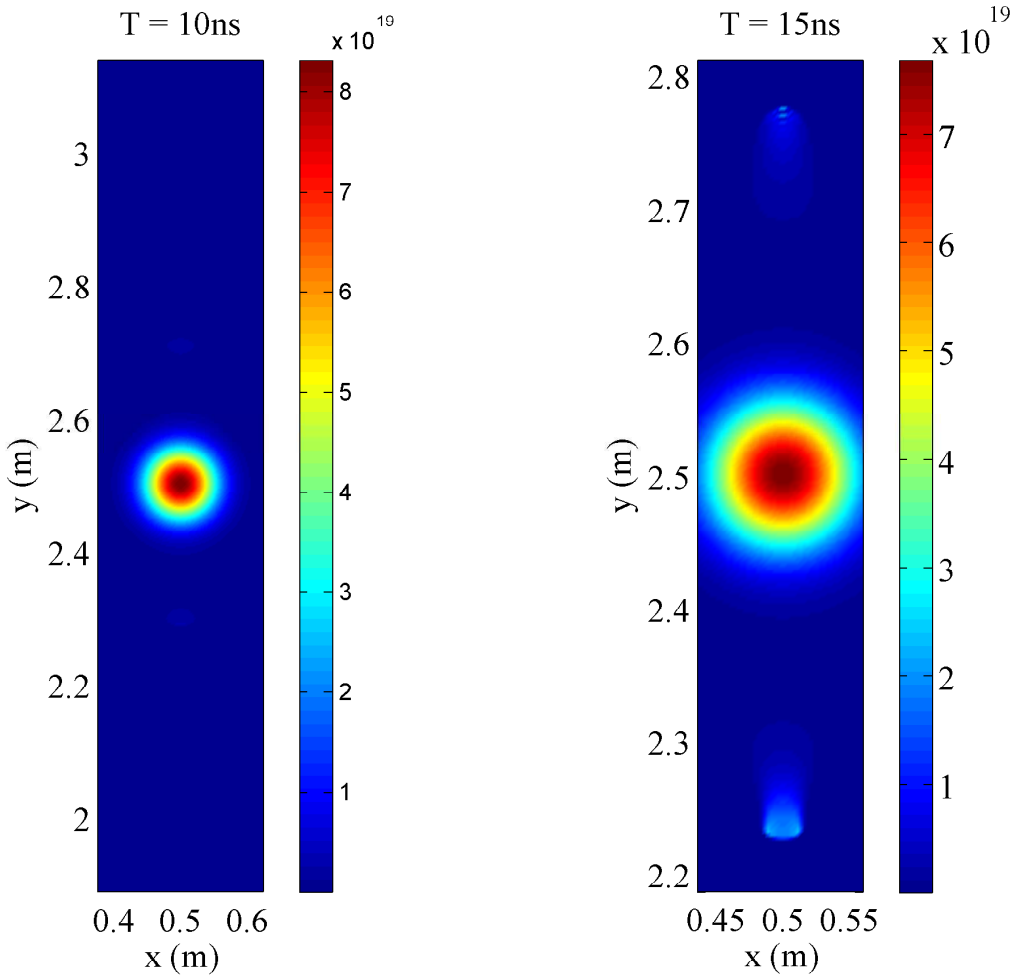

Figure 4.3: The distribution of electron density (m^{-3}) at 10ns (left) and 15ns (right).

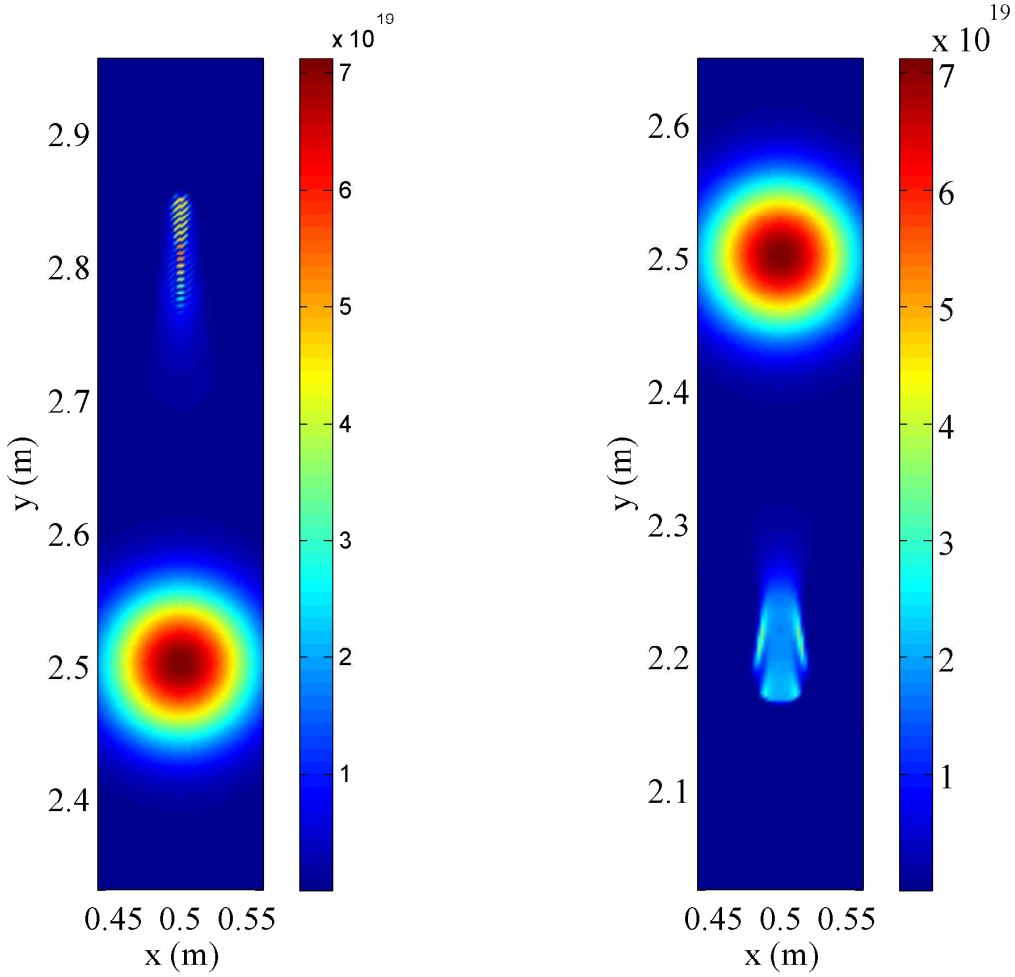

Figure 4.4: The distribution of electron density (m^{-3}) at 20ns.

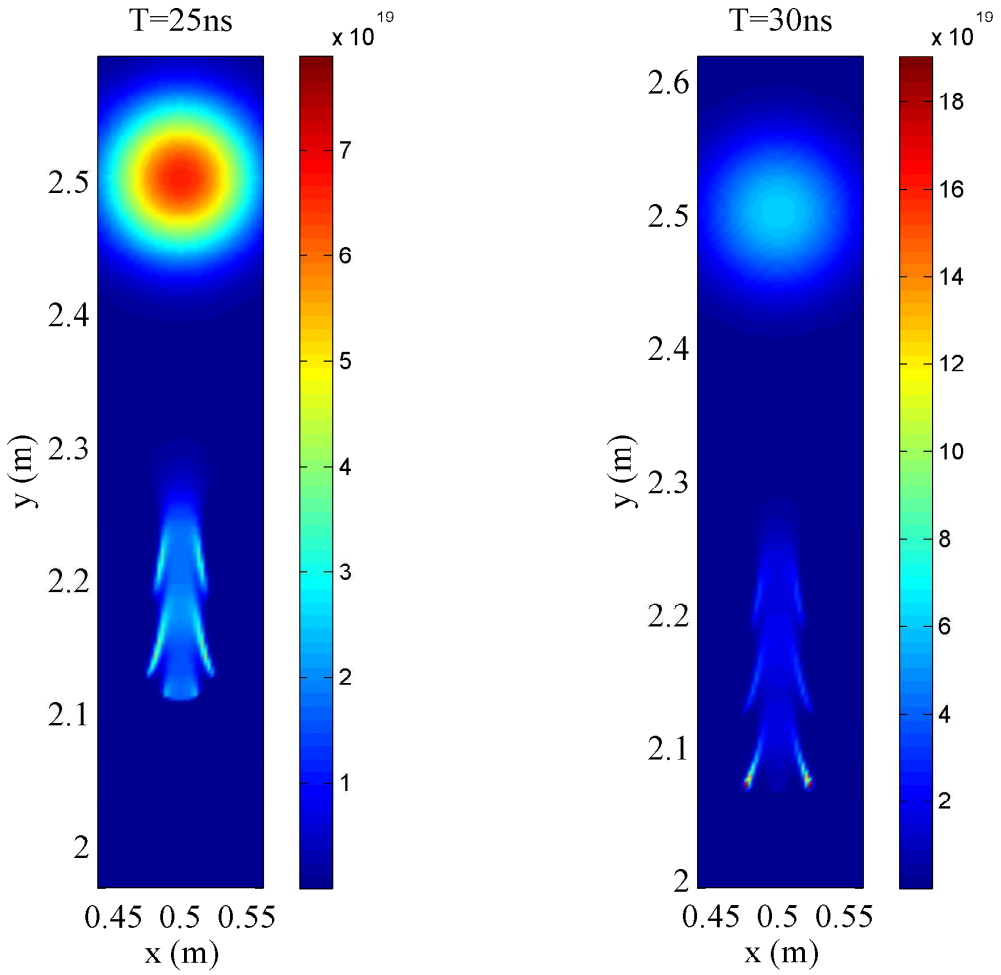

Figure 4.5: The distribution of electron density (m^{-3}) at 25ns (left) and 30ns (right).

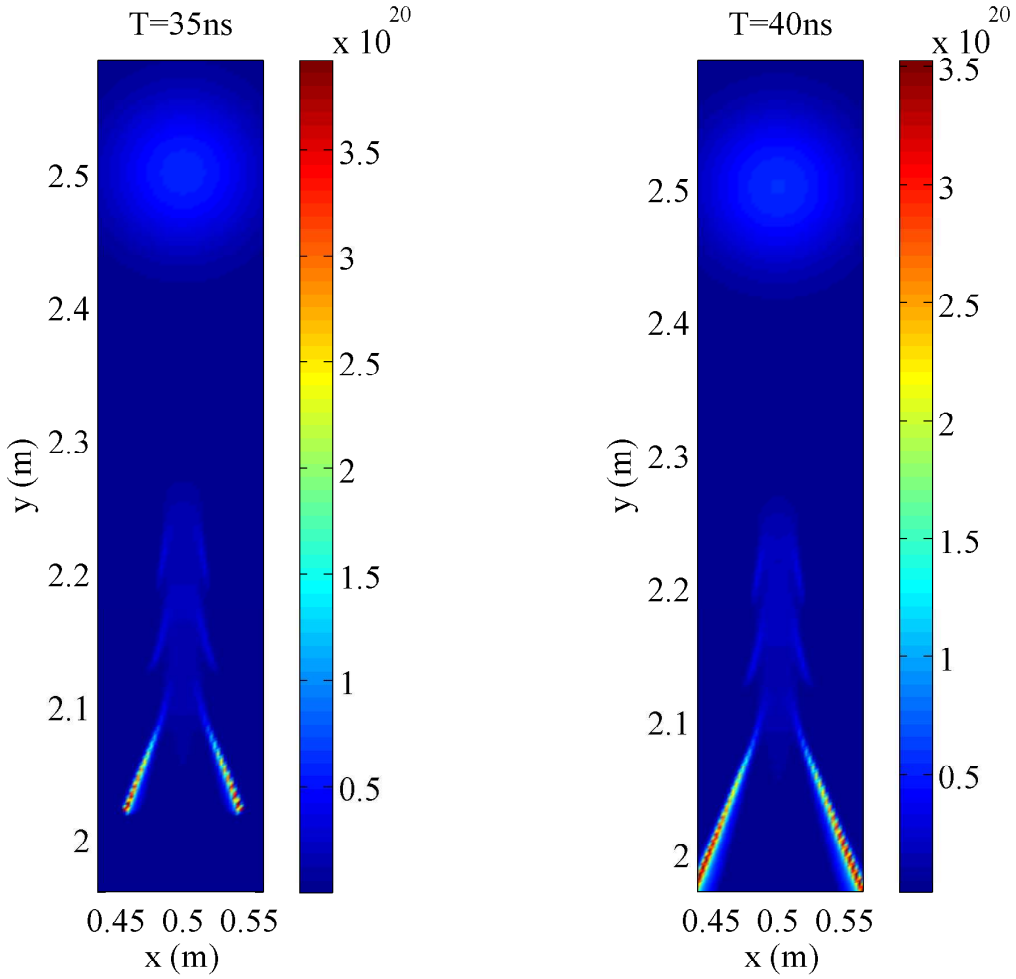

Figure 4.6: The distribution of electron density (m^{-3}) at 35ns (left) and 40ns (right).

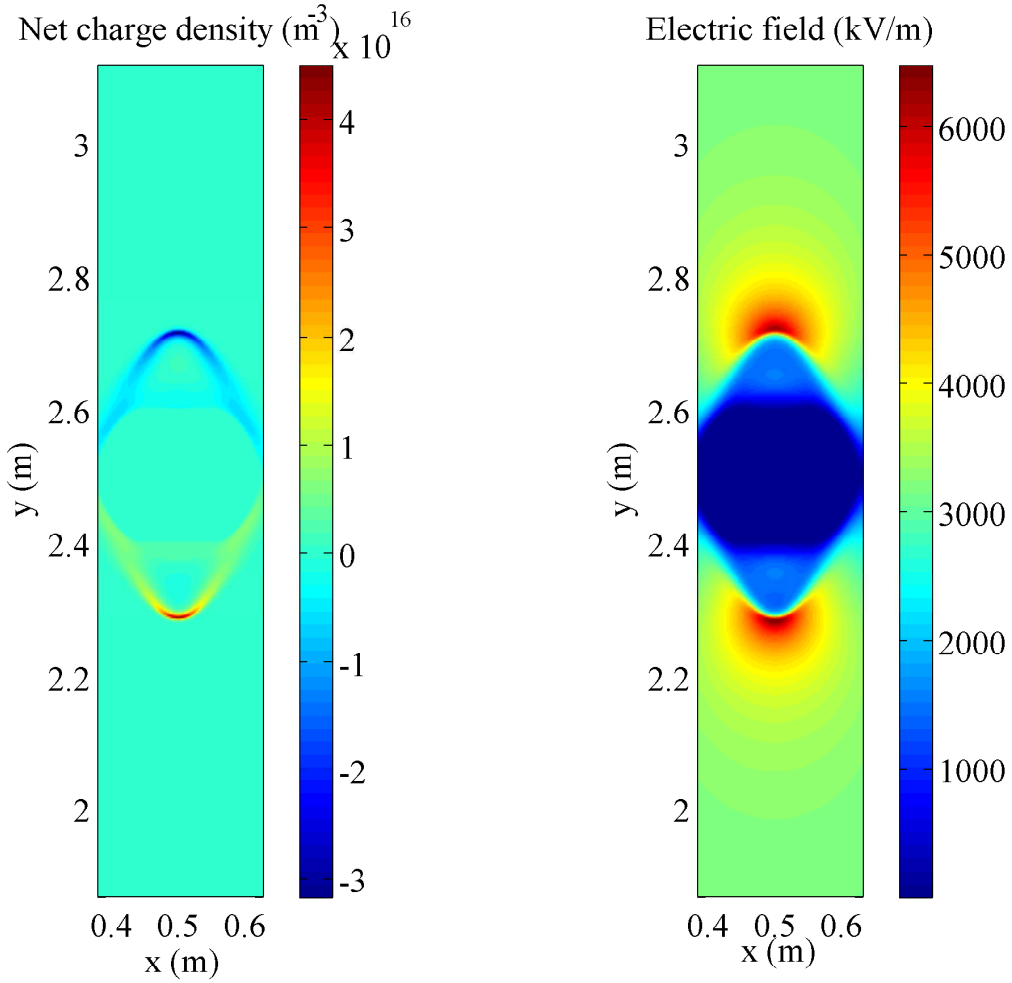

Figure 4.7: The distribution of net charge density (m^{-3}, left) and electric field $|\mathcal{E}|$ (kV/m, right) at 10ns.

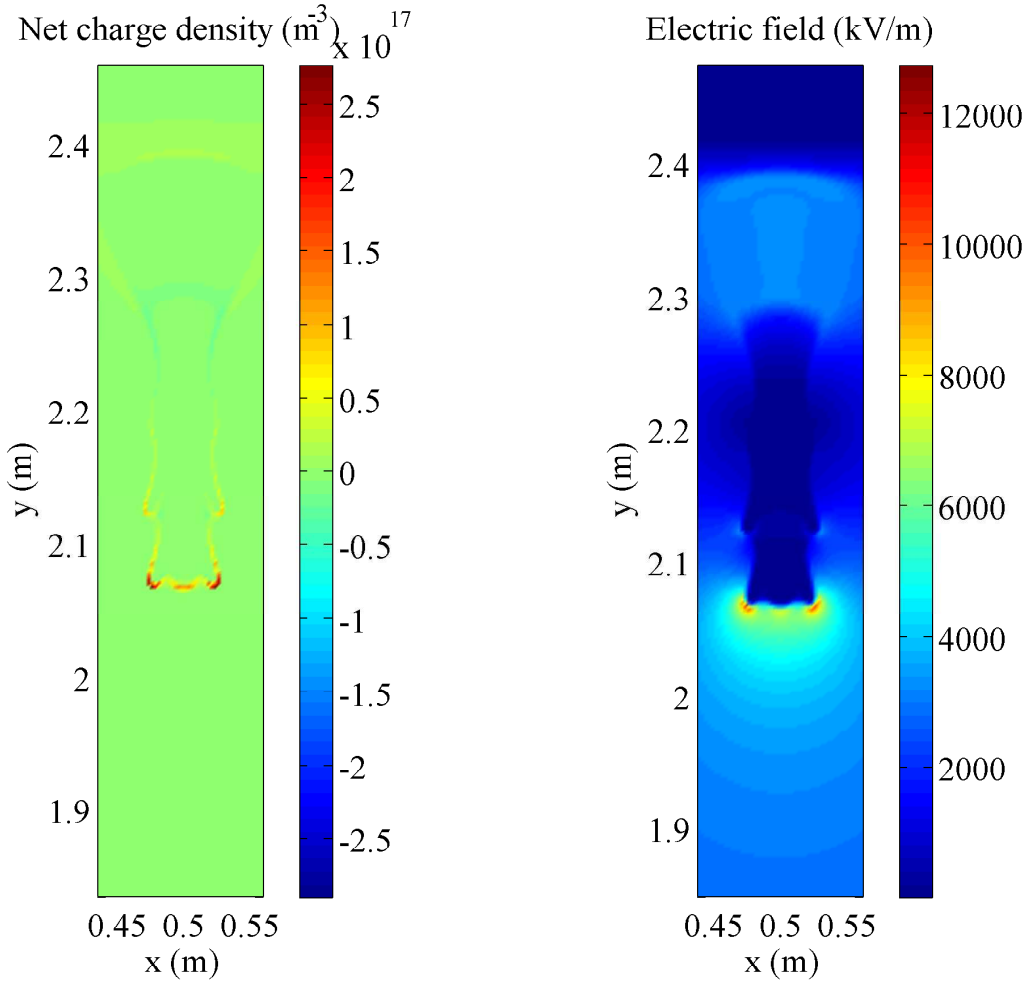

Figure 4.8: The distribution of net charge density (m^{-3}, left) and electric field $|\mathcal{E}|$ (kV/m, right) at 30ns.

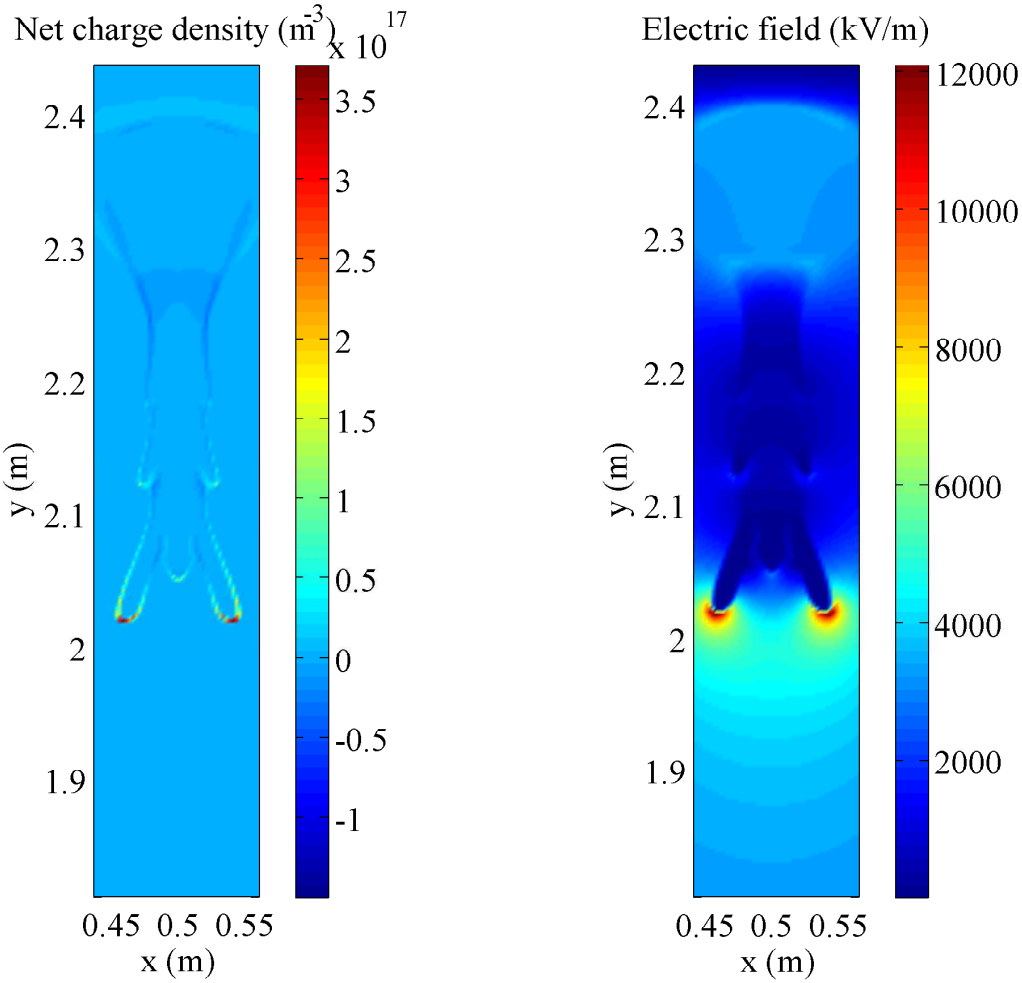

Figure 4.9: The distribution of net charge density (m^{-3}, left) and electric field $|\mathcal{E}|$ (kV/m, right) at 35ns.

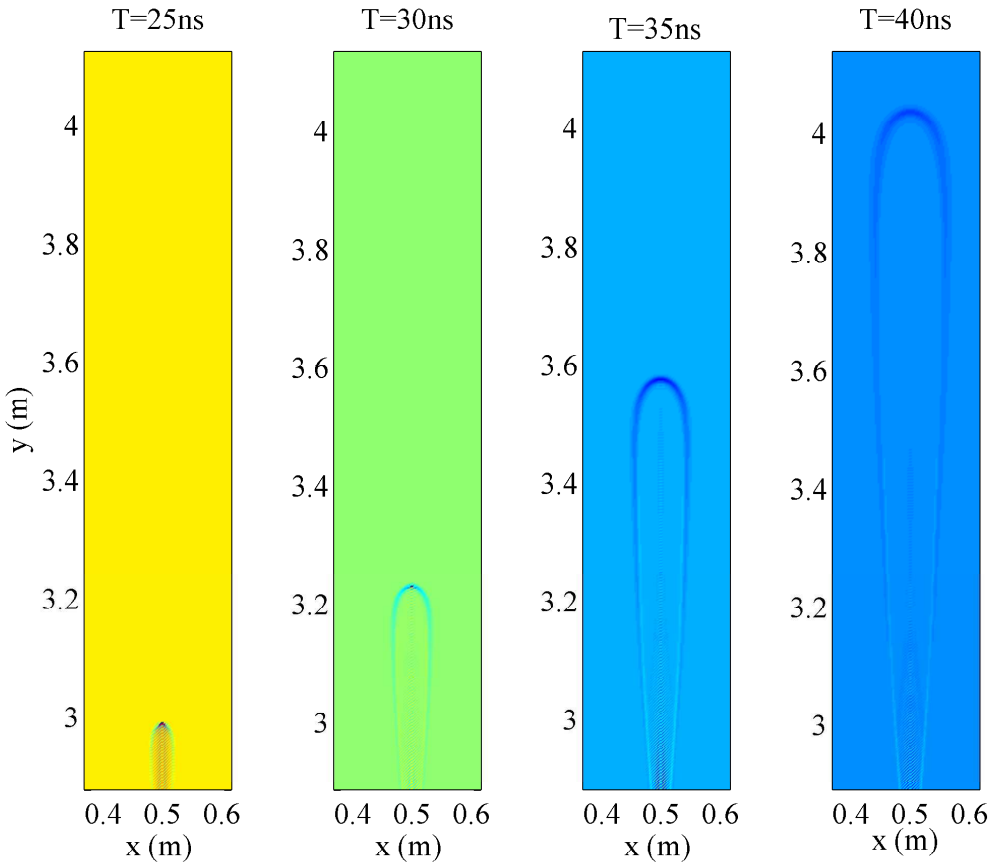

Figure 4.10: The distribution of net charge density (m^{-3}) at 25, 30, 35 and 40ns (from left to right).

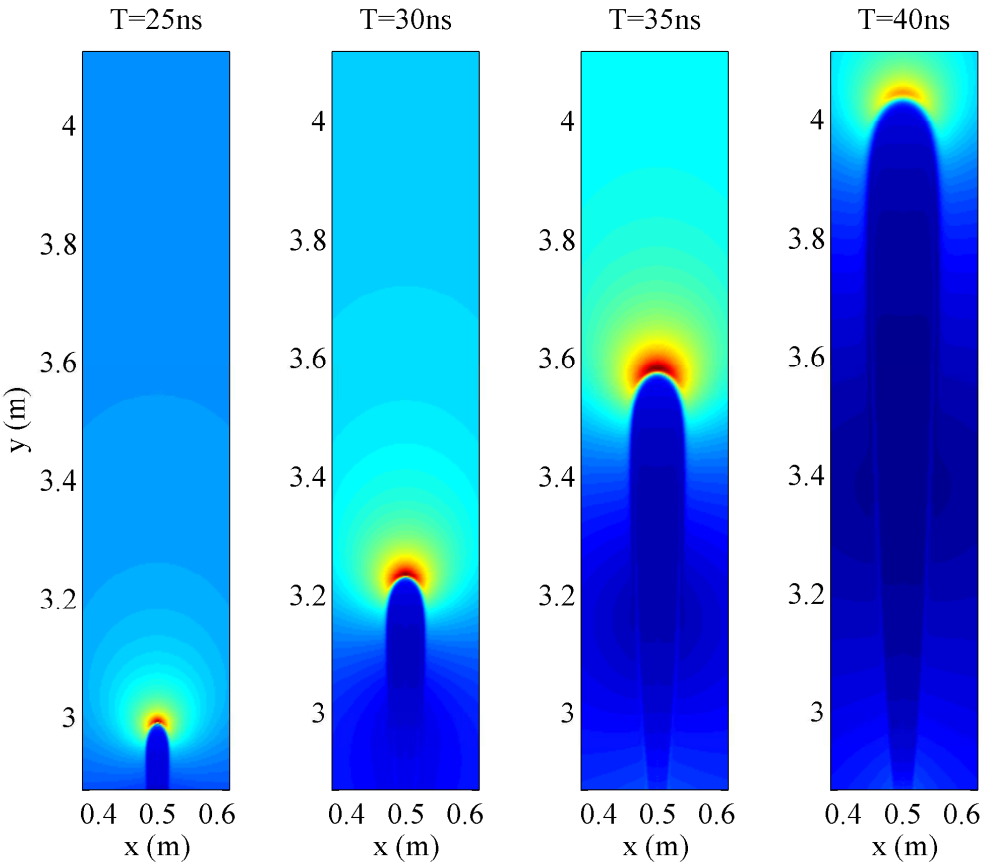

Figure 4.11: The distribution of electric field $|\mathcal{E}|$ (V/m) at 25, 30, 35 and 40ns (from left to right).

Chapter 5

Numerical Methods and Results for Quasi 3D Model

In this chapter, we will consider quasi 3D Model (1.6). To facilitate the interpretation of numerical schemes, this model is rewritten by

$$\begin{cases} \frac{\partial \sigma}{\partial t} + \frac{1}{r}\nabla \cdot (r\mu_\sigma \sigma \mathbf{E} - r\mathbb{D}\nabla\sigma) = S|\mathbf{E}|e^{K/|\mathbf{E}|}\sigma, \ (r,z) \in \Omega, t > 0; \\ \frac{\partial \rho}{\partial t} + \frac{1}{r}\nabla \cdot (r\mu_\rho \rho \mathbf{E}) = S|\mathbf{E}|e^{K/|\mathbf{E}|}\sigma, \ (r,z) \in \Omega, t > 0; \\ -\frac{1}{r}\nabla \cdot (r\nabla\phi) = \rho - \sigma, \ \mathbf{E} = -\nabla\phi, \ (r,z) \in \Omega, t > 0. \end{cases} \tag{5.1}$$

The computational domain is generally defined by

$$\Omega = \{(r,z) : 0 < r < R, \ 0 < z < f(r)\};$$

the initial and boundary conditions are posed by

$$\sigma(r,z,0) = \sigma_0(r,z), \ \rho(r,z,0) = \rho_0(r,z), \ (r,z) \in \Omega;$$

$$\frac{\partial \sigma}{\partial \mathbf{n}} = \frac{\partial \rho}{\partial \mathbf{n}} = 0 \ \text{ on } \partial\Omega;$$

$$\phi(r,0,t) = 0, \ \phi(r,f(r),t) = 1, \ \frac{\partial \phi}{\partial r}(0,z,t) = \frac{\partial \phi}{\partial r}(R,z,t) = 0.$$

Please refer to the following figure.

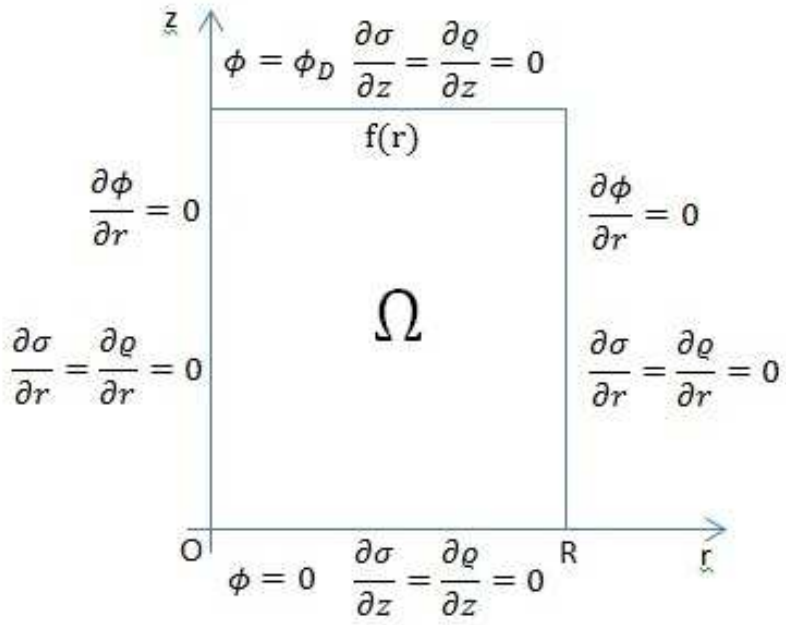

Figure 5.1: Boundary conditions for quasi 3D model.

We have pointed out in Chapter 3 that the main difficulty in this model is that it involves of the singular factor $\frac{1}{r}$. To overcome the singularity, we apply new test function rv, where v is the test function in Chapter 4, in Galerkin-type schemes. The definitions for finite element spaces and other notations are all inherited from Chapter 4.

5.1 Numerical methods for Poisson's equation

Similar with 2D model, we consider the finite difference method (FDM) and discontinuous Galerkin (DG) methods if the computational domain is a rectangle and consider DG methods, mixed finite element method (MFEM) and least-squares finite element method (LSFEM) if the geometry is complex. Suppose the computational

domain is always $\Omega = (0, R) \times (0, L_z)$ and rewrite the boundary condition on the Dirichlet boundary as

$$\phi(r, z) = \phi_D(r, z), \text{ on } \Gamma_D.$$

5.1.1 The finite difference method

In this method, the numerical solution for Poisson's equation is defined in the center of elements. Suppose there are N_r rectangles in r-direction and N_z rectangles in z-direction in a uniform mesh. Let $\triangle r = \frac{R}{N_r}$ and $\triangle z = \frac{L_z}{N_z}$. Let $r_i = (i - \frac{1}{2})\triangle r$ and $z_j = (j - \frac{1}{2})\triangle z$ be the coordinates of the center of element $K_{i,j}$. Let $\phi_{i,j}$ approximate $\phi(r_i, z_j)$, then the standard second order approximation reads,

$$-\frac{\phi^n_{i-1,j} - 2\phi^n_{i,j} + \phi^n_{i+1,j}}{(\triangle r)^2} - \frac{\phi^n_{i+1,j} - \phi^n_{i-1,j}}{2r_i\triangle r} - \frac{\phi^n_{i,j-1} - 2\phi^n_{i,j} + \phi^n_{i,j+1}}{(\triangle z)^2} = \rho^n_{i,j} - \sigma^n_{i,j}, \quad (5.2)$$

for $i = 1, 2, \cdots, N_r$ and $j = 1, 2, \cdots, N_z$, where $\rho^n_{i,j}$ and $\sigma^n_{i,j}$ are the values of ρ and σ in element centers respectively. The boundary conditions are strongly imposed by introducing ghost cells. If the boundary condition is imposed by Dirichlet type, then a linear interpolation will be used. If the boundary condition is given by Neumann type, then we use reflection.

$$\phi^n_{0,j} = \phi^n_{1,j}, \ \phi^n_{N_r+1,j} = \phi^n_{N_r,j}, \ j = 1, 2, \cdots, N_z;$$

$$\phi^n_{i,0} = 2\phi_D(r_i, 0) - \phi^n_{i,1}, \ \phi^n_{i,N_z+1} = 2\phi_D(r_i, L_z) - \phi^n_{i,N_z}, \ i = 1, 2, \cdots, N_r.$$

Next, we need to define the numerical approximation of $\mathbf{E}^n$. Since the geometry is very simple, we can directly define $\mathbf{E}^n \cdot \mathbf{n}$ along the edge of any element $K_{i,j}$.

$$\begin{aligned}
&\text{On the top edge: } \mathbf{E}^n \cdot \mathbf{n} = \frac{\phi^n_{i,j} - \phi^n_{i,j+1}}{\triangle z};\\
&\text{on the bottom edge: } \mathbf{E}^n \cdot \mathbf{n} = \frac{\phi^n_{i,j-1} - \phi^n_{i,j}}{\triangle z};\\
&\text{on the left edge: } \mathbf{E}^n \cdot \mathbf{n} = \frac{\phi^n_{i-1,j} - \phi^n_{i,j}}{\triangle r};\\
&\text{on the right edge: } \mathbf{E}^n \cdot \mathbf{n} = \frac{\phi^n_{i,j} - \phi^n_{i+1,j}}{\triangle r}.
\end{aligned} \quad (5.3)$$

And we define $\mathbf{E}^n$ in the interior as

$$\mathbf{E}^n = \left(\frac{\phi^n_{i-1,j} - \phi^n_{i+1,j}}{2\triangle r}, \frac{\phi^n_{i,j-1} - \phi^n_{i,j+1}}{2\triangle z} \right)^T. \tag{5.4}$$

5.1.2 The discontinuous Galerkin methods

We still follow the ideas in [6] to derive the DG scheme for the Poisson's equation in quasi 3D model. Firstly, we reformulate the equation by a first order system,

$$\begin{cases} \frac{1}{r}\nabla \cdot (r\mathbf{E}) = \rho^n - \sigma^n, \\ -\nabla\phi = \mathbf{E}. \end{cases} \tag{5.5}$$

Multiplying the first and second equation by new test functions rv and $r\mathbf{F}$ respectively, integration over one single element K and using integration by parts, we can obtain

$$\int_{\partial K} r(\mathbf{E}\cdot\mathbf{n}_K)v - \int_K r\mathbf{E}\cdot\nabla v = \int_K (\rho^n - \sigma^n)rv, \tag{5.6}$$

and

$$-\int_{\partial K} r\phi(\mathbf{F}\cdot\mathbf{n}_K) + \int_K \phi\nabla\cdot(r\mathbf{F}) = \int_K \mathbf{E}\cdot(r\mathbf{F}), \tag{5.7}$$

where $\mathbf{n}_K$ is the unit outer normal vector of the boundary of element K. Replacing $\mathbf{E}$ and ϕ in the edge integrations in (5.6) and (5.7) by numerical fluxes $\hat{\mathbf{E}}_K$ and $\hat{\phi}_K$ respectively, we consider a general weak formulation: to find $\phi^h \in V_k$ and $\mathbf{E}^h \in (V_k)^2$ such that for all element K in the partition $\mathcal{E}_h$, we have

$$\int_{\partial K} r(\hat{\mathbf{E}}_K\cdot\mathbf{n}_K)v - \int_K r\mathbf{E}^h\cdot\nabla v = \int_K (\rho^n - \sigma^n)rv,\ \forall v \in V_k, \tag{5.8}$$

and

$$-\int_{\partial K} r\hat{\phi}_K(\mathbf{F}\cdot\mathbf{n}_K) + \int_K \phi^h\nabla\cdot(r\mathbf{F}) = \int_K \mathbf{E}^h\cdot(r\mathbf{F}),\ \forall\mathbf{F} \in (V_k)^2. \tag{5.9}$$

Adding over all elements for (5.8) and (5.9), we get

$$\sum_K \int_{\partial K} r(\hat{\mathbf{E}}_K\cdot\mathbf{n}_K)v - \sum_K \int_K r\mathbf{E}^h\cdot\nabla v = \int_\Omega (\rho^n - \sigma^n)rv,\ \forall v \in V_k, \tag{5.10}$$

and

$$-\sum_K \int_{\partial K} r\hat{\phi}_K(\mathbf{F}\cdot\mathbf{n}_K) + \sum_K \int_K \phi^h \nabla\cdot(r\mathbf{F}) = \int_\Omega \mathbf{E}^h\cdot(r\mathbf{F}),\ \forall \mathbf{F}\in(V_k)^2. \quad (5.11)$$

It is easy to show that

$$\sum_K \int_{\partial K} ra\mathbf{B}\cdot\mathbf{n}_K = \sum_{e\in\Gamma_I}\int_e r(\{a\}[\mathbf{B}] + [a]\cdot\{\mathbf{B}\}) + \sum_{e\in\Gamma_D\cup\Gamma_N}\int_e r\{a\}[\mathbf{B}], \quad (5.12)$$

if the scalar function a and vector-valued function $\mathbf{B}$ both belongs to $C(\bar{K})\cap C^1(K)$ for all elements K. Here the notations $\Gamma_I, \Gamma_D, \Gamma_N$ and definitions for jump $[\cdot]$ and average $\{\cdot\}$ are all inherited from Chapter 4.

If we set $a = v, \mathbf{B} = \hat{\mathbf{E}}_K$ and $a = \hat{\phi}_K, B = \mathbf{F}$ respectively in (5.12), and insert the results into (5.10) and (5.11), then we can find that

$$\begin{aligned} &\sum_{e\in\Gamma_I}\int_e r(\{v\}[\hat{\mathbf{E}}_K] + [v]\cdot\{\hat{\mathbf{E}}_K\}) + \sum_{e\in\Gamma_D\cup\Gamma_N}\int_e r\{v\}[\hat{\mathbf{E}}_K] - \sum_K\int_K r\mathbf{E}^h\cdot\nabla v \\ =\ &\int_\Omega(\rho^n-\sigma^n)rv,\ \forall v\in V_k, \end{aligned} \quad (5.13)$$

and

$$\begin{aligned} &-\sum_{e\in\Gamma_I}\int_e r(\{\hat{\phi}_K\}[\mathbf{F}] + [\hat{\phi}_K]\cdot\{\mathbf{F}\}) - \sum_{e\in\Gamma_D\cup\Gamma_N}\int_e r\{\hat{\phi}_K\}[\mathbf{F}] + \sum_K\int_K \phi^h\nabla\cdot(r\mathbf{F}) \\ =\ &\int_\Omega \mathbf{E}^h\cdot(r\mathbf{F}),\ \forall\mathbf{F}\in(V_k)^2. \end{aligned} \quad (5.14)$$

Next, by setting $a = \phi^h, \mathbf{B} = \mathbf{F}$ in (5.12), using (5.14) and noticing

$$\sum_K\int_{\partial K} ra\mathbf{B}\cdot\mathbf{n}_K = \sum_K\int_K \nabla\cdot(ra\mathbf{B}),$$

we can obtain

$$\begin{aligned} &\sum_{e\in\Gamma_I}\int_e r(\{\phi^h\}[\mathbf{F}] + [\phi^h]\cdot\{\mathbf{F}\}) + \sum_{e\in\Gamma_D\cup\Gamma_N}\int_e r\{\phi^h\}[\mathbf{F}] \\ =\ &\sum_K\int_K\nabla\cdot(r\phi^h\mathbf{F}) = \sum_K\int_K(\phi^h\nabla\cdot(r\mathbf{F}) + r\mathbf{F}\cdot\nabla\phi^h) \\ =\ &\sum_K\int_K(\mathbf{E}^h+\nabla\phi^h)\cdot(r\mathbf{F}) + \sum_{e\in\Gamma_I}\int_e r(\{\hat{\phi}_K\}[\mathbf{F}] + [\hat{\phi}_K]\cdot\{\mathbf{F}\}) + \sum_{e\in\Gamma_D\cup\Gamma_N}\int_e r\{\hat{\phi}_K\}[\mathbf{F}], \end{aligned}$$

or equivalently,

$$\sum_K \int_K (\mathbf{E}^h + \nabla\phi^h)\cdot(r\mathbf{F}) = \sum_{e\in\Gamma_I}\int_e r(\{\phi^h - \hat{\phi}_K\}[\mathbf{F}] + [\phi^h - \hat{\phi}_K]\cdot\{\mathbf{F}\}) + \sum_{e\in\Gamma_D\cup\Gamma_N}\int_e r\{\phi^h - \hat{\phi}_K\}[\mathbf{F}]. \tag{5.15}$$

If we take $\mathbf{F} = \nabla v$ in each element in (5.15) and combine the resulting equation with (5.13), we can obtain

$$\begin{aligned}
&\sum_K \int_K r\nabla\phi^h\cdot\nabla v \\
-\ &\sum_{e\in\Gamma_I}\int_e r(\{\phi^h - \hat{\phi}_K\}[\nabla v] + [\phi^h - \hat{\phi}_K]\cdot\{\nabla v\}) - \sum_{e\in\Gamma_D\cup\Gamma_N}\int_e r\{\phi^h - \hat{\phi}_K\}[\nabla v] \\
+\ &\sum_{e\in\Gamma_I}\int_e r(\{v\}[\hat{\mathbf{E}}_K] + [v]\cdot\{\hat{\mathbf{E}}_K\}) + \sum_{e\in\Gamma_D\cup\Gamma_N}\int_e r\{v\}[\hat{\mathbf{E}}_K] \\
=\ &\int_\Omega (\rho^n - \sigma^n) rv,\ \forall v\in V_k.
\end{aligned} \tag{5.16}$$

We define the numerical fluxes $\hat{\phi}_K$ and $\hat{\mathbf{E}}_K$ as follows:

$$\begin{cases}
\hat{\phi}_K = \{\phi^h\} + \frac{1+\epsilon}{2}[\phi^h]\cdot\mathbf{n}_K, & \text{if } \partial K \supset e \in \Gamma_I, \\
\hat{\phi}_K = \phi^h, & \text{if } \partial K \supset e \in \Gamma_N, \\
\hat{\phi}_K = \phi^h + \epsilon(\phi^h - \phi_D), & \text{if } \partial K \supset e \in \Gamma_D,
\end{cases} \tag{5.17}$$

where ϵ is any real number; and

$$\begin{cases}
\hat{\mathbf{E}}_K = -\{\nabla\phi^h\} + \frac{\alpha_e}{|e|^\beta}[\phi^h], & \text{if } \partial K \supset e \in \Gamma_I, \\
\hat{\mathbf{E}}_K = -\nabla\phi(r,z), & \text{if } \partial K \supset e \in \Gamma_N, \\
\hat{\mathbf{E}}_K = -\nabla\phi^h + \frac{\alpha_e}{|e|^\beta}(\phi^h - \phi_D(r,z))\mathbf{n}_K, & \text{if } \partial K \supset e \in \Gamma_D,
\end{cases} \tag{5.18}$$

where $\alpha_e \geq 0$, $\beta > 0$ and $|e|$ is the length of edge. From these definitions, one can directly prove that

$$\{\phi^h - \hat{\phi}_K\} = 0,\ [\phi^h - \hat{\phi}_K] = -\epsilon[\phi^h],$$

and

$$\{\hat{\mathbf{E}}_K\} = -\{\nabla\phi^h\} + \frac{\alpha_e}{|e|^\beta}[\phi^h],\ [\hat{\mathbf{E}}_K] = 0,$$

along the interior edges.

Thus, by inserting the numerical fluxes into (5.16) and using the boundary conditions, we can find that

$$\begin{aligned}
&\sum_K \int_K r\nabla\phi^h \cdot \nabla v \\
+ &\sum_{e\in\Gamma_I} \int_e r\left(-\{\nabla\phi^h\} + \frac{\alpha_e}{|e|^\beta}[\phi^h]\right)\cdot[v] + \sum_{e\in\Gamma_D}\int_e r\left(-\nabla\phi^h\cdot\mathbf{n} + \frac{\alpha_e}{|e|^\beta}(\phi^h-\phi_D)\right)v \\
+ &\epsilon\sum_{e\in\Gamma_I}\int_e r\{\nabla v\}\cdot[\phi^h] + \epsilon\sum_{e\in\Gamma_D}\int_e r(\phi^h-\phi_D)(\nabla v\cdot\mathbf{n}) \\
= &\int_\Omega (\rho^n-\sigma^n)rv,\ \forall v\in V_k.
\end{aligned}$$

Therefore, if we define the symmetric bilinear form $B_\epsilon : V_k \times V_k \to \mathbb{R}$,

$$\begin{aligned}
B_\epsilon(u,v) &= \sum_K\int_K r\nabla u\cdot\nabla v - \sum_{e\in\Gamma_I\cup\Gamma_D}\int_e r\,\{\nabla u\}\cdot[v] \\
&+ \epsilon\sum_{e\in\Gamma_I\cup\Gamma_D}\int_e r\,\{\nabla v\}\cdot[u] + \sum_{e\in\Gamma_I\cup\Gamma_D}\frac{\alpha_e}{|e|^\beta}\int_e r[u]\cdot[v],
\end{aligned} \tag{5.19}$$

and linear form $L : V_k \to \mathbb{R}$,

$$L(v) = \int_\Omega(\rho^n-\sigma^n)rv + \sum_{e\in\Gamma_D}\int_e r\left(\epsilon\nabla v\cdot\mathbf{n} + \frac{\alpha_e}{|e|^\beta}v\right)\phi_D, \tag{5.20}$$

then the DG method is to find $\phi^h \in V_k$ such that

$$B_\epsilon(\phi^h, v) = L(v),\ \forall v\in V_k. \tag{5.21}$$

The DG method has different properties depending on the choice of parameters ϵ, α and β. Here we choose $\epsilon = -1$ to form a symmetric linear system which leads to symmetric interior penalty Galerkin method (SIPG) and choose

$$\beta = 1,\ \alpha_e = \begin{cases} 3k(k+1), & \text{if } e\in\Gamma_I, \\ 6k(k+1), & \text{if } e\in\Gamma_D\cup\Gamma_N, \end{cases}$$

to ensure optimal convergence.

The numerical approximation of electric field is derived from ϕ^h by the following way. In each element,

$$\mathbf{E}^n = -\nabla\phi^h. \tag{5.22}$$

Along the edge, since ϕ^h is allowed to be discontinuous, there is a penalty term in the above scheme,

$$\mathbf{E}^n = \begin{cases} -\{\nabla\phi^h\} + \frac{\alpha_e}{|e|^\beta}[\phi^h], & \text{if } e \in \Gamma_I, \\ -\nabla\phi^h, & \text{if } e \in \Gamma_N, \\ -\nabla\phi^h + \frac{\alpha_e}{|e|^\beta}(\phi^h - \phi_D)\mathbf{n}, & \text{if } e \in \Gamma_D, \end{cases} \tag{5.23}$$

which is almost the same with the numerical flux $\hat{\mathbf{E}}$.

Remark 1. Similar with the traditional DG scheme in previous chapter, the jump in both artificial terms (symmetric and penalty terms) is used for numerical solution. Therefore, the artificial terms will still not affect the convergence of numerical solution for fixed values of artificial parameters. Besides, the requirement for optimal convergence is the same as that in traditional DG scheme.

Remark 2. Due to some of our numerical studies not shown in this thesis, there seems to be still some critical values for artificial parameters α_e and β for optimal convergence rate when ϵ is fixed (especially for NIPG and IIPG). More careful studies can be done to solve this problem.

5.1.3 The mixed finite element method

This method also reformulates the Poisson's equation by a first order differential equation system,

$$\begin{cases} \frac{1}{r}\nabla\cdot(r\mathbf{E}) = \rho^n - \sigma^n, \\ -\nabla\phi = \mathbf{E}. \end{cases} \tag{5.24}$$

We still call ϕ the scalar variable and $\mathbf{E}$ the flux variable and use the definitions of subspaces introduced in the previous chapter.

By multiplying the first and second equation with $r\psi$ and $r\mathbf{v}$ respectively, applying integration by parts to the second equation and using the boundary conditions, the MFEM is to find $(\phi^h, \mathbf{E}^h) \in W_S^{mfem} \times W_F^{mfem}$ such that

$$\begin{cases} \int_\Omega \mathbf{E}^h \cdot (r\mathbf{v}) - \int_\Omega \phi^h [\nabla \cdot (r\mathbf{v})] = -\int_{\Gamma_D} r\phi_D(\mathbf{v}\cdot\mathbf{n}), & \forall \mathbf{v} \in W_F^{mfem}, \\ -\int_\Omega \psi[\nabla \cdot (r\mathbf{E}^h)] = -\int_\Omega (\rho^n - \sigma^n) r\psi, & \forall \psi \in W_S^{mfem}, \end{cases} \tag{5.25}$$

where the finite element spaces W_F^{mfem} and W_S^{mfem} are defined by (4.15) and (4.16) respectively.

Since $\mathbf{E}^h \cdot \mathbf{n}$ is continuous across the edges by the definition of subspace. Thus, the approximate electric field is naturally chosen as $\mathbf{E}^n = \mathbf{E}^h$.

5.1.4 The least-squares finite element method

The LSFEM starts from (5.24) as well. But the difference is that we want to minimize a functional on $H_D^1 \times H_N(\Omega, div)$,

$$J(\phi, \mathbf{E}) = ||\nabla \cdot (r\mathbf{E}) - r(\rho^n - \sigma^n)||^2_{L^2(\Omega;r)} + ||\mathbf{E} + \nabla\phi||^2_{\mathbf{L}^2(\Omega;r)},$$

where the weighted L^2- and $\mathbf{L}^2-$ norm are defined by

$$||f||_{L^2(\Omega;r)} = \left(\int_\Omega r f^2\right)^{1/2},$$

and

$$||\mathbf{f}||_{\mathbf{L}^2(\Omega;r)} = \left(\int_\Omega r|\mathbf{f}|^2\right)^{1/2}.$$

The LSFEM is to find $(\phi^h, \mathbf{E}^h) \in W_S^{lsfem} \times W_F^{lsfem}$ such that

$$B[(\phi^h, \mathbf{E}^h), (\psi, \mathbf{v})] = L(\mathbf{v}),\ \forall (\psi, \mathbf{v}) \in (W_k^0 \times W_F^{lsfem}), \tag{5.26}$$

where the finite element spaces W_S^{lsfem} and W_F^{lsfem} are defined by (4.18) and (4.19) respectively; the bilinear form B and linear functional L are derived from the variation of the above functional $J(\phi, \mathbf{E})$,

$$B[(\phi, \mathbf{E}), (\psi, \mathbf{v})] = \int_\Omega r[\nabla \cdot (r\mathbf{E})][\nabla \cdot (r\mathbf{v})] + \int_\Omega r\left(\mathbf{E} + \nabla\phi\right) \cdot \left(\mathbf{v} + \nabla\psi\right), \tag{5.27}$$

and

$$L(\mathbf{v}) = \int_\Omega r^2[\nabla \cdot (r\mathbf{v})](\rho^n - \sigma^n). \tag{5.28}$$

Since the flux variable $\mathbf{E}^h$ is continuous in this method, then $\mathbf{E}^h \cdot \mathbf{n}$ is automatically continuous along the edges. Thus, the approximate electric field is naturally chosen as $\mathbf{E}^n = \mathbf{E}^h$.

5.2 Numerical method for continuity equations

5.2.1 The Oden-Babuška-Baumann DG method

In this method, firstly, the diffusion term $-\frac{1}{r}\nabla\cdot(r\mathbb{D}\nabla\sigma)$ is discretized by the bilinear form (5.19) with symmetric parameter $\epsilon = 1$ and penalty parameter $\alpha_e = 0$. Because of the homogeneous Neumann boundary condition, we only consider interior edges:

$$B(u,v) = \sum_{i=1}^{N}\int_{K_i} r\mathbb{D}\nabla u\cdot\nabla v - \sum_{e\in\Gamma_I}\int_e r\,\{\mathbb{D}\nabla u\}\cdot[v] + \sum_{e\in\Gamma_I}\int_e r\,\{\mathbb{D}\nabla v\}\cdot[u]. \tag{5.29}$$

Secondly, the convection terms $\frac{1}{r}\nabla\cdot(r\mu_P P\mathbf{E}$ for $P=\sigma$ or ρ is discretized by

$$\begin{aligned} C(P,v;\mathbf{E}) &= -\sum_{i=1}^{N}\int_{K_i} rP(\mu_P\mathbf{E}\cdot\nabla v) + \sum_{e\in\Gamma_I}\int_e r\widehat{P}(\mu_P\mathbf{E}\cdot[v]) \\ &+ \sum_{e\in\Gamma_N}\int_e rP(\mu_P\mathbf{E}\cdot\mathbf{n})v, \end{aligned} \tag{5.30}$$

with numerical flux

$$\widehat{P} = \begin{cases} P_i, & \text{if } \mu_P\mathbf{E}\cdot\mathbf{n}_i \geq 0, \\ P_j, & \text{if } \mu_P\mathbf{E}\cdot\mathbf{n}_i < 0, \end{cases}$$

for any interior edge $e = K_i \cap K_j$. Finally, the source term $S|\mathbf{E}|e^{K/|\mathbf{E}|}\sigma$ is still discretized by a linear form,

$$L(\sigma,v;\mathbf{E}) = \int_\Omega S|\mathbf{E}|e^{K/|\mathbf{E}|}\sigma rv. \tag{5.31}$$

Therefore, OBBDG method is to find $\sigma^h(t), \rho^h(t) \in V_k$ such that

$$\int_\Omega(\sigma^h(0)-\sigma_0)rv = \int_\Omega(\rho^h(0)-\rho_0)rv = 0,\ \forall v\in V_k; \tag{5.32}$$

and

$$\begin{aligned}
&\int_\Omega \partial_t \sigma^h r v + C(\sigma^h(t), v; \mathbf{E}(t)) + B(\sigma^h(t), v) = L(\sigma^h(t), v; \mathbf{E}(t)),\ \forall v \in V_k, \\
&\int_\Omega \partial_t \rho^h r v + C(\rho^h(t), v; \mathbf{E}(t)) = L(\sigma^h(t), v; \mathbf{E}(t)),\ \forall v \in V_k.
\end{aligned} \tag{5.33}$$

5.2.2 The slope limiter

As pointed out in Chapter 3, the slope limiter for quasi 3D model is slightly different from 2D slope limiter due to the $\frac{1}{r}$ singularity.

For rectangular mesh, one more step needs to be add into the slope limiter such that the cell average can be preserved. Suppose that the solution in the element $K_{i,j} = [r_i - \triangle r/2, r_i + \triangle r/2] \times [z_j - \triangle z/2, z_j + \triangle z/2]$ ($\triangle r$ and $\triangle z$ are mesh sizes) by

$$U_{i,j} = \sum_{p,q=0}^{p+q=k} u_{i,j}^{p,q} \phi_p(\xi) \psi_q(\eta), \tag{5.34}$$

where $\xi = \frac{r - r_i}{\triangle r/2}$, $\eta = \frac{z - z_j}{\triangle z/2}$. By using the 2D slope limiter, we end up with

$$\tilde{U}_{i,j} = u_{i,j}^{0,0} + \sum_{p^2+q^2>0}^{p+q=k} \tilde{u}_{i,j}^{p,q} \phi_p(\xi) \psi_q(\eta),$$

then we reconstruct $u_{i,j}^{0,0}$ by $\tilde{u}_{i,j}^{0,0}$ such that

$$\frac{1}{|K_{i,j}|} \int_{K_{i,j}} \left(\tilde{u}_{i,j}^{0,0} + \sum_{p^2+q^2>0}^{p+q=k} \tilde{u}_{i,j}^{p,q} \phi_p(\xi) \psi_q(\eta) \right) r dr dz = \frac{1}{|K_{i,j}|} \int_{K_{i,j}} U_{i,j} r dr dz. \tag{5.35}$$

For triangular mesh, the integrals for seeking reconstructed polynomials (i.e., (4.34)) should be changed by

$$\frac{1}{|K_j|} \int_{K_j} L_{i_1}(r - r_i, z - z_i) r dr dz = \frac{1}{|K_j|} \int_{K_j} u_j(r - r_j, z - z_j) r dr dz, \tag{5.36}$$

where the cell average in both rectangular case and triangular case should be weighted average,

$$|K_j| = \int_{K_j} 1 \cdot r dr dz.$$

5.3 Numerical tests and comparisons

Test 1. Rectangular mesh.

Consider Model (1.6) on a rectangular domain $\Omega = [0,1] \times [0,1.5]$ with toy parameters: $S = 1000$, $K = -5$, $\mu_\sigma = -1$, $\mu_\rho = 0.5$, $\mathbb{D} = 10^{-4}\mathbf{I}$. The background electric field is given as $\mathbf{E}|_{t=0} = (0,-1)^T$. The initial data of continuity equations is

$$\sigma|_{t=0} = \rho|_{t=0} = \exp\{-25r^2 - 100(z-0.5)^2\}.$$

The terminal time is set to be $T = 0.5$. The 'exact' solutions are numerically defined by using very fine mesh, namely $h = \frac{1}{128}$, and tiny time step size $\tau = 10^{-4}$. In order to compare the convergence rate in space for each coupled method, the time step is chosen as small enough. The results from Tables 5.1 - 5.3 indicate that FDM+OBBDG and SIPG+OBBDG can both be used to simulate the streamer propagation since they are both convergent. Besides, the convergence rate for particles in SIPG+OBBDG method is more regular than that in FDM+OBBDG method.

		$h_0 = \frac{1}{8}$	$h_0/2$	$h_0/2^2$	$h_0/2^3$
FDM	error	0.0128	0.0038	7.1756E-4	3.9337E-4
+OBBDG	rate	-	1.7430	2.4104	0.8672
SIPG	error	0.0112	0.0035	9.8836E-4	2.6910E-4
+OBBDG	rate	-	1.6855	1.8163	1.8769

Table 5.1: Error and convergence rate for σ in quasi 3D comparison based on rectangular mesh.

Test 2. Triangular mesh.

Before testing and comparing different methods, we would like to review the performance of those methods in 2D model. It is concluded that RT_0 MFEM is less accurate than the others and BDM_1 MFEM and LSFEM requires more memory

		$h_0 = \frac{1}{8}$	$h_0/2$	$h_0/2^2$	$h_0/2^3$
FDM	error	0.0100	0.0020	3.5590E-4	1.9363E-4
+OBBDG	rate	-	2.3120	2.4959	0.8782
SIPG	error	0.0090	0.0027	0.0012	3.7448E-4
+OBBDG	rate	-	1.7419	1.1738	1.6681

Table 5.2: Error and convergence rate for ρ in quasi 3D comparison based on rectangular mesh.

		$h_0 = \frac{1}{8}$	$h_0/2$	$h_0/2^2$	$h_0/2^3$
FDM	error	0.0017	5.9839E-4	1.5889E-4	4.3398E-5
+OBBDG	rate	-	1.5221	1.9130	1.8723
SIPG	error	2.5821E-4	5.6058E-5	1.4493E-5	3.5810E-6
+OBBDG	rate	-	2.2036	1.9515	2.0170

Table 5.3: Error and convergence rate for ϕ in quasi 3D comparison based on rectangular mesh.

and computational time in Chapter 4. In addition, it can be predicted that the structure of mass and stiff matrix in quasi 3D model is more complicated than that in 2D model. Thus, it is expected that SIPG+OBBDG method should be the best choice in this case. However, we still want to point out that the accuracy order will be reduced when MFEM and LSFEM are applied to solve a single Poisson's equation.

Consider the following Poisson's equation

$$\begin{cases} -\frac{1}{r}\frac{\partial}{\partial r}\left(r\frac{\partial \phi}{\partial r}\right) = f(r,z), & (r,z) \in \Omega = (0,1)\times(0,1), \\ \frac{\partial \phi}{\partial r} = 0, & (r,z) \in \Gamma = \{0\}\times(0,1), \\ \phi(r,z) = g(r,z), & (r,z) \in \partial\Omega\backslash\Gamma. \end{cases}$$

The exact solution is given by

$$\phi(r,z) = \cos(\pi r^2 z).$$

The error and order of accuracy are shown in Table 5.4 - 5.6. The results indicate that BDM_1 performs worse - its accuracy is lower and cost more memory and computational time - than RT_0. This should be due to the incompatibility between the singularity and the definition of finite element space W_F^{mfem}. It can be also found that the convergence rate for $-\frac{\partial \phi}{\partial r}$ is suboptimal in LSFEM. Hence, these method will not be taken into consideration in simulation.

We still need to take a look at the error and convergence rate of SIPG+OBBDG method in this case. We use the same toy system in Test 1 but the terminal time is $T = 0.1$. The 'exact' solutions are numerically defined by using very fine mesh, namely $h = \frac{1}{128}$, and tiny time step size $\tau = 10^{-4}$. In order to compare the convergence rate in space for each coupled method, the time step is chosen as small enough. Table 5.7 shows the error and convergence rate of SIPG+OBBDG method. It is indicated that SIPG+OBBDG method converges optimally and consequently can be applied into simulations.

		$h_0 = \frac{1}{16}$	$h_0/2$	$h_0/2^2$	$h_0/2^3$
LSFEM	error	0.0015	3.8404E-4	9.6090E-5	2.4025E-5
	rate	-	1.9943	1.9988	1.9998
RT_0	error	0.0181	0.0091	0.0045	0.0023
	rate	-	1.0000	1.0000	1.0000
BDM_1	error	0.0202	0.0101	0.0050	0.0025
	rate	-	1.0009	1.0002	1.0001

Table 5.4: Error and convergence rate for ϕ in quasi 3D comparison based on triangular mesh.

		$h_0 = \frac{1}{16}$	$h_0/2$	$h_0/2^2$	$h_0/2^3$
LSFEM	error	0.0385	0.0125	0.0042	0.0014
	rate	-	1.6274	1.5861	1.5516
RT_0	error	0.0631	0.0317	0.0159	0.0079
	rate	-	0.9952	0.9986	0.9996
BDM_1	error	0.0139	0.0066	0.0033	0.0016
	rate	-	1.0660	1.0177	1.0045

Table 5.5: Error and convergence rate for $-\frac{\partial \phi}{\partial r}$ in quasi 3D comparison based on triangular mesh.

		$h_0 = \frac{1}{16}$	$h_0/2$	$h_0/2^2$	$h_0/2^3$
LSFEM	error	0.0201	0.0051	0.0013	3.2956E-4
	rate	-	1.9949	1.9728	1.9653
RT_0	error	0.0630	0.0317	0.0158	0.0079
	rate	-	0.9931	0.9981	0.9995
BDM_1	error	0.0113	0.0054	0.0027	0.0013
	rate	-	1.0586	1.0157	1.0040

Table 5.6: Error and convergence rate for $-\frac{\partial \phi}{\partial z}$ in quasi 3D comparison based on triangular mesh.

		$h_0 = \frac{1}{16}$	$h_0/2$	$h_0/2^2$	$h_0/2^3$
σ	error	0.0316	0.0083	0.0020	4.5711E-4
	rate	-	1.9210	2.0789	2.1109
ρ	error	0.0267	0.0079	0.0020	4.6124E-4
	rate	-	1.7594	1.9896	2.1070
ϕ	error	2.2324E-5	5.6113E-6	1.3945E-6	3.0716E-7
	rate	-	1.9922	2.0086	2.1827

Table 5.7: Error and convergence rate for SIPG+OBBDG method in quasi 3D test on triangular mesh.

5.4 Numerical simulation

Example 1. A double-headed streamer propagation in nitrogen.

This application is widely used in many literatures, such as [7, 101, 104]. Since nitrogen is a non-attaching gas, we directly consider Model (5.1). In the early studies, this simulation was always carried out in a 1cm gap. In this thesis, we would like to use the same background field and enlarge the gap length to 5cm. The physical coefficients are cited from [62]; hence, the parameter S in the source term will be proportional to the gap length so that we need much smaller temporal step size to complete this simulation.

The background electric field is imposed by $[0, -52]$ kV/cm as in [7, 101, 104]. The initial data is concentrated at the middle of the z-axis,

$$N_e = N_p = 10^8 + 10^{14} \exp\left\{ -\left(\frac{r}{0.025cm}\right)^2 - \left(\frac{z - 2.5cm}{0.027cm}\right)^2 \right\} cm^3.$$

The mesh size is chosen to be $\triangle r = \triangle z = \frac{1}{2000}$ so that there are totally 400,000 elements. The time step size is $\triangle t = 10^{-5}$ which corresponds to $2.5 \times 10^{-3} ns$.

Firstly, we show the consistency between our simulation and the existing simulations by Figure 5.2. Compared with the results in [7, 101, 104], it can be concluded that our result is correct up to their terminal time. Since our gap length is 5 times as others', we can try to figure out what will happen after 2ns. Figure 5.3 shows the evolution of electric field along z-axis from 2ns to 5ns. From this figure, we can observe that electric field possesses two local maxima in magnitude. Due to the mechanical research, e.g. [34], there are two streamer heads with opposite polarities around the local maximum points; and they move in the opposite directions. Figure 5.4 shows the important properties of these two streamers. From this figure, we can conclude that (1) negative streamer moves faster than positive streamer; (2) both of them will firstly slow down for a while then speed up towards their own destination; (3) the average speed for both streamers is of order $10^7 \sim 10^8$ cm/s which is closed to the experimental result [34]; (4) the maximum particle density

in positive streamer is higher than that in negative streamer, but both have order $10^{13}\ cm^{-3}$; (5) both streamers develop very fast within 1ns, then they become stable after 1.75ns; (6) streamers have a period of rapid growth in the first nanosecond, which is the effect of the first corona; then the electric field tends to be stable for about 0.5-0.75ns; once the electric field becomes stable, the streamers propagate with a nearly constant acceleration driven by the background ionization.

For the distribution of electric field and net charge in the whole domain, one can refer to Figure 5.5 (2ns) and 5.6 (4ns). It can be clearly seen from both figures that the streamer heads indeed have the same position as the local maxima of electric field. The sharp change of net charge and electric field only concentrate in a tiny area, especially there is one net charge layer with width about 0.1mm in each streamer head. This is the evidence that we need to apply discontinuous Galerkin method in the streamer propagation simulations.

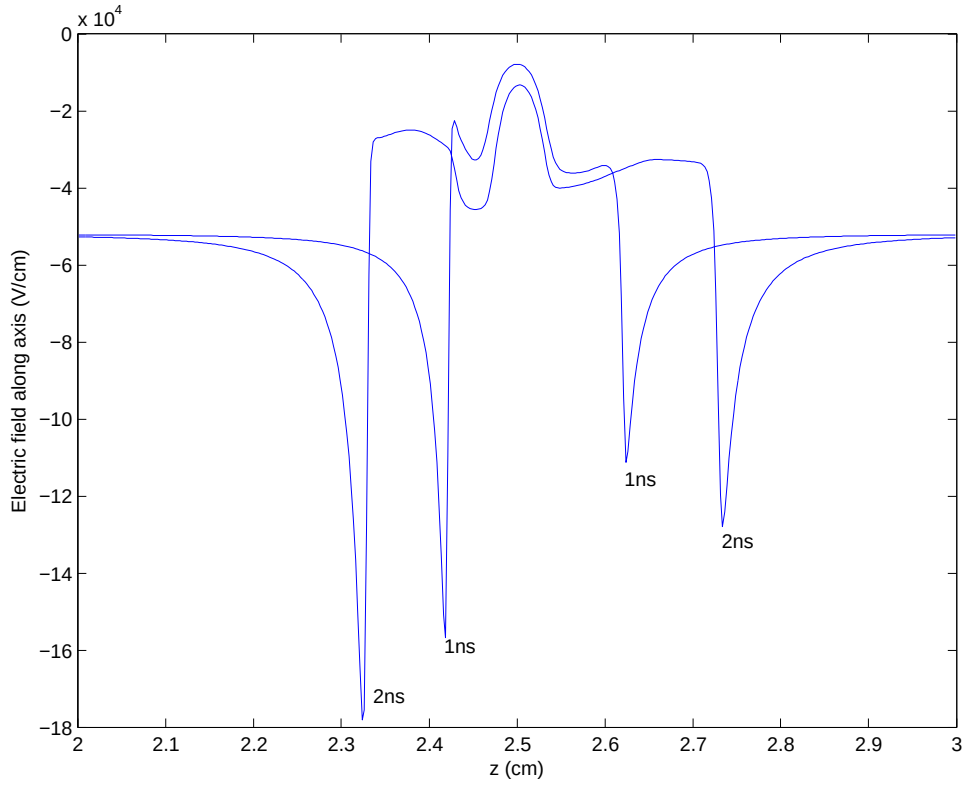

Figure 5.2: The z-component of electric field (V/cm) along z-axis at 1ns and 2ns in the simulation for nitrogen.

Example 2. Streamer propagation in SF_6.

This example is used to indicate the availability of SIPG+OBBDG method on non-uniform mesh.

SF_6 is an attaching gas, thus negative ions and attachment effect must be taken into consideration. In this case, the movements of the heavy ions are neglected [103]. Then the model becomes

$$\begin{cases} \frac{\partial N_e}{\partial t} + \frac{1}{r}\nabla \cdot (rN_e\mathbf{W}_e - r\mathbb{D}\nabla N_e) = (\alpha(|\mathcal{E}|) - \eta(|\mathcal{E}|))N_e|\mathbf{W}_e|, \\ \frac{\partial N_p}{\partial t} = \alpha(|\mathcal{E}|)N_e|\mathbf{W}_e|, \\ \frac{\partial N_n}{\partial t} = \eta(|\mathcal{E}|)N_e|\mathbf{W}_e|, \\ -\frac{1}{r}\nabla \cdot (r\nabla V) = \frac{e}{\epsilon}(N_p - N_e - N_n),\ \mathcal{E} = -\nabla V, \end{cases} \tag{5.37}$$

where the ionization coefficient $\alpha(|\mathcal{E}|)$, attachment coefficient $\eta(|\mathcal{E}|)$ and the drift

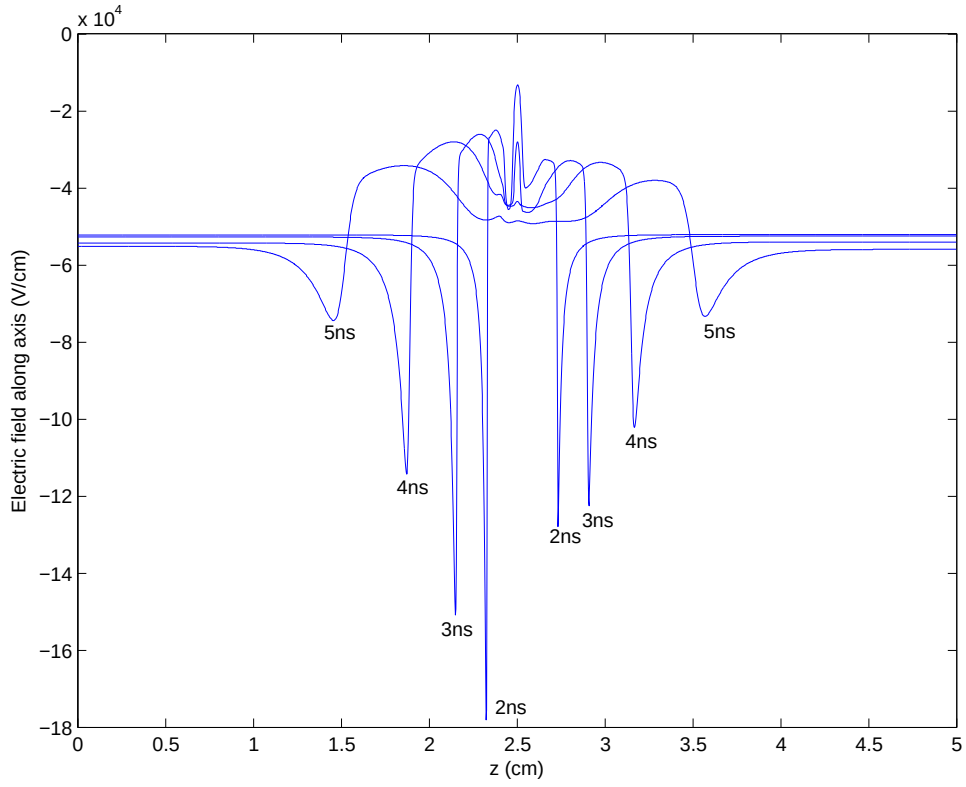

Figure 5.3: The evolution of z-component of electric field (V/cm) along z-axis from 2ns to 5ns in the simulation for nitrogen.

velocity of electron $\mathbf{W}_e$ are all taken from [63]; and the diffusion coefficient is taken $\mathbb{D} = 1900\mathbb{I}\frac{cm}{s^2}$. The physical domain is $[0, 0.4cm] \times [0, 0.5cm]$ and the applied voltage is 50 kV. The initial data is concentrated on the bottom of z-axis,

$$N_e = N_p = 10^4 + 10^{14} \exp\left\{ -\left(\frac{r}{0.021cm}\right)^2 - \left(\frac{z}{0.027cm}\right)^2 \right\} cm^3,\ N_n = 0cm^{-3}.$$

Since the particles will mainly move along the axial direction, the mesh size is uniform in z-direction, say $\triangle z = \frac{1}{400}$. In the r-direction, there are 80 cells between 0 and 0.1cm, 40 cells between 0.1cm and 0.2cm and 40 cells in the rest interval. Totally, there are 64,000 elements. The time step size is $\triangle t = 10^{-5}$ which corresponds to $10^{-3}ns$.

Figure 5.7 shows the distribution of different particles along axial direction at 1ns. It can be observed that the density of electrons is lower than that of ions by

about one to two orders. This means the attaching effect is much important than ionization in SF_6. From Figure 5.8, it is found that electric field performs differently with that in Example 1. In nitrogen, the electric field has two isolated valleys; but in SF_6, there is one valley just next to one peak.

The net charge density also has different performance. Take 1ns for example. Combine Figures 5.9 and 5.10, we can find that the negative net charge is concentrated around the sharp change of electric field and formed a thin layer whose width is only about 40 μm. The positive net charge follows closely behind the negative net charge. The area of positive net charge is much larger than that of negative net charge. Due to the attaching effect, the maximum of negative net charge density is about 8 times larger than that of positive net charge density, say 5.3246 $\mu C/cm^3$ and 0.7063 $\mu C/cm^3$ respectively. Our results are very closed to those in [103]. This proves that SIPG+OBBDG is a successful choice for non-uniform mesh.

Example 3. A point-to-plane streamer propagation in nitrogen.

We turn back to consider Model (5.1) in nitrogen. But the computational domain is not rectangular any longer. The upper boundary of the computational domain is given by a hyperbola

$$\frac{z^2}{(1cm)^2} - \frac{r^2}{(0.14cm)^2} = 1, \quad \text{for } 0 \le r \le 0.1cm.$$

Therefore, the gap length in this example is from 1cm (at $r = 0$) to 1.23cm (at $r = 0.4cm$). Let

$$f(r) = \begin{cases} \sqrt{1 + \frac{r^2}{0.14^2}}, & 0 \le r \le 0.1, \\ 1.23, & 0.1 < r \le 0.4, \end{cases}$$

and the computational domain be

$$\Omega = \{(r, z) : 0 < r < 0.4, 0 < z < f(r)\}.$$

Since the domain has complex geometry is this case, we consider triangular mesh and SIPG+OBBDG method. From the last example, we can construct non-uniform mesh to reduce the number of unknowns. In this simulation, we totally construct 81,920 triangles. $\triangle t$ is chosen to be 10^{-6} which corresponds to $10^{-4}ns$.

Similar domain configuration appears in some literatures. For example the work of O. Ducasse *et al.* [29]. In their work, FEM+FEM-FCT and FVM+FVM-FCT methods are applied. However, the gap length is only 1.21mm, which means our gap is about 8 times longer than theirs.

Another examples are Morrow's [65] and Kulikovsky's [47] studies. Morrow used a longer gap, which is 5cm. Kulikovsky's gap is as long as ours. However, in their studies, the continuity equations and Poisson's equation are solved in different domains. Namely, suppose their computational domain is $\Omega = \{(r, z) : 0 < r < R, 0 < z < f(r)\}$, then the Poisson's equation is solved in Ω meanwhile the continuity equations are solved in a rectangular subdomain $\Omega' = (0, R') \times (0, f(0))$ where R' is much less than R. Moreover, they assume the particle densities vanish in $\Omega \setminus \Omega'$, therefore, the Poisson's equation actually is numerically solved in Ω' and analytically

solved in $\Omega \setminus \Omega'$ by using [31]. To ensure that all particles cannot move out Ω', they only use the z-component of electric field, instead of electric field itself, to solve continuity equations. This treatment is not so appropriate that their results are not so reliable as O. Ducasse's.

Therefore, in our simulation, all the equations are solved in Ω just like O. Ducasse *et al.* did.

Suppose the applied voltage is $-60kV$ and the other physical coefficients are same as in Example 1 (cited from [62]). The initial data is given by

$$N_e = N_p = 10^8 + 10^{14} \exp\left\{ -\left(\frac{r}{0.02cm}\right)^2 - \left(\frac{z - 1cm}{0.05cm}\right)^2 \right\} cm^{-3}.$$

Figure 5.11 shows the evolution of electron density and electric field along the z-axis within 1ns. Due to ionization, more and more electrons are produced. The streamer propagates toward the planar electrode ($z = 0$) with the electric field which provides electron density about $10^{14} cm^{-3}$ around the streamer head. Similar to Example 1, the electric field in nitrogen has one isolated maximum and its maximum value is slowly decreasing.

Figures 5.12 and 5.13 show the evolution of net charge density and electric field in the whole domain within 1ns. The applied voltage is negative, therefore, only one negative streamer should be generated. From both figures, we can estimate that negative streamer propagates with average speed about 5.8×10^8 cm/s in 1ns. This speed is much faster than that in Example 1 since the background field is higher in this case. The maximum of net charge density in the streamer head is decreased from 3.6375 $\mu C/cm^3$ (0.25ns) to 1.1571 $\mu C/cm^3$ (1ns). Besides, the width of streamer head is about 0.1-0.2mm which is also similar to Example 1.

Compared with a similar numerical simulation in [96], our simulation result has a same tendency in the evolution of discharge region. Note that, the gap length in [96] is only 1mm.

5.5 Quasi 3D model v.s. 1.5D model

As mentioned in Chapter 1, the quasi 3D model can be reduced to 1.5D model if it is assumed that the distribution of particles is constant along radial direction with a fixed radius r_d. Then, in 1.5D model, the continuity equations are one-dimensional and Poisson's equation will be solved by disc method. We still apply OBBDG method to solve continuity equations. The electric field can be computed by

$$E = E_a + E_m,$$

where E_a is the applied background field and E_m is the modified electric field given by formula

$$\begin{aligned} E_m(z) &= \frac{1}{2}\left[\int_{-L}^{z} n(z')\left(1 - \frac{z-z'}{\sqrt{(z-z')^2 + r_d^2}}\right)dz' \right. \\ &\quad \left. + \int_{z}^{1+L} n(z')\left(-1 - \frac{z-z'}{\sqrt{(z-z')^2 + r_d^2}}\right)dz'\right], \end{aligned} \tag{5.38}$$

In (5.38), the net charge $n(z')$ for $z' \in [-L, 0] \cup [1, 1+L]$ is computed by reflection.

In this section, we are going to show how successfully the 1.5D model is able to simplify quasi 3D model. First of all, in (5.38), there are two parameters which can affect the solution, L and r_d. Thanks to some early works [7, 28, 102], it is concluded that L plays a very small role in disc method. It is enough to use one order of image charge, i.e., $L = 1$.

Now, the issue is r_d. Usually, r_d is given by an empirical value; for example $r_d = 0.02cm$ in [7] and $r_d = 0.05cm$ in [28]. However, different r_d will lead to totally different results. Hence, in rest of this section, we will show the effect of r_d in disc method.

For simplicity, we consider the simulation in nitrogen. The benchmark is given by the first example in quasi 3D simulation but we only consider a 1cm gap between two parallel planar electrodes. The background field is still set by 52 kV/cm.

We sketch out the electric field along axial direction at 2ns for different values of r_d. From Figure 5.14, we can see that different choices of r_d will indeed lead to

different results. It can also be found that the intensity of electric field around the streamer heads becomes smaller under larger r_d. The propagation speed is positively related to r_d when r_d is lower than some threshold. When r_d becomes larger, the locations of streamer heads will not change. This suggests that there should be a limiting solution when r_d tends to infinity, see Figure 5.15. This limit actually is the solution to the 1D model which has been seen in Chapter 2.

However, through this simulation, it can be concluded that there does not exist a proper r_d such that 1.5D model is able to replace quasi 3D model. In other words, it should be better for scientists to study 2D, quasi 3D and 3D models.

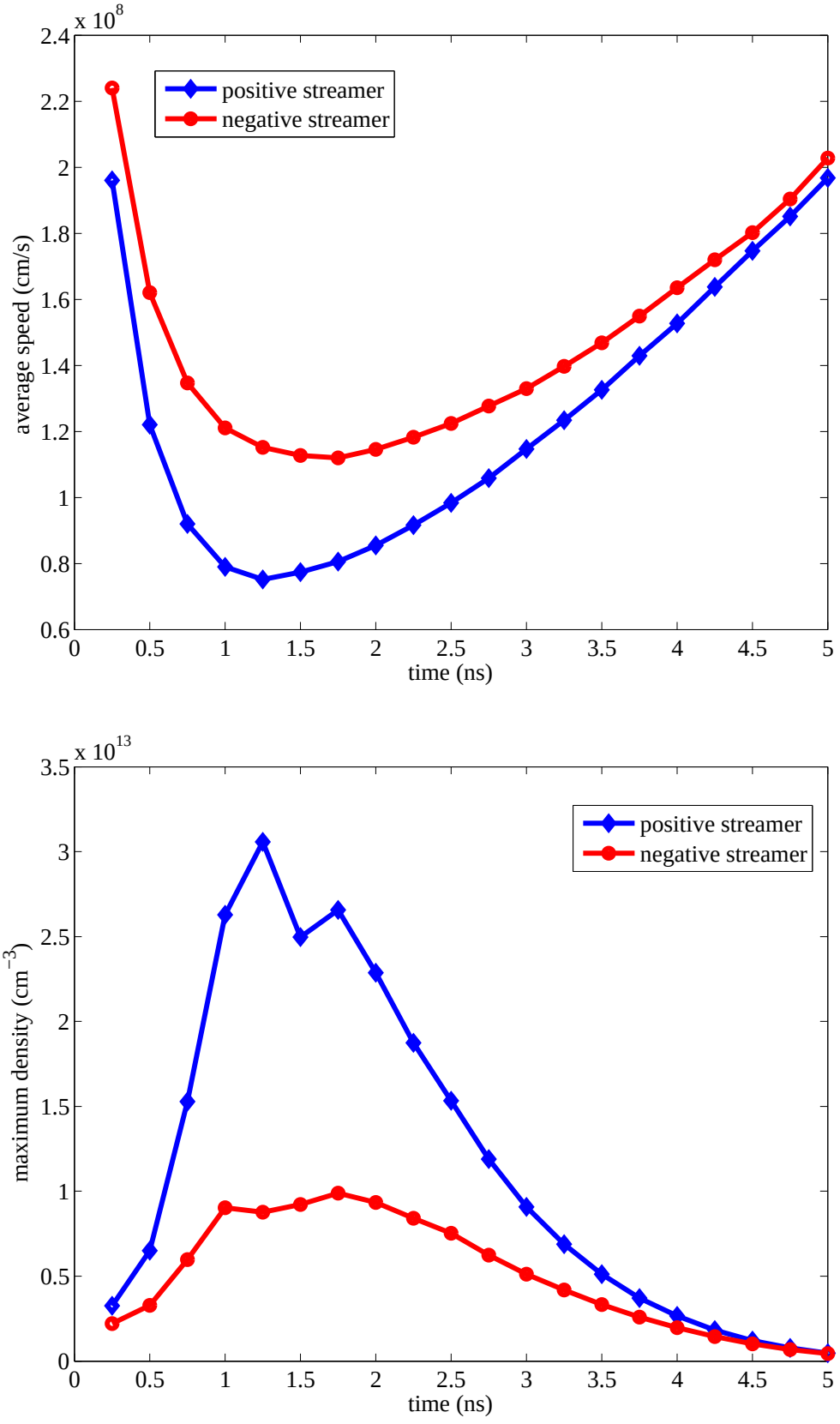

Figure 5.4: The evolution of average speed (cm/s, top) and maximum density (cm^{-3}, bottom) of positive and negative streamer along z-axis in the simulation for nitrogen.

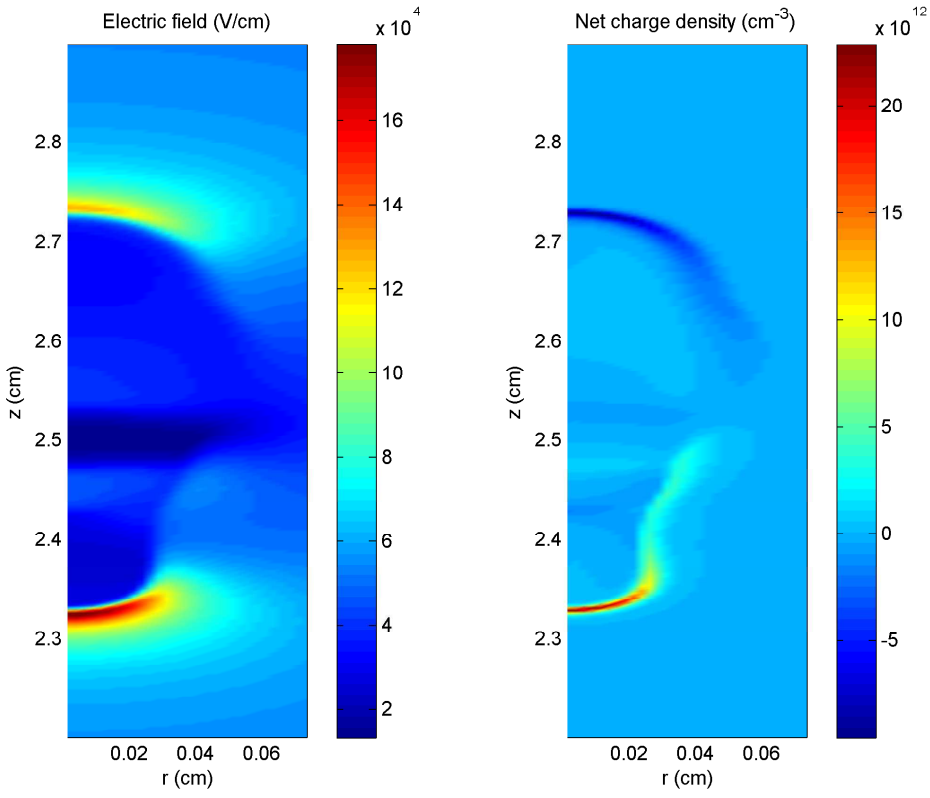

Figure 5.5: The distribution of electric field $|\mathcal{E}|$ (V/cm) and net charge density (cm^{-3}) at 2ns in the simulation within nitrogen.

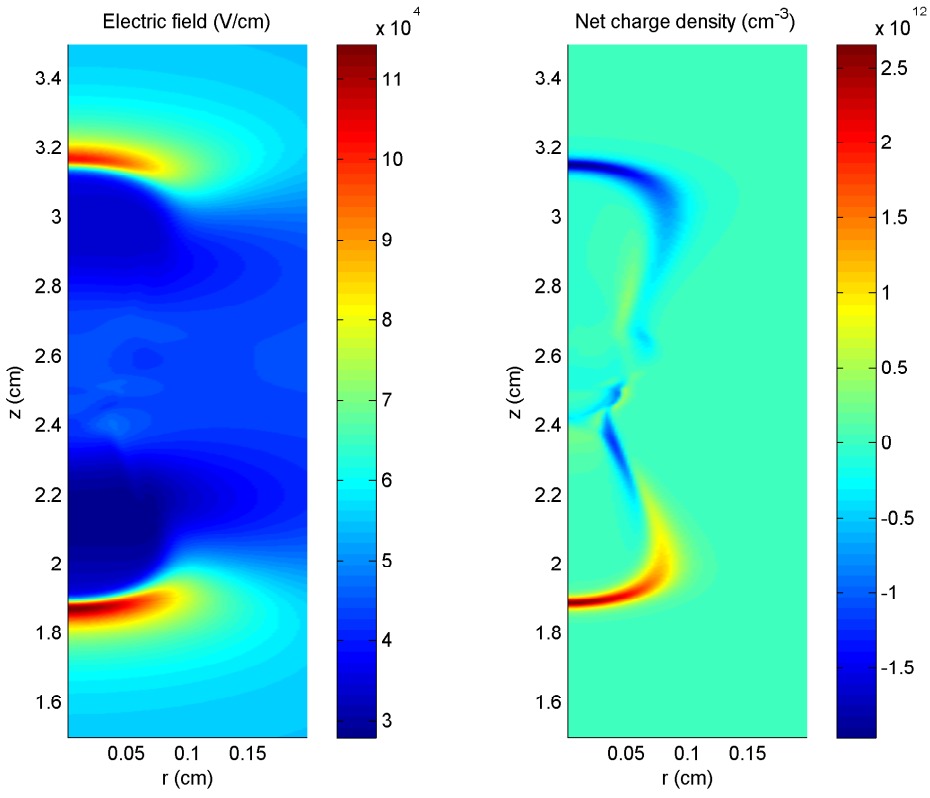

Figure 5.6: The distribution of electric field $|\mathcal{E}|$ (V/cm) and net charge density (cm^{-3}) at 4ns in the simulation within nitrogen.

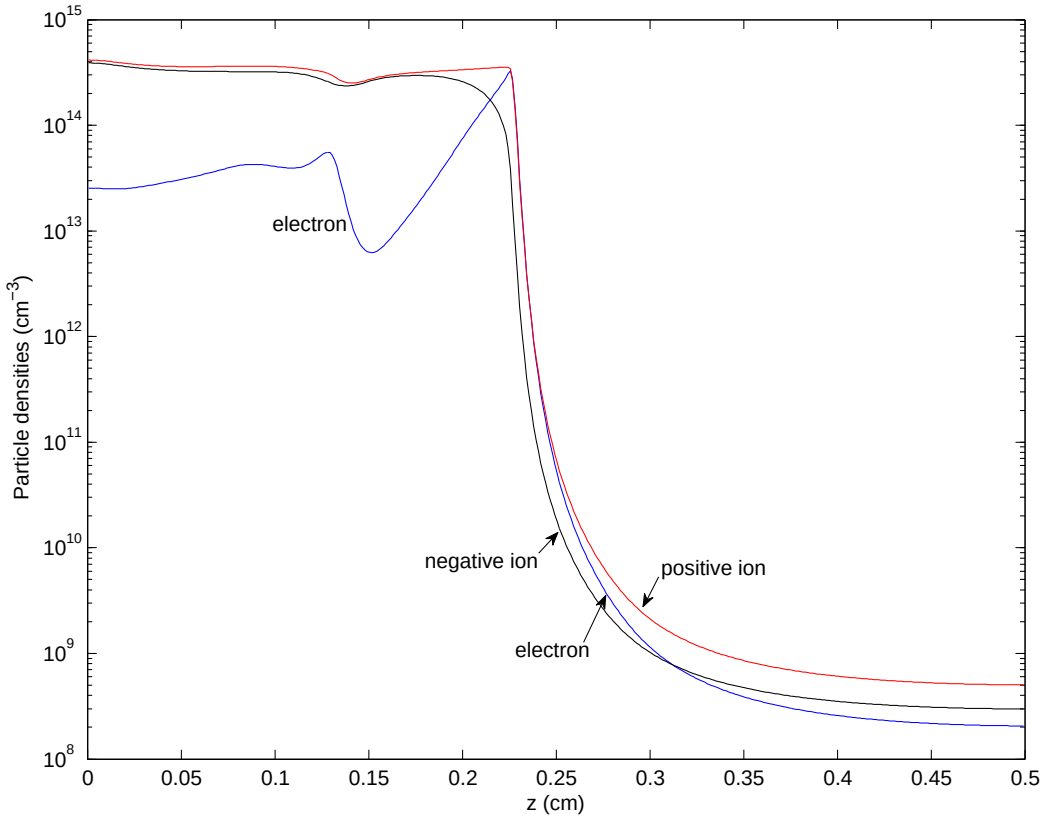

Figure 5.7: The distribution of different particles along axial direction at 1ns in the simulation in SF_6.

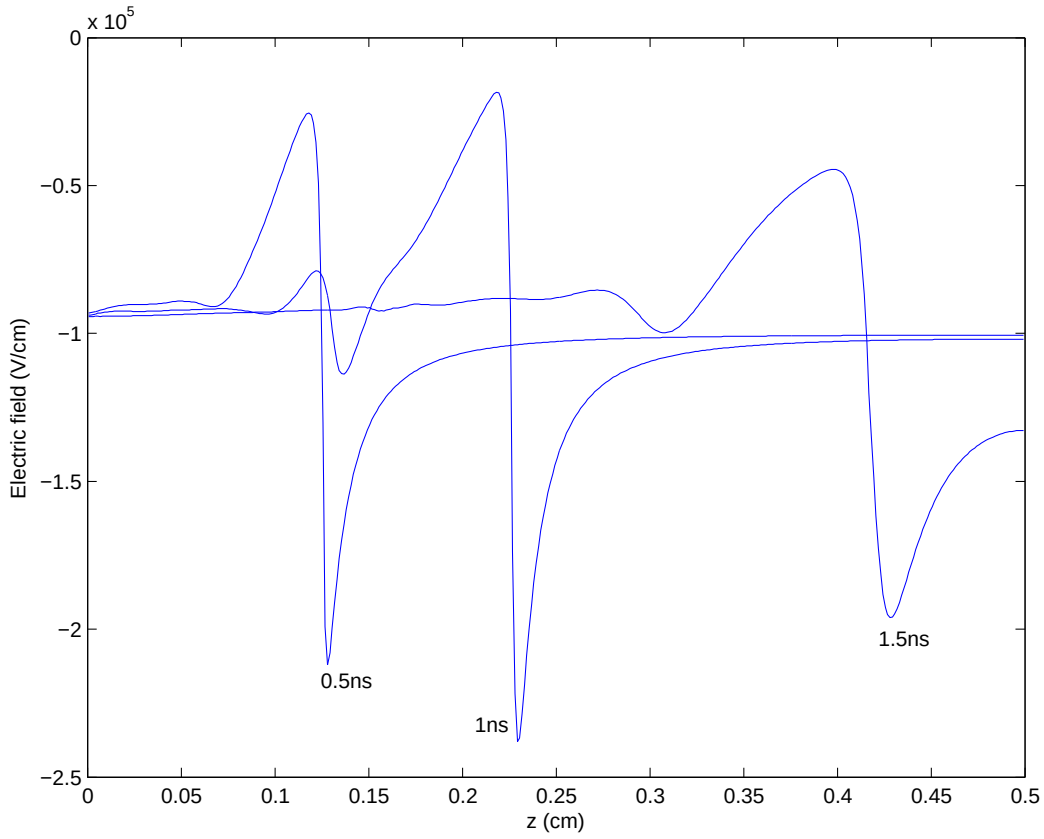

Figure 5.8: The evolution of z-component of electric field along axial direction in the simulation in SF_6.

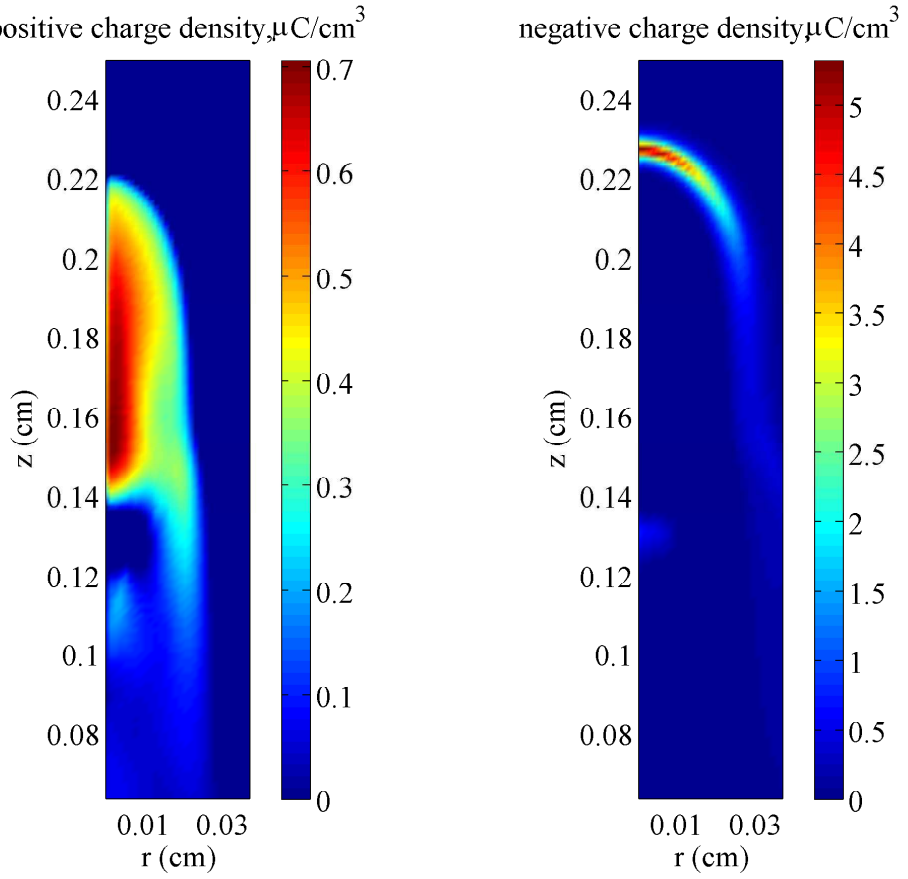

Figure 5.9: The distribution of net charge density ($\mu C/cm^3$) at 1ns in the simulation in SF_6.

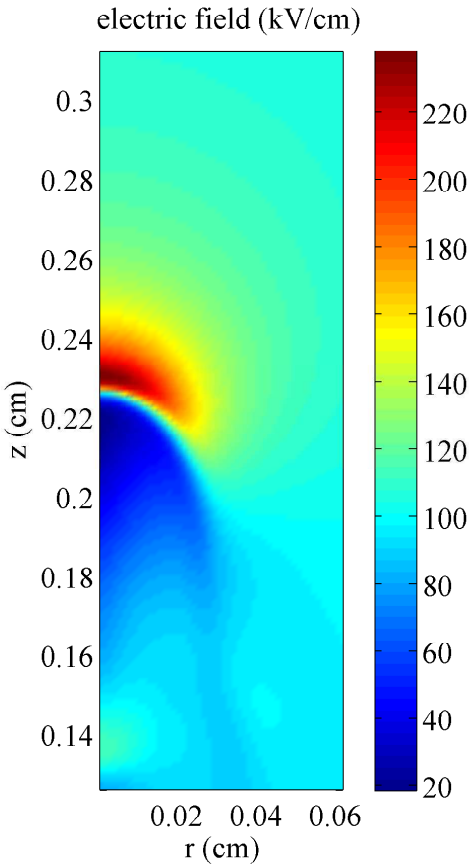

Figure 5.10: The distribution of electric field $|\mathcal{E}|$ (kV/cm) at 1ns in the simulation in SF_6.

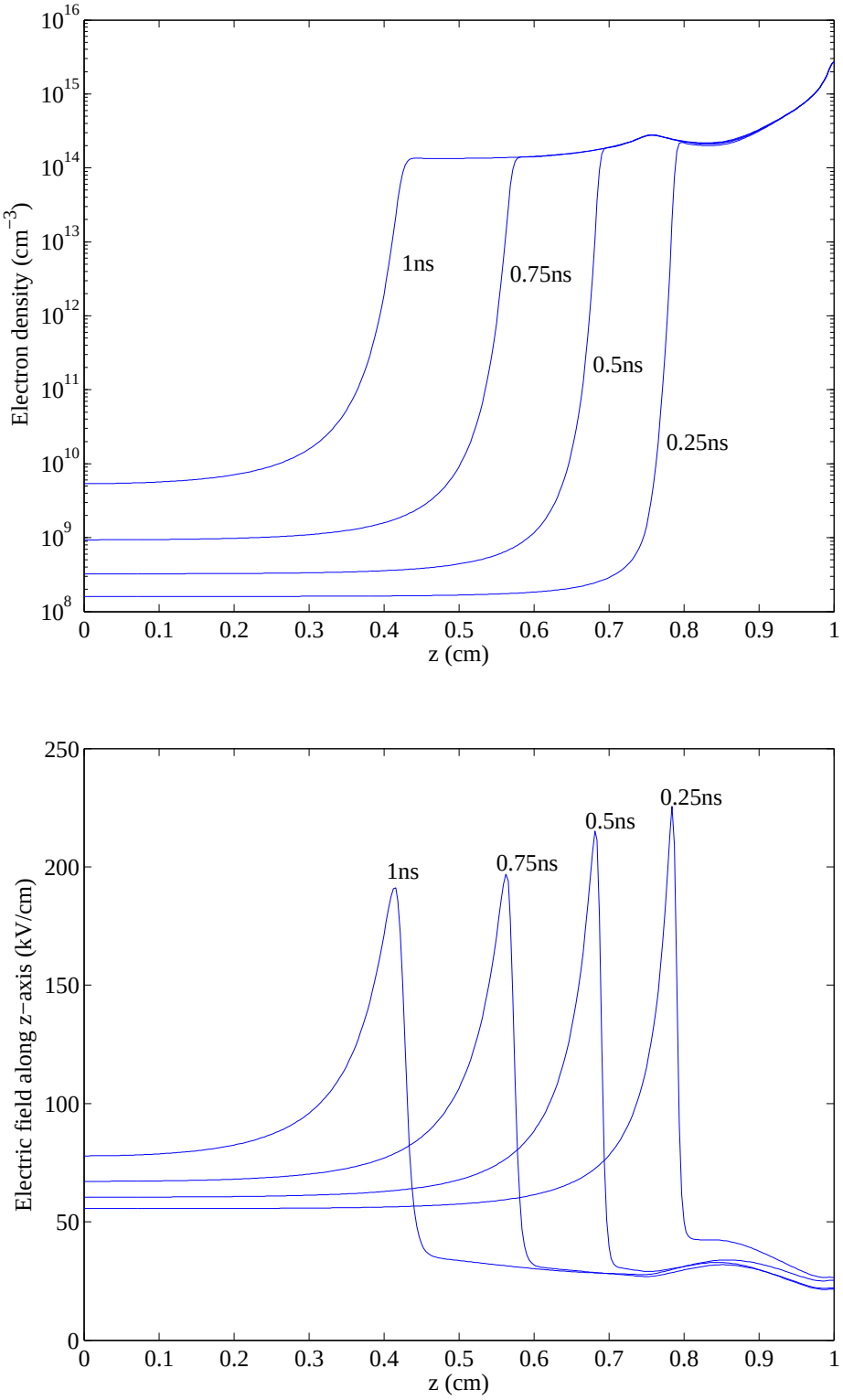

Figure 5.11: The evolution of electron density (cm^{-3}, top) and z-component of electric field (kV/cm, bottom) along the z-axis in point-to-plane streamer propagation simulation.

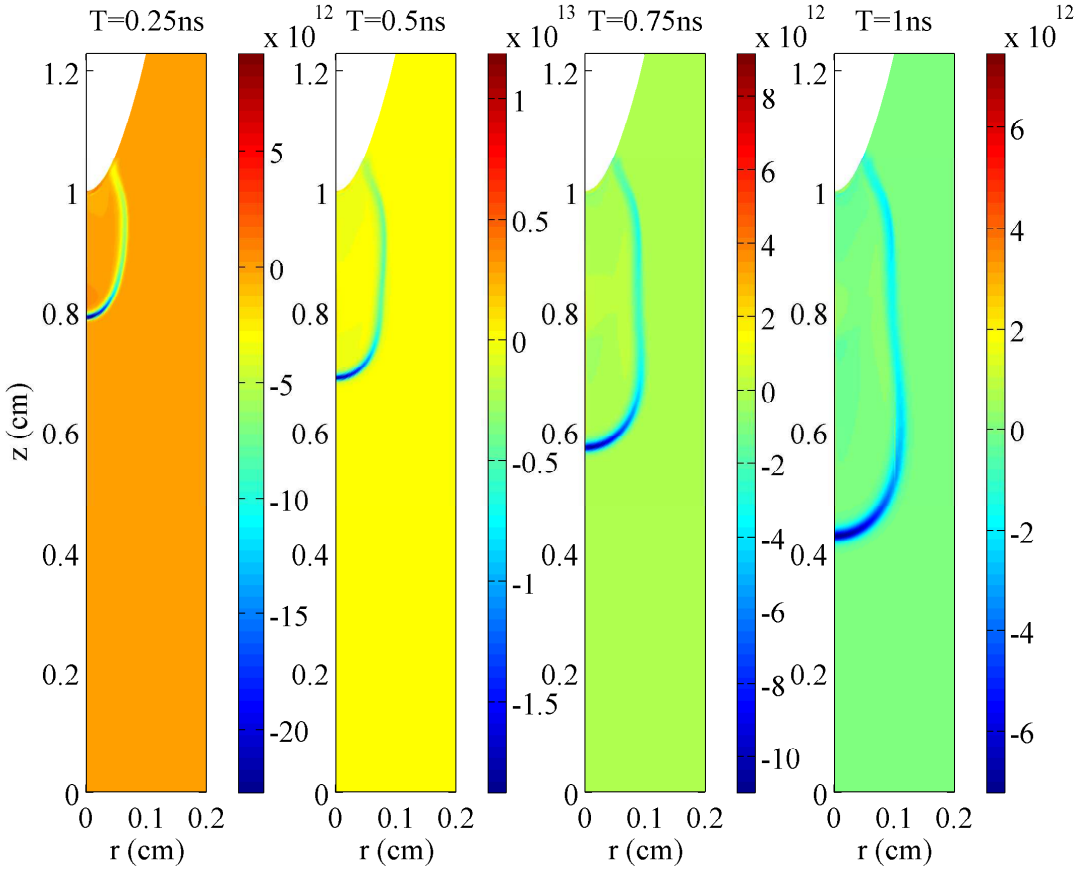

Figure 5.12: The evolution of net particle density (cm^{-3}) in point-to-plane streamer propagation simulation.

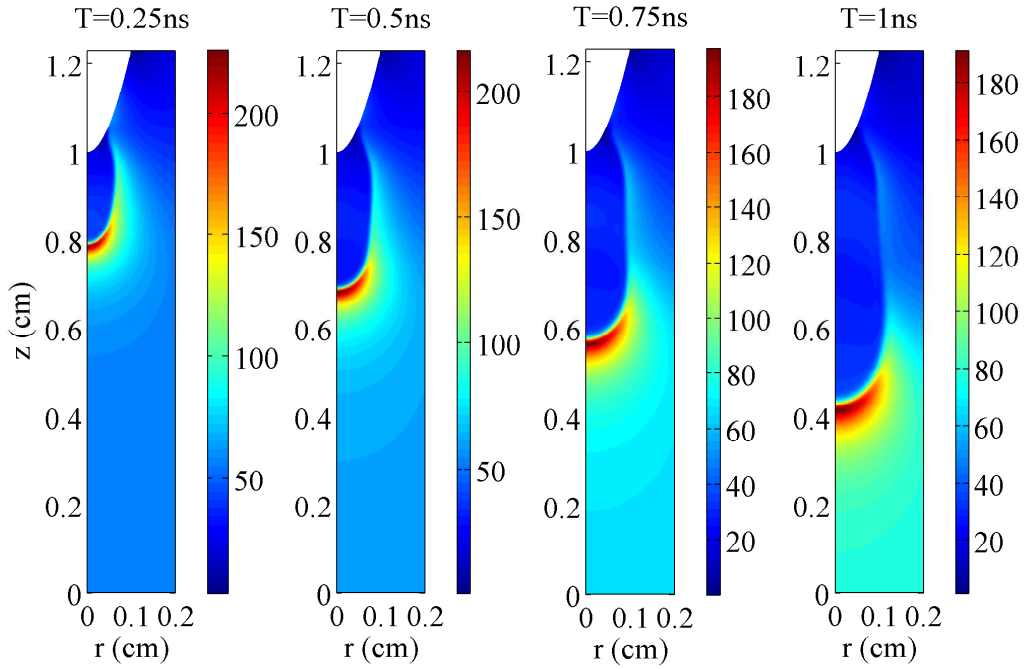

Figure 5.13: The evolution of electric field $|\mathcal{E}|$ (kV/cm) in point-to-plane streamer propagation simulation.

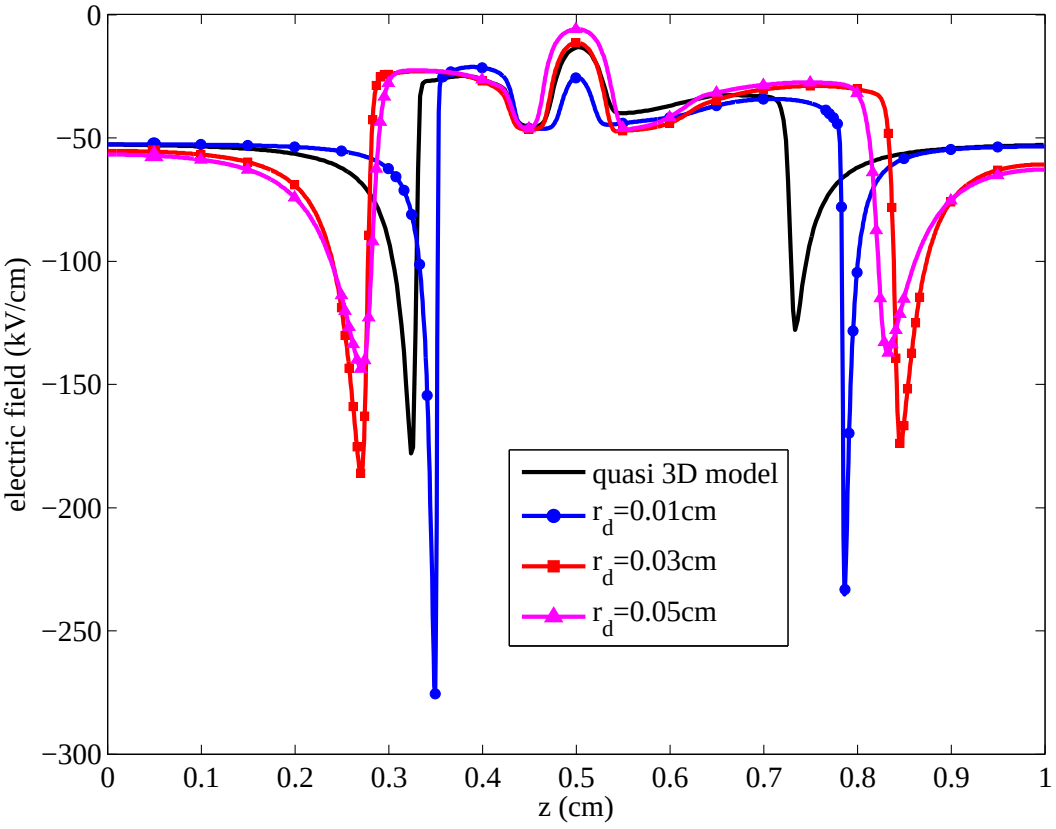

Figure 5.14: The electric field (kV/cm) along axial direction under different values of r_d. The benchmark is given by quasi 3D simulation.

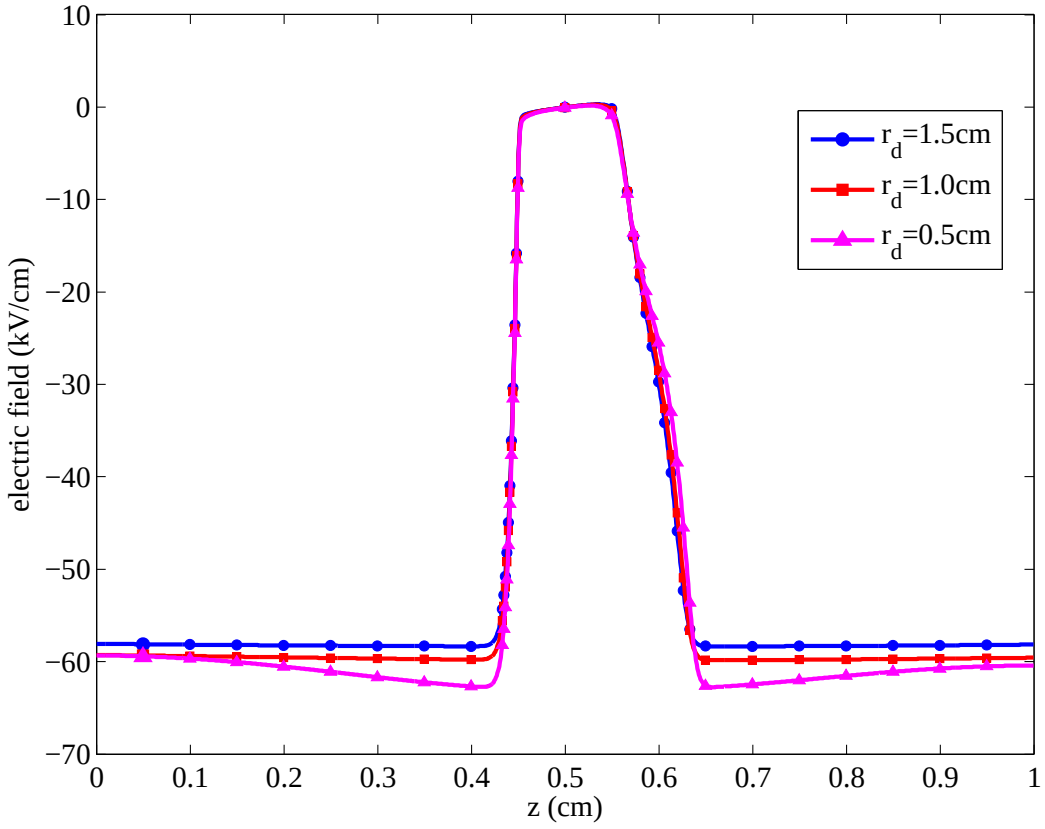

Figure 5.15: The electric field (kV/cm) along axial direction under different values of r_d. This figure is used to show the limiting solution when $r_d \to \infty$.

Chapter 6

Conclusions

In this thesis, we have studied a variety of numerical methods in simulating different streamer propagation models which include 1D, quasi 2D, 2D and quasi 3D model. Each model is a coupling between hyperbolic system and Poisson's equation. We applied DG methods (in particular, the LDG and OBBDG method) to solve the hyperbolic system. The Poisson's equation was solved by four different methods: FDM, SIPG, LSFEM and MFEM. In Chapter 2 and Chapter 4, we directly apply the traditional schemes. However, the equations in Chapter 3 and Chapter 5 contain a $\frac{1}{r}$ singularity, which is derived from polar/cylindrical coordinates under certain symmetric assumption. Therefore, we have re-derived the weak formulations by choosing new test function which is the multiplication between r and traditional test function. From mathematical point of view, this work can be regarded as an extension of traditional numerical method (especially DG method, LSFEM and MFEM) applied to partial differential equation with singularity.

Through the numerical tests in quasi 2D model (Chapter 3), it has been found that the extended numerical methods preserve the same order of accuracy as the traditional ones. However, in quasi 3D model (Chapter 5), we can only preserve the convergence rate for FDM, DG methods and RT_0 MFEM; LSFEM and BDM_1 MFEM become suboptimal for flux variable. Hence, it could be a future work to design a more suitable scheme for LSFEM and BDM_1 MFEM in this singular case.

The new schemes should be based on some properly-defined finite element subspace which satisfies the grid decomposition property (GDP) [8] for flux variable.

The numerical tests and comparisons in Chapter 2 and Chapter 3 have shown that every method possesses the same desired convergence rate if the spatial dimension is only one. But in 2D or quasi 3D tests, the results are more complicated. First of all, as suggested by Shuyu Sun and Jiangguo Liu in [88], the numerical method for solving Poisson's equation should be compatible with that for hyperbolic equation. It has been concluded that all the methods for Poisson's equation introduced in Chapters 4 and 5 are compatible with OBBDG method for hyperbolic system, since all the numerical schemes can converge in the coupling, which is the basic requirement of compatibility. If it is further required not to degenerate the convergence rate, it can be found that FDM and SIPG are compatible with OBBDG method on rectangular mesh (SIPG is compatible with OBBDG method on triangular mesh as well.); however, LSFEM and MFEM are not compatible because either they degenerates the convergence rate of OBBDG method or they are suboptimal for Poisson's equation.

Therefore, it is recommended that (1) FDM+OBBDG method is the best choice for rectangular mesh because it is easy to implement; (2) SIPG+OBBDG method is the best one for triangular mesh.

The numerical simulations of long streamer propagation have been performed in Chapter 4 and Chapter 5. The simplest simulation is carried out in the 5cm gap filled with nitrogen in Chapter 5. During the propagation, the average drift velocity of positive and negative streamer is of the order $10^7 \sim 10^8$ cm/s. The particle density is of the order $10^{12} \sim 10^{13}$ cm/s. Through our long time simulation, we have found that there are two periods during the streamer propagation. In the first period, streamers develop rapidly due to the applied voltage and first corona. In the second period, after the drastic change of electric field is over, the modified electric field gently accelerate the propagation of streamers. In the profile of the density of net charge in positive or negative streamer, there is a thin layer with width about

0.1mm, in which the particles mainly concentrated. Overall, our results are nearly the same as those of D. Bessieres *et al.* [7], which used finite volume method; but the gap length in our simulation is 5 times longer than in their work. This comparison between DG methods and finite volume method suggests that DG methods are highly potential competitors for streamer simulations and they work well in long time simulations.

We have carried out simulations not only for electropositive gas (such as nitrogen) but also for electronegative gas (e.g., SF_6 in Chapter 5). Compared with the simulation in nitrogen, some different features have been found during streamer propagation in SF_6. For example, the electric field attains its local minimum and maximum around the streamer head; positive net charge follows just behind the negative net charge; the density of negative net charge is much higher than that of positive streamer. Those are due to the attaching effect. During the discharge, part of electrons will attach on neutral particles to form negative ions. But ions are nearly immobile so that they can help modify the electric field when electrons move away.

Besides, from the simulation for SF_6 gas using the 2D model, we have observed an interesting phenomenon, which is called streamer bifurcation. It is found that the new streamer heads are formed some time after the inception of first streamer corona. The electric field around those streamer heads are different such that the positive streamer is speeded up and two symmetric negative streamer heads keep a much lower velocity. It can be a future work to modify the models to allow the random effects during streamer propagation such that more interesting phenomenon could be observed.

Actually, the most interesting part of this thesis is that SIPG+OBBDG method has been applied to a complex region. In the third example in Chapter 5, we consider a simulation of point-to-plane streamer propagation. In this simulation, a non-uniform triangular mesh is generated and the simulation result indicates again that DG methods are very competitive in this field.

Despite the many advantages of DG methods, they suffer from some disadvantages. For example, they use more unknowns to achieve higher order of accuracy, and thus, their implementation is not efficient enough. Therefore, further studies are probably needed to derive an acceleration algorithm to increase the efficiency.

Bibliography

[1] M. Abdel-Salam and N. Allen, *Inception of corona and rate of rise of voltage in diverging electric fields*, Physical Science, Measurement and Instrumentation, Management and Education-Reviews, IEE Proceedings A, 137 (1990), pp. 217–220.

[2] T. Aka-Ngnui and A. Beroual, *Modelling of multi-channel streamers propagation in liquid dielectrics using the computation electrical network*, Journal of Physics D: Applied Physics, 34 (2001), pp. 794–805.

[3] N. Aleksandrov and E. Bazelyan, *Simulation of long-streamer propagation in air at atmospheric pressure*, Journal of Physics D: Applied Physics, 29 (1996), pp. 740–752.

[4] N. Allen, G. Berger, D. Dring, and R. Hahn, *Effects of humidity on corona inception in a diverging electric field*, Physical Science, Measurement and Instrumentation, Management and Education-Reviews, IEE Proceedings A, 128 (1981), pp. 565–570.

[5] D. N. Arnold, F. Brezzi, B. Cockburn, and D. Marini, *Discontinuous Galerkin methods for elliptic problems*, in Discontinuous Galerkin Methods,

Springer, 2000, pp. 89–101.

[6] D. N. Arnold, F. Brezzi, B. Cockburn, and L. D. Marini, *Unified analysis of discontinuous Galerkin methods for elliptic problems*, SIAM journal on numerical analysis, 39 (2002), pp. 1749–1779.

[7] D. Bessières, J. Paillol, A. Bourdon, P. Ségur, and E. Marode, *A new one-dimensional moving mesh method applied to the simulation of streamer discharges*, Journal of Physics D: Applied Physics, 40 (2007), pp. 6559–6570.

[8] P. Bochev and M. Gunzburger, *On least-squares finite element methods for the Poisson equation and their connection to the Dirichlet and Kelvin principles*, SIAM Journal on Numerical Analysis, 43 (2005), pp. 340–362.

[9] ——, *Least-squares finite element methods*, in Proceedings of the International Congress of Mathematicians, Madrid, August 22–30, 2007, pp. 1137–1162.

[10] P. Bochev and M. Gunzburger, *Least-Squares Finite Element Methods*, vol. 166 of Applied Mathematical Sciences, Springer-Verlag, New York, 2009.

[11] D. L. Book, *The conception, gestation, birth, and infancy of FCT*, in Flux-Corrected Transport, Springer, 2005, pp. 5–27.

[12] J. P. Boris and D. L. Book, *Flux-corrected transport. I. SHASTA, a fluid transport algorithm that works*, Journal of Computational Physics, 11 (1973), pp. 38–69.

[13] A. Bourdon, V. Pasko, N. Y. Liu, S. Célestin, P. Ségur, and E. Marode, *Efficient models for photoionization produced by non-thermal gas discharges in air based on radiative transfer and the Helmholtz equations*, Plasma Sources Science and Technology, 16 (2007), pp. 656–678.

[14] F. Brezzi, J. Douglas Jr, and L. D. Marini, *Two families of mixed finite elements for second order elliptic problems*, Numerische Mathematik, 47 (1985), pp. 217–235.

[15] F. Brezzi and M. Fortin, *Mixed and Hybrid Finite Element Methods*, vol. 15 of Springer Ser. Comput. Math., Springer-Verlag, New York, 1991.

[16] T. Briels, J. Kos, E. Van Veldhuizen, and U. Ebert, *Circuit dependence of the diameter of pulsed positive streamers in air*, Journal of Physics D: Applied Physics, 39 (2006), pp. 5201–5210.

[17] J. S. Clements, A. Mizuno, W. C. Finney, and R. Davis, *Combined removal of SO_2, NO_x and fly ash from simulated flue gas using pulsed streamer corona*, IEEE Transactions on Industry Applications, 25 (1989), pp. 62–69.

[18] B. Cockburn and C.-W. Shu, *The local discontinuous Galerkin method for time-dependent convection-diffusion systems*, SIAM Journal on Numerical Analysis, 35 (1998), pp. 2440–2463.

[19] ——, *The Runge–Kutta discontinuous Galerkin method for conservation laws V: multidimensional systems*, Journal of Computational Physics, 141 (1998), pp. 199–224.

[20] ——, *Runge–Kutta discontinuous Galerkin methods for convection-dominated problems*, Journal of Scientific Computing, 16 (2001), pp. 173–261.

[21] A. Cohen, S. Kaber, S. Müller, and M. Postel, *Fully adaptive multiresolution finite volume schemes for conservation laws*, Mathematics of Computation, 72 (2003), pp. 183–225.

[22] A. Davies, C. Evans, and F. L. Jones, *Electrical breakdown of gases: the spatio-temporal growth of ionization in fields distorted by space charge*, Proceedings of the Royal Society of London. Series A. Mathematical and Physical Sciences, 281 (1964), pp. 164–183.

[23] A. J. Davies, J. Dutton, R. Turri, and R. T. Waters, *Predictive modeling of impulse corona in air a various pressure and humidities*, in 6th International Symposium on High-Voltage Engineering, 1989, pp. 189–192.

[24] C. Dawson, S. Sun, and M. F. Wheeler, *Compatible algorithms for coupled flow and transport*, Computer Methods in Applied Mechanics and Engineering, 193 (2004), pp. 2565–2580.

[25] S. Dhali and P. Williams, *Numerical simulation of streamer propagation in nitrogen at atmospheric pressure*, Physical Review A, 31 (1985), pp. 1219–1221.

[26] ——, *Two-dimensional studies of streamers in gases*, Journal of Applied Physics, 62 (1987), pp. 4696–4707.

[27] R. Diaz, F. Ruhling, F. Heilbronner, and P. Ortega, *The corona inception under negative impulse voltage in inhomogeneous fields*, in Eleventh International Symposium on High Voltage Engineering, 1999. (Conf. Publ. No. 467), vol. 3, IET, 1999, pp. 155–158.

[28] M. Duarte, Z. Bonaventura, M. Massot, A. Bourdon, S. Descombes, and T. Dumont, *A new numerical strategy with space-time adaptivity and error control for multi-scale streamer discharge simulations*, Journal of Computational Physics, 231 (2012), pp. 1002–1019.

[29] O. Ducasse, L. Papageorghiou, O. Eichwald, N. Spyrou, and M. Yousfi, *Critical analysis on two-dimensional point-to-plane streamer simulations using the finite element and finite volume methods*, IEEE Transactions on Plasma Science, 35 (2007), pp. 1287–1300.

[30] V. Ervin, *Computational bases for RT_k and BDM_k on triangles*, Computers & Mathematics with Applications, 64 (2012), pp. 2765–2774.

[31] C. Eyring, S. Mackeown, and R. Millikan, *Fields currents from points*, Physical Review, 31 (1928), pp. 900–909.

[32] G. J. Fix, M. D. Gunzburger, and R. Nicolaides, *On finite element methods of the least squares type*, Computers & Mathematics with Applications, 5 (1979), pp. 87–98.

[33] I. Fofana and A. Beroual, *A predictive model of the positive discharge in long air gaps under pure and oscillating impulse shapes*, Journal of Physics D: Applied Physics, 30 (1997), pp. 1653–1667.

[34] I. Gallimberti, G. Bacchiega, A. Bondiou-Clergerie, and P. Lalande, *Fundamental processes in long air gap discharges*, Comptes Rendus Physique, 3 (2002), pp. 1335–1359.

[35] G. Georghiou, R. Morrow, and A. Metaxas, *An improved finite-element flux-corrected transport algorithm*, Journal of Computational Physics, 148 (1999), pp. 605–620.

[36] ——, *A two-dimensional, finite-element, flux-corrected transport algorithm for the solution of gas discharge problems*, Journal of Physics D: Applied Physics, 33 (2000), pp. 2453–2466.

[37] ——, *Two-dimensional simulation of streamers using the FE-FCT algorithm*, Journal of physics D: Applied Physics, 33 (2000), pp. L27–L32.

[38] G. Georghiou, A. Papadakis, R. Morrow, and A. Metaxas, *Numerical modelling of atmospheric pressure gas discharges leading to plasma production*, Journal of Physics D: Applied Physics, 38 (2005), pp. R303–R328.

[39] A. Gibert and F. Bastien, *Fine structure of streamers*, Journal of Physics D: Applied Physics, 22 (1989), pp. 1078–1082.

[40] S. K. Godunov, *Different methods for shock waves*, PhD thesis, Moscow State University, Moscow, 1954.

[41] ——, *A different scheme for numerical solution of discontinuous solution of hydrodynamic equations*, Math. Sbornik, 47 (1959), pp. 271–306.

[42] N. Goelian, P. Lalande, A. Bondiou-Clergerie, G. Bacchiega, A. Gazzani, and I. Gallimberti, *A simplified model for the simulation of positive-spark development in long air gaps*, Journal of Physics D: Applied Physics, 30 (1997), pp. 2441–2452.

[43] R. Herbin, *An error estimate for a finite volume scheme for a diffusion–convection problem on a triangular mesh*, Numerical Methods for Partial Differential Equations, 11 (1995), pp. 165–173.

[44] M. Huang, R. Zeng, and C. Zhuang, *Numerical methods and comparisons for 1D and quasi 2D streamer propagation models*, Submitted to Journal of Computational Physics in Dec 2013, in revision.

[45] M. Khaled, *New method for computing the inception voltage of a positive rod-plane gap in atmospheric air*, ETZ Arch, 95 (1974), pp. 369–373.

[46] L. Krivodonova, *Limiters for high-order discontinuous Galerkin methods*, Journal of Computational Physics, 226 (2007), pp. 879–896.

[47] A. A. Kulikovsky, *Production of chemically active species in the air by a single positive streamer in a nonuniform field*, IEEE Transactions on Plasma Science, 25 (1997), pp. 439–446.

[48] E. Kunhardt and Y. Tzeng, *Monte Carlo technique for simulating the evolution of an assembly of particles increasing in number*, Journal of Computational Physics, 67 (1986), pp. 279–289.

[49] E. Kunhardt, Y. Tzeng, and J. Boeuf, *Stochastic development of an electron avalanche*, Physical Review A, 34 (1986), pp. 440–449.

[50] Y. Liu, C.-W. Shu, E. Tadmor, and M. Zhang, *Central discontinuous Galerkin methods on overlapping cells with a nonoscillatory hierarchical reconstruction*, SIAM Journal on Numerical Analysis, 45 (2007), pp. 2442–2467.

[51] L. B. Loeb, *Electrical coronas, their basic physical mechanisms*, Univ of California Press, Berkeley, 1965.

[52] R. Löhner, *An adaptive finite element scheme for transient problems in CFD*, Computer Methods in Applied Mechanics and Engineering, 61 (1987), pp. 323–338.

[53] R. Löhner and J. D. Baum, *30 years of FCT: Status and directions*, in Flux-Corrected Transport, Springer, Berlin, 2005, pp. 131–154.

[54] R. Löhner, K. Morgan, M. Vahdati, J. Boris, and D. Book, *FEM-FCT: Combining unstructured grids with high resolution*, Communications in Applied Numerical Methods, 4 (1988), pp. 717–729.

[55] J. Lowke and F. D'Alessandro, *Onset corona fields and electrical breakdown criteria*, Journal of physics D: Applied Physics, 36 (2003), pp. 2673–2682.

[56] Q. Luo, N. D'angelo, and R. Merlino, *Shock formation in a negative ion plasma*, Physics of Plasmas (1994-present), 5 (1998), pp. 2868–2870.

[57] A. Luque, U. Ebert, C. Montijn, and W. Hundsdorfer, *Photoionization in negative streamers: Fast computations and two propagation modes*, Applied Physics Letters, 90 (2007), pp. 081501–081501–3.

[58] P. MacNeice, K. M. Olson, C. Mobarry, R. de Fainchtein, and C. Packer, *PARAMESH: A parallel adaptive mesh refinement community toolkit*, Computer Physics Communications, 126 (2000), pp. 330–354.

[59] J. M. Meek and J. D. Craggs, *Electrical Breakdown of Gases*, John Wiley and Sons, Ltd., New York, NY, 1978.

[60] W.-G. Min, H.-S. Kim, S.-H. Lee, and S.-y. Hahn, *An investigation of FEM-FCT method for streamer corona simulation*, IEEE Transactions on Magnetics, 36 (2000), pp. 1280–1284.

[61] W.-G. Min, H.-S. Kim, S.-H. Lee, and S.-Y. Hahn, *A study on the streamer simulation using adaptive mesh generation and FEM-FCT*, IEEE Transactions on Magnetics, 37 (2001), pp. 3141–3144.

[62] C. Montijn, W. Hundsdorfer, and U. Ebert, *An adaptive grid refinement strategy for the simulation of negative streamers*, Journal of Computational Physics, 219 (2006), pp. 801–835.

[63] R. Morrow, *Properties of streamers and streamer channels in SF_6*, Physical Review A, 35 (1987), pp. 1778–1785.

[64] R. Morrow and J. Lowke, *Space-charge effects on drift dominated electron and plasma motion*, Journal of Physics D: Applied Physics, 14 (1981), pp. 2027–2034.

[65] ——, *Streamer propagation in air*, Journal of Physics D: Applied Physics, 30 (1997), pp. 614–627.

[66] E. Nasser and M. Abou-Seada, *Calculation of streamer thresholds using digital techniques*, in IEE Conference Publication, vol. 70, 1970, pp. 534–537.

[67] E. Nasser and M. Heiszler, *Mathematical-physical model of the streamer in nonuniform fields*, Journal of Applied Physics, 45 (2003), pp. 3396–3401.

[68] L. Niemeyer, L. Ullrich, and N. Wiegart, *The mechanism of leader breakdown in electronegative gases*, IEEE Transactions on Electrical Insulation, 24 (1989), pp. 309–324.

[69] S. Nijdam, J. Moerman, T. Briels, E. Van Veldhuizen, and U. Ebert, *Stereo-photography of streamers in air*, Applied Physics Letters, 92 (2008), pp. 101502–101502–3.

[70] J. T. Oden, I. Babuŝka, and C. E. Baumann, *A discontinuous hp finite element method for diffusion problems*, Journal of Computational Physics, 146 (1998), pp. 491–519.

[71] S. Pancheshnyi, P. Ségur, J. Capeillère, and A. Bourdon, *Numerical simulation of filamentary discharges with parallel adaptive mesh refinement*, Journal of Computational Physics, 227 (2008), pp. 6574–6590.

[72] S. Pancheshnyi, S. Starikovskaia, and A. Y. Starikovskii, *Role of photoionization processes in propagation of cathode-directed streamer*, Journal of Physics D: Applied Physics, 34 (2001), pp. 105–115.

[73] L. Papageorgiou, A. Metaxas, and G. Georghiou, *Three-dimensional numerical modelling of gas discharges at atmospheric pressure incorporating photoionization phenomena*, Journal of Physics D: Applied Physics, 44 (2011), pp. 045203–045203–10.

[74] V. P. Pasko, M. A. Stanley, J. D. Mathews, U. S. Inan, and T. G. Wood, *Electrical discharge from a thundercloud top to the lower ionosphere*, Nature, 416 (2002), pp. 152–154.

[75] F. W. Peek, *Dielectric phenomena in high voltage engineering*, McGraw-Hill Book Company, Incorporated, New York, 1920.

[76] I. Plumb, D. Cook, and S. Haydon, *Laboratory investigations of pulsed RF plasmas relevant to CW arc pluming at high-power aerials. part 1: Critical breakdown under pulsed RF conditions*, Physical Science, Measurement and Instrumentation, Management and Education-Reviews, IEE Proceedings A, 131 (1984), pp. 145–152.

[77] E. Poli, *A comparison between positive and negative impulse corona*, in 7th International Conference on Gas Discharge, 1982, pp. 132–135.

[78] B.-L. Qin and P. D. Pedrow, *Particle-in-cell simulation of bipolar DC corona*, IEEE Transactions on Dielectrics and Electrical Insulation, 1 (1994), pp. 1104–1118.

[79] H. Raether, *Electron avalanches and breakdown in gases*, Butterworths London, 1964.

[80] Y. P. Raizer, V. I. Kisin, and J. E. Allen, *Gas discharge physics*, vol. 1, Springer-Verlag Berlin, 1991.

[81] T. Renardières Group, *Research on long air gap discharges at Les Renardières*, Electra, 29 (1972), pp. 53–157.

[82] ——, *Positive discharges in long air gap discharges at Les Renardières*, Electra, 53 (1977), pp. 31–153.

[83] ——, *Negative discharges in long air gap discharges at Les Renardières*, Electra, 74 (1981), pp. 67–216.

[84] B. Rivière, *Discontinuous Galerkin methods for solving elliptic and parabolic equations: theory and implementation*, Society for Industrial and Applied Mathematics, Philadelphia, 2008.

[85] G. Schwarz, C. Lehmann, A. Reimann, E. Schöll, J. Hirschinger, W. Prettl, and V. Novák, *Current filamentation in n-GaAs thin films with different contact geometries*, Semiconductor Science and Technology, 15 (2000), pp. 593–603.

[86] C.-W. Shu, *Total-variation-diminishing time discretizations*, SIAM Journal on Scientific and Statistical Computing, 9 (1988), pp. 1073–1084.

[87] C. Soria, F. Pontiga, and A. Castellanos, *Particle-in-cell simulation of electrical gas discharges*, Journal of Computational Physics, 171 (2001), pp. 47–78.

[88] S. Sun and J. Liu, *A locally conservative finite element method based on piecewise constant enrichment of the continuous Galerkin method*, SIAM Journal on Scientific Computing, 31 (2009), pp. 2528–2548.

[89] H. Tang and T. Tang, *Adaptive mesh methods for one-and two-dimensional hyperbolic conservation laws*, SIAM Journal on Numerical Analysis, 41 (2003), pp. 487–515.

[90] E. Van Veldhuizen, P. Kemps, and W. Rutgers, *Streamer branching in a short gap: The influence of the power supply*, IEEE Transactions on Plasma Science, 30 (2002), pp. 162–163.

[91] E. v. Veldhuizen, *Electrical discharges for environmental purposes: fundamentals and applications*, Nova Science Publishers, Inc. Huntington, New York, 2000.

[92] A. Villa, L. Barbieri, M. Gondola, and R. Malgesini, *An asymptotic preserving scheme for the streamer simulation*, Journal of Computational Physics, 242 (2013), pp. 86–102.

[93] P. Vitello, D. Penetrante, and J. Bardsky, *Multi-dimensional modeling of the dynamic morphology of streamer coronas*, in IEEE Conference Record-Abstracts., 1992 IEEE International Conference on Plasma Science, IEEE, 1992, pp. 86–87.

[94] W. Wang and H. Wang, *A new model for simulating the effects of space charge in gas discharge*, in Proceedings., Second International Conference on Properties and Applications of Dielectric Materials, IEEE, 1988, pp. 182–185.

[95] M. F. Wheeler, *An elliptic collocation-finite element method with interior penalties*, SIAM Journal on Numerical Analysis, 15 (1978), pp. 152–161.

[96] G. Wormeester, S. Pancheshnyi, A. Luque, S. Nijdam, and U. Ebert, *Probing photo-ionization: simulations of positive streamers in varying N_2:O_2-mixtures*, Journal of Physics D: Applied Physics, 43 (2010), pp. 505201–505201–13.

[97] C. Wu and E. Kunhardt, *Formation and propagation of streamers in N_2 and N_2-SF_6 mixtures*, Physical Review A, 37 (1988), pp. 4396–4406.

[98] Z. Xu, Y. Liu, and C.-W. Shu, *Hierarchical reconstruction for discontinuous Galerkin methods on unstructured grids with a WENO-type linear reconstruction and partial neighboring cells*, Journal of Computational Physics, 228 (2009), pp. 2194–2212.

[99] S. T. Zalesak, *Fully multidimensional flux-corrected transport algorithms for fluids*, Journal of Computational Physics, 31 (1979), pp. 335–362.

[100] M. Zhelezniak, A. K. Mnatsakanian, and S. Sizykh, *Photoionization of nitrogen and oxygen mixtures by radiation from a gas discharge*, High Temperature Science, 20 (1982), pp. 357–362.

[101] C. Zhuang, *Study on short gap gas discharge simulations based on discontinuous Galerkin method*, PhD thesis, Tsinghua University, Beijing, 2011.

[102] C. Zhuang and R. Zeng, *A local discontinuous Galerkin method for 1.5-dimensional streamer discharge simulations*, Applied Mathematics and Computation, 219 (2013), pp. 9925–9934.

[103] ——, *A positivity-preserving scheme for the simulation of streamer discharges in non-attaching and attaching gases*, Communications in Computational Physics, 15 (2014), pp. 153–178.

[104] C. Zhuang, R. Zeng, B. Zhang, and J. He, *2-d discontinuous Galerkin method for streamer discharge simulations in nitrogen*, IEEE Transactions on Magnetics, 49 (2013), pp. 1929–1932.

NUMERICAL METHODS AND COMPARISON FOR SIMULATING LONG STREAMER PROPAGATION

HUANG MENGMIN

NATIONAL UNIVERSITY OF SINGAPORE

2014